HETEROEPITAXIAL SELF ASSEMBLING NOBLE METAL NANOPARTICLES IN MONOCRYSTALLINE SILICON

A Dissertation

by

MICHAEL SCOTT MARTIN

Submitted to the Office of Graduate Studies of
Texas A&M University
in partial fulfillment of the requirements for the degree of

DOCTOR OF PHILOSOPHY

Chair of Committee,	Lin Shao
Committee Members,	Craig Marianno
	Sean McDeavitt
	Xing Cheng
Head of Department,	Yassin Hassan

August 2013

Major Subject: Nuclear Engineering

ABSTRACT

Embedding metal nanoparticles in crystalline silicon possesses numerous possible applications to fabricate optoelectronic switches, increase efficiency of radiation detectors, decrease the thickness of monocrystalline silicon solar panels and investigate fundamental properties. Noble metal nanoparticles made of gold or silver are grown in cavities in monocrystalline silicon formed by helium ion implantation and high temperature annealing at depth greater than 500 nm from the surface. Metals are introduced into the system by low energy ion implantation or physical vapor deposited thin film on the surface, and diffused into cavities by heat treatment. Nanoparticles nucleate on the inner surface of cavities heteroepitaxially and form face centered cubic crystal structure in the case of silver. Excessive heat treatment causes metal to be emitted from nanoparticles into bulk after trapping and nanoparticle formation. Helium ion implantation, annealing and diffusion heat treatment conditions have been optimized so that residual crystalline damage, point defects and dislocations, is reduced in monocrystalline silicon substrate.

DEDICATION

To my family, especially Kimberly and Augustine

ACKNOWLEDGEMENTS

I would like to thank many people for their contribution to this research. Collaborators and friends enhanced this work in direct and indirect ways.

My graduate advisor, Professor Lin Shao, deserves much credit for this work. His vision conceived of the broad strokes, and he toiled with me to fill in the details that realized it. Lab managers Mark Hollander and Xuemei Wang greatly aided in keeping our equipment operational, which included many components crucial to this research.

Before joining Dr. Shao's group at Texas A&M in 2012, Xuemei Wang was a part of Professor Wei-Kan Chu's group at University of Houston. She had a part in collecting all of the Rutherford backscattering spectrometry data in this work, along with Dharshana Wijesundera and Prof. Chu. I am exceedingly grateful for this contribution, without which this research project would be incomplete.

In my research group, I would like to thank Michael T. Myers, Assel Aitkaliyeva, Di Chen, and Chao-Chen "George" Wei for their direct contributions as well as willingness to discuss results. Michael is an invaluable collaborator concerned with properly executing experimental research, and taught me how to fabricate electron microscopy specimens. Assel and George gave freely of their time and electron microscopy skills, and I am indebted to them. Di Chen performed several molecular dynamics simulations to help understand and elucidate the physical processes that cannot be observed experimentally. An undergraduate student worker, Alvaro Aranibar, spent countless hours preparing cross-sectional transmission electron microscopy specimens, truly yeoman's work, and paid sufficient attention to detail to progress from worker to artist in this important skill. Such dedication is not common, and I

am especially indebted to Alvaro for it.

Dr. N. David Theodore, employed by Freescale, Inc. in Chandler, AZ, is an important collaborator in this work. He fabricated eight TEM specimens using focused ion beam, and then characterized them. His patience and skill are greatly appreciated.

Ongoing discussion of results with Dan Bufford and Steven Rios, both experts in thin films studying under Prof. Xinghang Zhang, over period of years aided in crafting the data obtained into a complete story of what can be done inside open-volume defects. Access to a high-temperature gas flow furnace proved to be the lynchpin in late stages of this work provided by David Foley, a part of Prof. K. Ted Hartwig's research group. David Foley's willingness to listen and discuss with me details of point defect interactions and diffusion contributed greatly to my understanding.

Ron R. Hart, Professor Emeritus in the Nuclear Engineering department, initially hired me to work in his Ion Beam Lab and taught me how to do the nasty jobs and the glorious jobs, and taught me that an expert is one who has made all the mistakes. It is better to be an expert than not, but when making mistakes, Prof. Hart taught me to eliminate their re-occurence. I am grateful for those lessons.

A point that I do not wish to leave unsaid is to acknowledge the wonder that is creation, motive and subject of endless rational inquiry, and its Creator.

TABLE OF CONTENTS

LIST OF FIGURES

LIST OF TABLES

TABLE Page

1. MOTIVATION TO FABRICATE NANOPARTICLES IN SILICON

Embedding metal nanoparticles inside a semiconductor device has numerous applications for optoelectronics and radiation detection, including bridging the gap between metallic nanoplasmonics and semiconductor devices. Metal nanoparticles have been embedded in polymers and organic semiconductors or deposited on semiconductors and dielectrics to make plasmonic and other electronic devices. Voids in Si have been fabricated in microelectronics to getter impurities (e.g. Fe, Cu, Au), or to nucleate silicide nanoparticles (e.g. CoSi2). However, the inner surface of a void can also be used as a surface for nanoparticle growth by chemisorption of metal diffused from free surface. Such a method can substantially reduce the amount of residual crystalline damage in the Si substrate. Given two immiscible materials, this method can be generalized to fabricate precipitate nanoparticles with size and location determined by distribution of open volume defects.

Nanometer-sized metallic features have the unique ability to scatter and absorb photons with wavelengths much larger than the feature size by exciting electron density oscillations, called plasmons [34, 5]. Thus far, metal films with nanometer thickness or nanometer-sized metal islands have been fabricated on the surface of semiconductors, or textured films have been deposited on the back side of optically thin silicon wafers to excite localized surface plasmon resonances, which increases photon scattering and increases path length in small semiconductor volume [44, 3, 56, 4]. A third way has been proposed, where nanometer-sized metallic features are buried inside a thin semiconductor layer [3]. These authors proposed placing metallic nanoparticles between two films, but another method is to fabricate metallic nanoparticles by creation of open volume defects and diffusion and chemisorption of

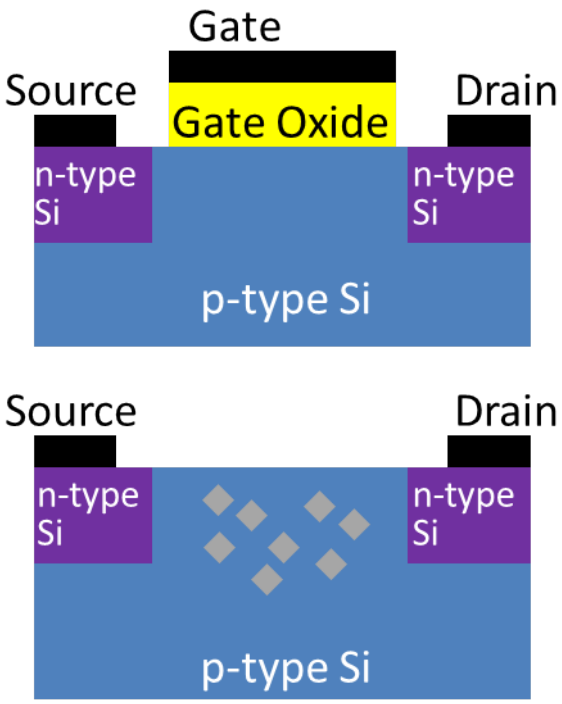

Figure 1.1: Schematic of current MOSFET design (top) and possible optically gated MOSFET design with metallic nanoparticles (bottom).

metal into defects. The advantages and disadvantages of the chemisorption method will be further discussed throughout this document.

An exciting possible application to integrating metallic nanoparticles in semiconductors is the possibility of switching from p-type charge transport, by holes, to n-type charge transport by photon irradiation. Contemporary designs of field-effect transistors, the backbone of logical computing, rely on electrical voltage signals to switch from one state to another, which causes heat creation in logic chips due to non-zero electrical resistance and is fundamentally limited by drift velocity of electrons. If a light signal switches the state of a field-effect transistor, the speed and efficiency of such devices would increase significantly. The speed of light is approximately three orders of magnitude greater than the drift velocity of an electron, and heat creation in a microprocessor chip would decrease significantly if a significant quantity of wired connections is decreased. A schematic representation of how metallic nanoparticles in semiconductor could replace the gate in a metal-oxide-semiconductor field-effect transistor is shown in Figure 1.1.

A phenomenological model for the photoelectric effect is the following: an photon is absorbed by an atom, atomic electrons are excited to momentum states from which photoemission is possible, and excited electrons diffuse to an interface and are emitted from material irradiated by photons. The quantum yield of photoemission, or number of electrons emitted per incident photon, is greatly increased when the dimensions of a silver particle are reduced to few nanometers compared to classic large surfaces studied many years ago [63, 24]. Figure 1.2, calculated using results of Chen et al, shows that quantum yield from Ag-O-Cs photoemitter increases because electron has finite chance of emission from particle each time it encounters boundary, and decreasing particle size below diffusion length of photoelectron increases boundary interaction [7]. Modeling photoelectric emission from Ag and Au nanoparticles is

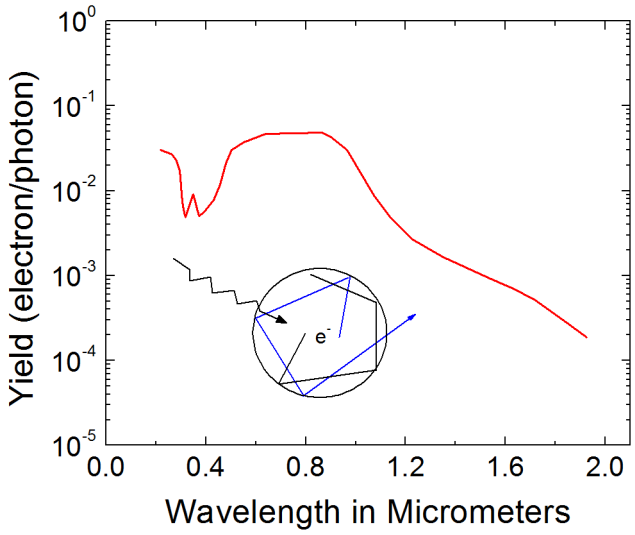

Figure 1.2: Quantum yield of nanometer sized Ag-O-Cs photoemitter.

performed by treating d-band electrons like s-band electrons in a free electron model, and this method adequately matches experimental data for photoemission from 5 nm Au particles [19]. However, this model underestimates experimental quantum yield from 5 nm Ag particles in the energy region where scattering cross sections of 5 nm Ag and Au particles differ significantly [18].

The efficiency of surface barrier detectors is determined by the interaction of ionizing radiation in the depletion zone of the detector. Placing high-Z metallic nanoparticles in the depletion zone of a silicon surface barrier detector, or even a high purity germanium detector, could significantly increase the efficiency of radiation detection. Applying equation 1.1 shows the increase in interaction that can be attained by integrating metal nanoparticles in detectors [37].

$$I = I_0 e^{(\mu/\rho)\rho x} \tag{1.1}$$

For 60 keV X-rays in Si and Au, with densities 2.33 g/cm^3 and 19.29 g/cm^3, respectively, and (μ/ρ) of 0.3207 cm^2/g and 4.528 cm^2/g, respectively, it takes 117 nm of Si to attenuate X-rays the same amount as 1 nm of Au. For 1 MeV γ-rays, the mass attenuation coefficients have similar values, but the increased density will still yield a slight enhancement. This method may not be able to uniformly improve radiation detection, but it could have an impact on specialized radiation detection issues where desired detection energy is well known, such as measuring X-rays emitted by U-235, by selecting materials that have high absorption related to electron energy level transitions at selected energies. For instance, it might be possible to make depleted uranium nanoparticles in silicon, which could have interesting radiation detection applications.

This research proposes and achieves fabrication of metal nanoparticle precipitates inside silicon, with the additional constraint of minimizing residual crystalline damage in the silicon. The results of this research project represent an important step towards full integration of nanometallic plasmonic features with semiconductors. These metal nanoparticle precipitates are grown on the inner surface of voids at depth several hundred nanometers from the surface, which are created by ion implantation and defect annealing. Metal is deposited on the surface and diffused by heat treatment to the void layer, and chemisorb out of solution on the inner surface of voids. Alternatively, metal is implanted to very shallow depth, instead of surface deposition, and subsequently diffused to defects.

This research combines the areas of growth of epitaxial films and radiation materials science. Film growth on surface of substrate is often performed to engineer superior materials and to study fundamental properties, but film growth inside a void has not been performed and studied, to the author's knowledge. Evolution of point defects in silicon into extended defects, like dislocations and voids, has been exten-

sively studied, and this area will discussed in Chapter 4. Precipitation is a massively important phenomenon in metals, especially steels, but precipitation in semiconductors is primarily studied as a method to decrease metal impurity concentrations below equilibrium concentration. This will be discussed in detail in Chapter 5. The capabilities of ion accelerators are utilized to introduce radiation damage into silicon, from which voids will evolve, so this technology is reviewed in Chapter 3. Important characterization tools are transmission electron microscopy and diffractometry, and Rutherford backscattering spectrometry using ion accelerators, and Chapter 6 reviews these two techniques. The methods applied and materials utilized to fabricate nanoparticles in silicon are numerous. Chapter 2 contains a discussion of the consequences of choosing each experimental parameter and possibilities for variation that could lead to interesting results in future.

2. PROPOSED METHODS FOR FABRICATION AND CHARACTERIZATION OF SELF-ASSEMBLING HETEROEPITAXIAL NANOPARTICLES

The process to fabricate nanoparticles, shown in Figure 2.1, involves many steps. Open-volume defects are created, then metal is introduced and diffused to defects. All of the parameters chosen to realize each step are highly dependent on the materials utilized in each step. The materials for fabrication are the substrate which will be the matrix surrounding the nanoparticle, the material which the nanoparticle will be made of, and the ion which will be implanted and will be responsible for making open volume defects. Beyond the choice of ion species, the ion energy, fluence and flux must be determined. Creation of open volume defects depends strongly on substrate and ion implantation parameters, as well as defect annealing time, temperature and atmosphere. The method of introducing the nanoparticle material must be considered, whether by film deposition on surface or ion implanation into near-surface region. Diffusion of material to open volume defect depends on heat treatment time, temperature and atmosphere. Finally, proper characterization methods must be utilized to quantify properties of produced material. All of these parameters must be chosen carefully, and a number of them must be investigated empirically to optimize nanoparticle formation and residual substrate damage.

2.1 Material selection and fabrication parameters

Nominal parameters for the fabrication of silver nanoparticles in silicon are shown in Fig. 2.1.

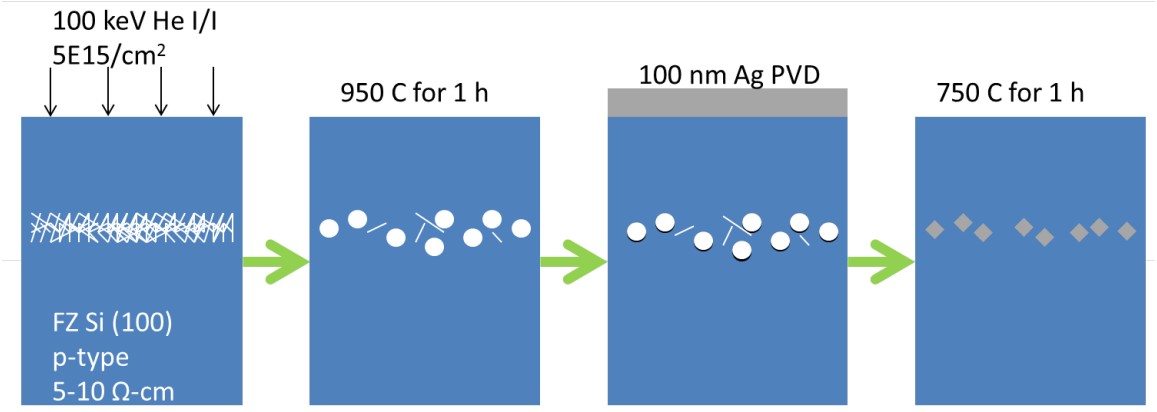

Figure 2.1: Steps in fabrication method for silver nanoparticles in silicon, including nominal parameters.

2.1.1 Substrate

Silicon is widely used, cheap and extensively studied. It is the backbone of the microelectronics industry. Monocrystalline silicon is a good substrate for experiments conducted by Rutherford backscattering spectrometry and transmission electron microscopy. Visible light can penetrate up to four microns [45].

There are two prominent processes for growth of monocrystalline silicon wafers, the Czochralski process and the float zone process [6, 55]. The float zone process creates monocrystalline silicon wafers with lower concentration of oxygen contaminants than the Czochralski process. Void dynamics are complicated by impurities, as discussed in Chapter 5. High oxygen concentration limits void growth severely, and should be avoided for the proposed process [12].

The presence of dopants will complicate the diffusion of metal, but one stated objective is to make an optoelectronic switch. In this case, the fabricated material is designed to switch from p-type to n-type by injection of electrons into the silicon substrate emitted from the nanoparticle by irradiation with light either above the

threshold energy for photoelectric effect or due to plasmonic excitation. Therefore, the substrate must be p-type, but with low dopant concentration. Monocrystalline silicon wafers grown by float zone method doped with boron to resistivity of 5-10 $\Omega - cm$, corresponding to boron concentration of 2.7×10^{15} cm^{-3} or less, will be used as the substrate for nanoparticle growth inside cavities [17].

2.1.2 Nucleating bubbles and evolving voids

Voids will be created by implanting helium ions at 100 keV to varying fluence and annealing at 950°C for varying times. Ion flux will not be investigated at this time. The range of implanted ions is 670 nm calculated by the code SRIM, which assumes the binary collision approximation and amorphous, homogenized target [76]. Helium is chosen as ion species for multiple reasons. As a light ion, it penetrates deep into silicon without causing excessive displacements, so that crystalline damage is low and large number of dislocations are avoided. Helium is chemically inactive due to its full valence electron shell, so that it does not bond with silicon atoms and is easily diffused out of the substrate. This property also causes open volume defects to be spherical. The goal is to fabricate large voids around 20 nm in diameter in the intermediate regime of void evolution discussed in Section 4.2 of Chapter 4. The density of large voids in this regime is low, but the dislocation density is also low, and dislocations are considered problematic to operation of the device.

An interesting area of additional research would be initiated by changing the shape of open-volume defects. For example, ion irradiation with sufficient fluence of hydrogen ions and defect annealing causes thin, almost two-dimensional platelets to form in silicon [49]. The shape anisotropy of nanoparticles would be significantly increased if open-volume defects are created by hydrogen irradiation and annealing, which would be desirable for plasmonic applications of noble metals in silicon or for

magnetic applications if different materials are utilized.

2.1.3 Introducing metal by ion implantation or film growth and diffusion to open volume defects

Many past studies have utilized ion implantation at a range of energies to introduce metal into silicon to investigate gettering [47]. We implant gold ions at energy 60 keV, with projected range 15 nm in silicon according to SRIM, following the method of Venezia et al [76, 69]. Gold will be introduced by this method because the eutectic temperature for gold-silicon compound formation is 360°C, and implantation decreases the concentration of gold sufficiently for heat treatment at 750°C to not form gold silicide. However, the objective is to transport and trap gold in the voids, so silicide formation may proceed from the diffusion heat treatment.

Introducing additional crystal damage into the silicon surface by implanting metal ions at low energy is not desirable, therefore films of gold and silver are deposited by physical vapor deposition with thickness up to 100 nm. The eutectic temperature for silver-silicon compound from binary phase diagram is 830°C, so diffusion heat treatments will be performed at temperatures up to 750°C for times from 10 minutes to two hours.

The diffusion kinetics of Ag and Au in Si are much different. Gold is introduced by film deposition and ion irradiation in order to determine the difference of the two methods. From a diffusion standpoint, a film more than a few nanometers thick represents an infinite source of Au atoms, whereas ion irradiation of Au represents a source diluted by large amount of surrounding Si. The final result, the semiconductor containing nanoparticles, must still behave like a p-type semiconductor instead of a metal conductor. The risk of introducing Au by surface film is that so much Au will diffuse into Si that it will no longer act like a semiconductor when a voltage is

applied. Silver diffusion in Si is limited compared to Au, and eutectic temperature is much higher, so Ag is only introduced as an infinite diffusion source, or 100 nm thick film on the surface. The risk of metallizing Si by diffusion of Ag from surface film is much lower than with Au surface film.

2.2 Determining nanoparticle concentration, depth and atomic structure

Rutherford backscattering spectrometry with 2 MeV He ion probe beam will be utilized to determine the depth and concentration of gold or silver trapped in void layer. Additionally, transmission electron microscopy, scanning transmission electron microscopy and electron dispersive X-ray spectrometry will be performed to confirm the localization of metals to voids and compare trapping of metals in voids and other defects, such as dislocations. Electron diffraction in the transmission electron microscope is utilized to understand atomic structure of nanoparticles.

The structure, if any is present, of the nanoparticle in silicon will be determined by a combination of transmission electron microscopy and channeling Rutherford backscattering spectrometry. The crystal structure of silver or gold nanoparticle superimposed on the crystal structure of silicon will cause the electron beam to have interference maxima and minima, referred to as Moire patterns [25]. Alignment of the probing ion beam, in this case 2 MeV He ions, with the major crystalline axes or planes of nanoparticle will cause a significant decrease in the backscattering yield of incident He ions, and determining the decrease in the yield and the angle between major crystalline axes will tell the crystal structure and crystallinity of nanoparticles. This method will also compare the residual damage in silicon following fabrication of nanoparticles so that the steps can be optimized to minimize crystal defects in silicon.

2.2.1 Electronic characterization

Bulk measurements of the electronic response to optical stimulation of silicon with buried nanoparticles is measured by diffuse reflectance and the resistivity will be measured by two- or four-point probe. A possibility to characterize nanoparticles is scanning tunneling microscopy based on a recently reported investigation of argon filled nanometer sized bubbles in copper [40].

3. INTRODUCTION TO ION ACCELERATORS

The experimental methods used to fabricate the semiconductor-metal nanoparticle samples are ion irradiation, thermal annealing and physical vapor deposition. This chapter focuses on ion irradiation.

There are three energy regimes of ion irradiation: low, medium and high. Ions generally possess less than 10 keV of kinetic energy in low-energy irradiation, only sufficient to deposit the material on the surface or in the few-nanometer near-surface region. High-energy ion irradiation is used to send an ion to great depth in a material, around one micrometer or greater or to cause large amount of atomic displacements by heavy ion irradiation, and is also used to analyze the depth profile of materials. One such analysis technique using 2 MeV helium ions will introduced in detail in Chapter 6. Each ion has kinetic energy from around ten to several hundred keV in medium-energy ion irradiation. This is used to implant helium at a selected depth which will be utilized to create open volume defects, or to implant gold a few tens of nanometers from the surface, which is subsequently diffused to greater depth to form nanoparticles.

Helium is implanted with 100 keV kinetic energy into monocrystalline silicon wafers, and the ion accelerator used to achieve this is shown schematically in Figure 3.1. Ions readily interact with atoms or molecules, so the whole accelerator is under vacuum to decrease the possibility of ion beam interacting with other atoms or molecules. The ion source consists of a thick tungsten filament cathode which, when heated, emits electrons which are accelerated from the cathode to the surrounding anode cylinder. Helium gas is fed through this volume, and the electrons ejected from cathode and accelerated to anode strike electrons in helium atom, imparting

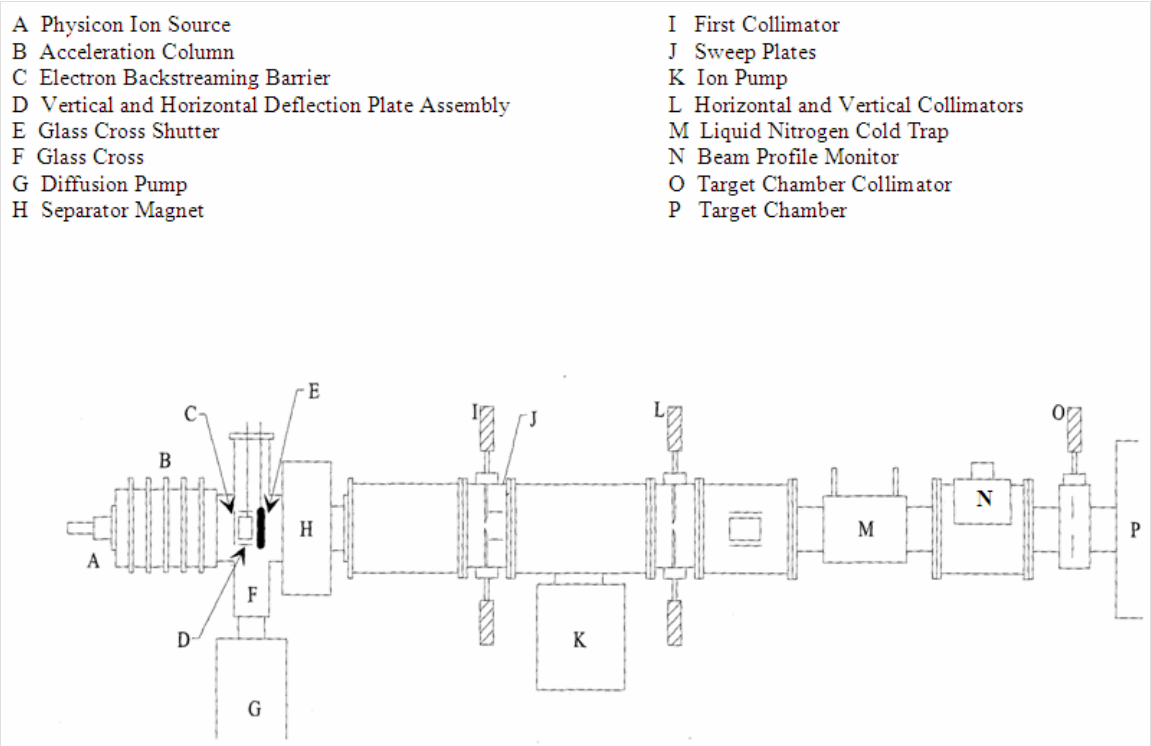

Figure 3.1: Schematic of components of 150 kV ion accelerator at Texas A&M University.

enough energy for helium atoms to become ionized. A magnet surrounding the anode/cathode helps focus the beam, and additional electrostatic focusing elements shape the beam before it enters the accelerating column. In the acceleration column, the ion beam travels across a potential set by the operator of the accelerator ranging from 50-150 kV, and the ionization state of the ion determines the amount of kinetic energy gained through the acceleration column. The research reported in this dissertation utilizes singly-positively-ionized helium, lacking one electron, accelerated through 100 kV potential to gain 100 keV kinetic energy.

The mass analyzing magnet, labeled the separator magnet in Fig. 3.1, applies a magnetic field perpendicular to the direction the ion beam is travelling, resulting in a

force that is perpendicular to both the direction of travel and the magnetic field and causes the ion beam to bend. For uniform incoming ion energy and applied magnetic field, the amount of bending varies depending on the ratio of the mass of the ion to the charge state of the ion. The source produces a broad ion beam consisting of multiple atoms and charge states, such as H_2, O and N_2 due to vacuum leaks, in addition to the desired beam, so the mass analyzing magnet is employed to bend the desired ion beam onto the target.

The beam is well-focused in the source, and the area of the beam is approximately circular and less than one millimeter in diameter. However, the object of the irradiation is to uniformly deposit ions over an area around 4 cm^2, so the beam is rastered by electromagnetic fields in two directions (not shown in Fig. 3.1). Before and after the rastering magnet, collimators shown in Fig. 3.1 further define the beam and eliminate any ions not well focused and directed to the target. Finally, the ion beam is scanned across the target area until the desired fluence, in units of $ions/cm^2$, is achieved.

Higher energy ion beams, used for analysis discussed in Chapter 6, are created by tandem accelerators, where the ion is accelerated through the terminal voltage twice. To create the helium ion beam used for analysis, a duoplasmatron source, similar to that described above with a filament made of tungsten mesh coated with a dried thorium-tungsten solution, positively ionizes helium atoms. At different stages, electrons are added and then removed from helium ions. First, helium atoms are directed through an oven filled with rubidium to add electrons followed by an acceleration column with potential of few tens of kilovolts. The beam is steered by a low energy mass-analyzing magnet into the tandem acceleration column, where the maximum potential is at the center of the column. The negative ion beam is accelerated to its incoming energy (several tens of keV) plus the maximum potential

of the column, lets say 970 kV. At the center of the column, the ions in the ion beam lose electrons by passing through N_2 gas, and are accelerated again to by the maximum potential of the column. If the ion beam gained 60 keV of energy in the low energy, then 970 keV in the first half of the tandem and 970 keV in the second half, an ion beam with kinetic energy 2 MeV is achieved by accelerating through maximum potential of 0.97 MV. The energy of the ion beam can be increased even further by searching for lower currents of ions with higher charge states before and/or after the charge exchange at center of tandem acceleration column.

4. INTRODUCTION TO ION IRRADIATION INDUCED DEFECTS

Due to the technological importance of silicon to the computing industry, it has been exhaustively studied. The ability to precisely calculate the range of ion irradiation makes it an important technology in the fabrication of semiconductor devices. Implanting a dopant into a certain volume, where depth is determined by irradiation energy, ion species and substrate and the area by lithographic masking, is a powerful tool, but the accompanying crystalline damage must be considered because it can lead to leakage currents and undesirable dopant diffusion [27]. Defects created by ion irradiation are annealed out of semiconducting devices by application of high temperature in controlled atmosphere, such as flowing high purity nitrogen or argon or ultra-high vacuum. Interstitials and vacancies are considered point defects, and if they encounter each other during defect annealing, they will annihilate; the difference in their ability to diffuse in silicon is significant however, leading to clustering into higher-dimensional defects [13]. Interstitials and vacancies can create two-dimensional dislocations or three-dimensional dislocation loops, and vacancy clusters can nucleate voids. Any significant amount of gas dissolved in the system, introduced from the surface or by ion irradiation, will promote coalescence of voids into bubbles by decreasing energy to nucleate due to the contribution of pressure on the inner surface from gas atoms.

4.1 Defects created in silicon by ion irradiation

Defects created upon ion irradiation are point defects. The displacement of one atom from its lattice position creates a pair of point defects, a self-interstitial and a vacancy. The path of the incident ion will contain many such defects, with the vacancies in the center of the path, and interstitials ejected out of the center. The

spatial separation of interstitials and vacancies is smaller for incident ions with lower mass, and increases as mass of incident ion species increases. During the short period of intense heat following traversal of the incident ion, some portion of the point defects created will recombine to annihilate. For 40 keV helium ions implanted into silicon at room temperature, it has been determined that around 90% of the point defects recombine and annihilate during irradiation [13].

Point defects that do not annihilate shortly after being created may cluster into small extended defects. In silicon, two vacancies that do not annihilate may form a divacancy, which is favorable energetically over two isolated vacancies because remaining silicon atoms neighbors will bond with each other. First principles study of vacancies in silicon suggests neighboring silicon atoms bond with each other in a divacancy configuration, but not in the midst of an individual vacancy [1]. Silicon interstitials and interstitials of the implanted ion species can rest at many different positions within the silicon unit cell, the most prominent of these are tetrahedral and octohedral positions. The tetrahedral position has the same available volume as a regular silicon lattice position [47]. Interstitials can occupy adjacent tetrahedral interstitial positions, which in some cases is energetically favorable [1]. There is also a configuration called a dumb-bell pair, where two interstitials are centered around one vacancy. Thus there are three point defects but only one "extra" atom without a lattice position [31].

4.2 Evolution of point defects into extended defects

High temperature annealing in vacuum or a flowing gas will increase the mobility of point defects, and resulting defect configurations are highly temperature dependent. Defects near a surface will be attracted to the surface and annihilate, encounter each other and annihilate, or point defects of the same type will encounter

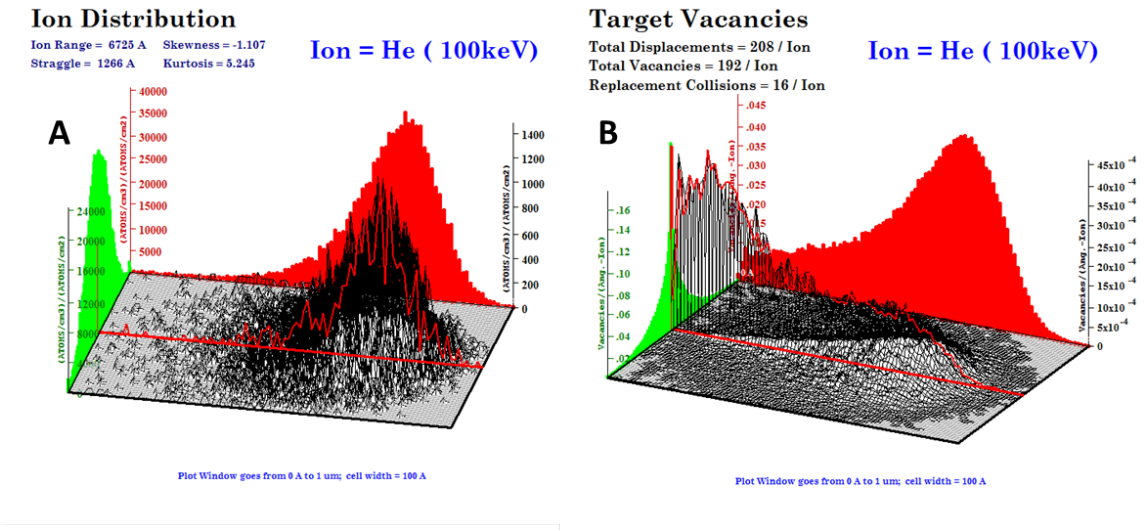

Figure 4.1: Monte-carlo simulations in Stopping and Range of Ions in Matter (SRIM) binary collision approximation computer code [76]. **A** distribution of 100 keV He ions in Si and **B** distribution of Si vacancies created by 100 keV He ion irradiation.

each other to form extended defect complexes. Extended interstitial-type defects are dislocations, dislocation loops, extrinsic stacking faults, stacking fault tetrahedra, and, in silicon, {311} rodlike defects [13]. Vacancies can cluster into divacancies, voids and intrinsic stacking faults [58]. As voids approach equilibrium, after long time annealing at high temperature, the shape will change from spherical to faceted [23]. The surface energy of major planes in silicon has been reported, and the equilibrium shape of voids is dominated by (111) and (100) plane facets [14]. For the purpose of creating voids, ion irradiation by noble gases is advantageous. Noble gases will not interact chemically with silicon atoms, and the presence of gas pressure in vacancy complexes balances a portion of energy required to make a new surface [22].

Helium ion irradiation followed by annealing is an important method to form voids in silicon because of the minimal chemical interaction of helium with silicon and the reduced defect production of light energetic ions. Experimental and theoretical

studies have determined that helium occupies the tetrahedral interstitial position [1, 2]. The theoretical study of Alatalo shows that adjacent helium atoms decorating tetrahedral interstitial sites in silicon are more energetically favorable than a single helium atom, and that individual vacancies repel helium interstitial atoms because of the high electron density due to dangling silicon bonds and the closed electron shell of helium [1]. Divacancies in silicon are electrically neutral, and photoluminescence data give evidence for trapping of helium interstitials by divacancies is shown by photoluminescence spectra [15].

The irradiation of helium into silicon creates a distribution of point defects and helium interstitials, and results of modeling by SRIM are shown in Figure 4.1. Upon annealing at 250°C, a low processing temperature, the helium profile and the accompanying profile of tetragonal strain of silicon lattice first moves toward the surface. Helium atoms in the distribution beyond the median range of helium ions are the least tightly bound. At some time after the shift of the profile towards the surface, the total concentration of helium ions and the amount of tetragonal strain induced in the silicon lattice start to decrease [9]. These authors estimate the average volume of a trapped helium atom to be 4×10^{-23} cm^3. Annealing at temperatures greater than 700°C for more than a few minutes ensures that all helium ions have been removed from the system. Such annealing leads to nucleation and growth of voids around the projected range of helium ions.

There are three regimes of bubble nucleation and void growth [22]. The first regime is insufficient ion fluence or annealing to form voids large enough to be seen in transmission electron microscopy, around 1 nm diameter. The second regime is an intermediate density of voids centered more tightly around the projected range of helium ions that can grow up to 100 nm diameter with sufficient annealing [13, 58, 22]. The third regime is sufficient fluence and annealing for a large amount of uniform

voids of diameter less than or equal to around 10 nm, up to 10% of the volume across a certain depth greater than 100 nm across, in a wide region centered around the projected range of the helium ion irradiation. One group of authors asserts that the threshold fluence to acheive the high uniform density of voids after high temperature annealing is 1×10^{16} ions cm^{-2} of 40 keV He ions, with that threshold increasing for higher energy helium ion irradiation [58]. Up to one order of magnitude below this threshold fluence, the intermediate regime of lower density of large voids is evolved.

Transmission electron micrographs of large, low density voids of the intermediate void regime also show stress fields associated with dislocations [22, 46]. Calculations performed on cavity-cavity and cavity-dislocation interactions, where cavity is less specific term indicating empty void or filled bubble, reveal that cavities are attracted to other cavities and dislocations are attracted to cavities [46]. The attractive force between two cavities fall off as inverse of the seventh power of the distance between the two, but the attractive force between cavity and dislocation falls off as the inverse of the second or third power of the distance between the two, depending on the type of dislocation. Dislocations are attracted to cavity layer buried under the surface, and dislocations are also attracted to the surface because it is a perfect defect sink. Myers et al implanted a silicon wafer with 1×10^{17} ions cm^{-2} 30 keV He ions and annealed at 700°C for 30 minutes to create a void layer with mean diameter 8 nm and volume fraction 8% at depth 300 nm, a third regime void distribution [46]. The authors used these parameters to calculate the forces applied to dislocations by void region and surface, and found that dislocations between the surface and 300 nm depth are strongly attracted to the surface. Dislocations in the bulk deeper than the voided layer are strongly attracted to the voided layer, and experience equilibrium near the center of the voided layer [46]. Transmission electron micrographs confirm these conclusions. Additional investigation by transmission electron microscopy shows that

dislocations and voids make an intersecting network, even though the dislocation paths are sometimes torturous [46].

4.3 Diffusion of impurities in silicon and their interaction with defects

Impurities can be introduced in silicon in many different ways, including the Czochrawlski wafer fabrication process discussed in Chapter 2. An important phenomenon for this study is the evolution of voids in silicon, and the presence of impurities such as carbon or oxygen alter the evolution of voids in silicon [12, 16]. Equivalent concentrations of oxygen and carbon do not equivalently limit growth because of the different phases of the two at processing temperatures. Number of trapped oxygen atoms in each void is limited by overpressurisation, but trapping of carbon atoms is not limited because processing temperatures are less than melting temperatures of carbon phases. The presence of both carbon and oxygen limits void growth, but oxygen is more uniformly distributed than carbon because it is in gaseous phase.

Implantation of silicon ions in order to introduce point defects without adding chemical effects of impurities has a weak limiting effect on void growth by introducting additional interstitials which annihilate with vacancies [12]. As discussed in Section 4.2 of Chapter 4, point defects repel helium interstitial atoms, so increasing concentration of point defects will limit migration of helium atoms and increase likelihood of point defect recombination, suppressing void nucleation and evolution.

The metals titanium, vanadium, chromium, manganese, iron, cobalt, nickel, copper and palladium are soluble at interstitial sites in silicon, and the metals zinc, platinum and gold at substitutional sites [47]. Diffusion of these metals is generally very rapid. The presence of metal contamination in silicon devices due to one or more of the dozens of processing steps during fabrication degrades the performance

of these devices, and has led researchers to develop methods to trap metals in defects introduced by ion irradiation away from the sensitive portion of these devices [32]. This field has developed to investigate, both experimentally and by modeling, the interactions of diffusing impurity atoms with dislocations and cavities, and has contributed to a deeper understanding of transient-enhanced diffusion of boron, an important p-type dopant [29, 65, 75].

4.4 Interaction of metals with cavities in silicon and structure of precipitated metal nanoparticles

The trapping of copper, gold, iron, cobalt, platinum and silver by cavities in silicon has been studied [10, 11, 52, 57, 38]. Gold and copper are trapped in voids and in other defects not containing voids, and this trapping is metastable [72]. Cavities or voids with larger curvature (smaller diameter) are more efficient metal trapping sites [62]. The presence of interstitial- or vacancy-type defects increases the thermal budget necessary to equilibrate metal concentration throughout a silicon wafer [48]. The presence of oxygen, introduced by the Czochrawlski growth process or other ways, makes Au trapping in H-induced voids less stable [70].

The number of valence electrons of the metal atom dictates the relative strength of bonds in different configurations. Multivalent cobalt and iron are more strongly bound in silicide compound precipitates, with multiple silicon atom neighbors, than on the inner surface of a cavity. Monovalent copper and gold are more strongly bound on the inner surface of a cavity, which can be referred to as "chemisorption", than as a silicide compound [54]. There is further evidence of ordered and disordered chemisorption of gold on the inner surface of cavities in silicon, where the ordered chemisorption is characterized by higher binding energy and long-range structural order of gold [48]. This ordered chemisorption represents the growth of bulk phase

gold precipitates in silicon with a well-defined boundary limited to the size of the initiating void [74].

Additional studies of Cu, Ag and Pt adsorption on inner surfaces support this conclusion. Increasing the amount of irradiation fluence of 70 keV Pt and Ag above 1×10^{14} cm^{-2} caused monotonically increasing Ag trapping, whereas trapping of Pt, which readily forms silicide, in void region saturated due to sufficient to initiate silicidation [36]. Increasing the Cu ion irradiation fluence up to 3×10^{15} cm^{-2}, exceeding the amount of Cu required for monolayer coverage of voids induced by H ion irradiation, causes large nanoparticle precipitates to form [71]. Wong-Leung et al even speculate that bulk phase Cu is grown inside voids based on fleeting glimpses of Moire fringes when investigating specimens by TEM, but no direct experimental evidence supporting this is presented [71]. A study by another group shows that there is a threshold He ion irradiation fluence of 6×10^{15} cm^{-2} for Cu to be trapped by voids grown at depth 1.2 μm [52].

Bulk, crystalline gold grown inside silicon presents a unique opportunity to study the crystal structure by channeling Rutherford backscattering spectrometry. The location of silicon and gold crystalline axes can be determined independently by finding the position or positions of minimum backscattering yields. Channeling studies of gold nanoparticle precipitates show that there is some channeling, with the backscattering yield decreasing by almost a factor of two along the $\langle 110 \rangle$ crystalline axis [73]. However, the results are not sufficiently conclusive to indicate the atomic position of gold atoms in the precipitates. The alignment of monolayer of platinum atoms adsorbed on inner surface of H-induced voids with silicon atomic planes are observed, and measurable decrease in minimum yields of $\langle 100 \rangle$, $\langle 110 \rangle$ and $\langle 111 \rangle$, with $\langle 110 \rangle$ minimum yield $_{min} = 0.56 \pm 0.03$ [35].

5. HETEROEPITAXIAL GROWTH OF METALS ON SILICON SURFACES

Careful growth of silver film on silicon will yield alignment of the two crystals [41]. Park et al. showed that small silver islands on silicon surface are aligned almost perfectly by Rutherford backscattering spectrometry, X-ray diffraction and electron microscopy[53]. Critical size of silver clusters for orientation to silicon substrate is 12 nm, and atomic planes of silver are rotated with respect to silicon atomic planes if silver cluster diameter is less than critical size [42].

5.1 Heteroepitaxy: The coincident site lattice model

Heteroepitaxial growth of supercells of any two lattice-mismatched materials has been postulated mathematically [77]. The number of unit cells required to make a nearly-periodic supercell of the interface can be calculated for any two materials with specified crystal type. For instance, for two materials with same crystal structure and lattice parameter difference of 10%, a supercell utilizing 10:9 heteroepitaxial relationship would have mismatch of 1%. The lattice parameters of silicon and silver are 5.431 Åand 4.085 Å, respectively, and the lattice mismatch of the two is 24.5%. For (100) orientation of silver and silicon, the periodic heteroepitaxial supercell relationship is two silver atomic planes for three silicon atomic planes, and for (110) and (111) orientations, the supercell is four silver atomic planes for three silicon atomic planes. Every fourth silver atomic plane and third silicon atomic plane are periodic within 0.2%. The dependence on orientation is caused by the different lattice structures, face-centered cubic (fcc) for silver and diamond-like for silicon. In (110) and (111) orientations, fcc and diamondlike lattice structures each have four atomic plane spacings per unit cell, whereas for (100) orientation, fcc has two atomic plane spacings and diamondlike lattice has four atomic plane spacings per unit cell.

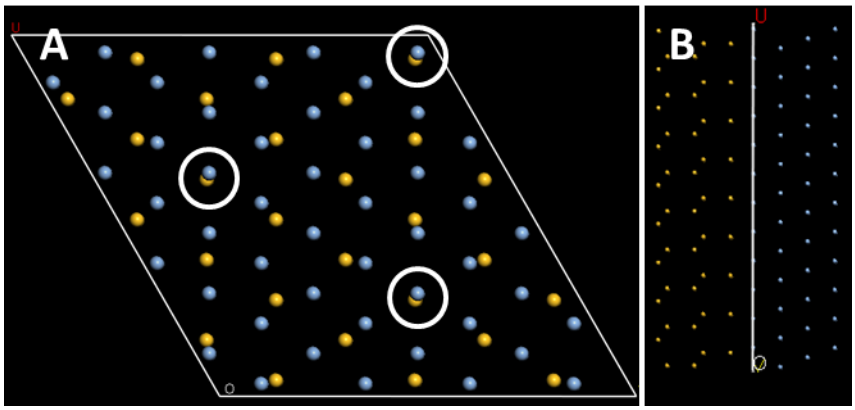

Figure 5.1: **A** Plane-view and **B** cross-section of (blue) Ag(111) on (yellow) Si(111), with co-incident sites circled in white. Materials Studio Materials Visualizer from Accelrys, Inc. is used to make this figure.

The crystalline structure of gold is the same as silver, and the lattice parameter is 4.078 Å, so the crystallographic match of silver and gold to silicon could be similar. Gold has been grown heteroepitaxially on silicon (100) and (111) faces and silicon nanowires by galvanic displacement, a type of wet chemical electroless deposition, using gold salts [61].

The co-incident site lattice model for heteroepitaxial growth of silver on silicon was proposed by LeGoues et al [41]. Figures 5.1, 5.2 and 5.3 show plan-view and cross-sectional views of Ag on Si with different orientations. The heteroepitaxial relationship for Ag(111) on Si(111) is obvious in Fig. 5.1, but less so for Ag(100) on Si(100) in Fig. 5.2. There are no obvious co-incident lattice sites for Ag(110) on Si(110), but there are a number of near-misses. The (100) and (111) projections of the fcc and diamond-like lattices are similar, whereas there is significant difference for (110) projection of those two crystal structures.

Heteroepitaxial film growth is not homoepitaxial, dislocation-free growth, where atomic planes align perfectly across an interface. Silver clusters grown on the (111)

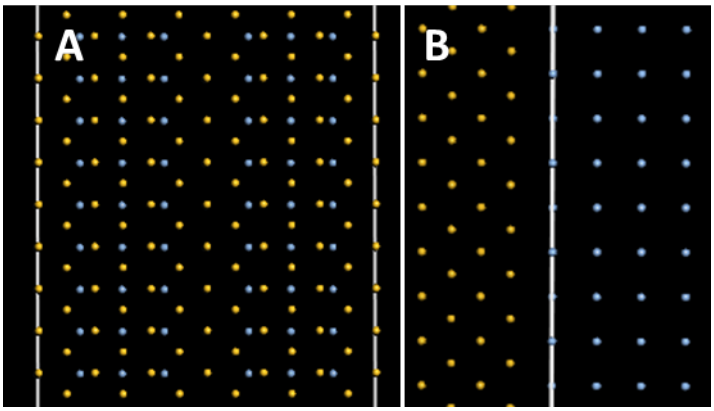

Figure 5.2: **A** Plane-view and **B** cross-section of (blue) Ag(100) on (yellow) Si(100). No co-incident sites are circled. Materials Studio Materials Visualizer from Accelrys, Inc. is used to make this figure.

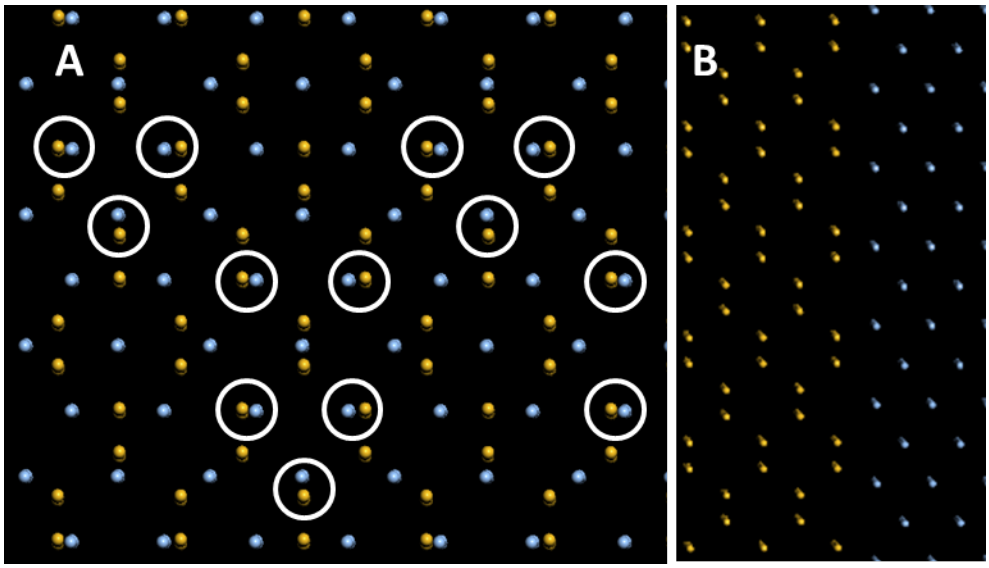

Figure 5.3: **A** Plane-view and **B** cross-section of (blue) Ag(110) on (yellow) Si(110), with possible co-incident sites circled in white. However, these sites are not very convincing. Materials Studio Materials Visualizer from Accelrys, Inc. is used to make this figure.

surface of and aligned with monocrystalline silicon bulk have strain 0.3% [42]. Heteroepitaxy must be accompanied by some strain, but the decrease from 25% strain, required by homoepitaxial growth of silver on silicon, to 0.3% is advantageous.

6. INTRODUCTION TO RUTHERFORD BACKSCATTERING SPECTROMETRY AND ELECTRON MICROSCOPY AND DIFFRACTOMETRY

The experimental methods used to characterize the structure, size and density of nanoparticles are transmission electron microscopy and diffractometry and Rutherford backscattering spectrometry. Transmission electron microscopy is based on measuring the electron beam that is transmitted through a piece of material that is less than a few hundred nanometers thick. This method can resolve changes in density, atomic number, and stress on the order of angstroms. Electron diffractometry measures diffraction of beam off of atomic planes, revealing the atomic structure. Rutherford backscattering spectrometry is based on elastic collisions of an incident ion with low atomic mass, e.g helium, and high energy with heavier atoms at rest in the material of interest. This experimental method can be used to determine the depth distribution of atoms with differing atomic masses, especially the distribution of higher atomic mass elements in a material consisting of lower atomic mass elements.

6.1 Rutherford backscattering spectrometry

This technique is named for Ernest Rutherford, whose graduate students, Geiger and Marsden, tested Rutherford's hypothesis on the nuclear structure of matter by measuring how a beam of α particles (helium nuclei) is scattered by thin foil of gold [8]. The angular dependence of the scattering, which includes backscattering, indicated that atoms consist of heavy nuclei surrounded by light electrons. Rutherford backscattering spectrometry (RBS) remains a prominent tool today, amongst the various methods of ion beam analysis, to characterize solid materials. It is valuable

for determining the depth dependence of elemental concentrations near a surface. If the material is monocrystalline, atomic displacement data can also be extracted by carefully aligning the ion beam with crystal axes or planes.

The utility of RBS is based on combination of elastic and inelastic energy loss of analyzing ion beam as it penetrates the material of interest. Elastic energy loss occurs when the incoming ion has a nuclear scattering event with an atom in the material being analyzed. The incoming ion also loses energy in the material by Coulombic interaction due to the non-zero charge state of the incoming ion. Electrons in the material being analyzed interact with the high energy ion and cause some of the kinetic energy of the ion to be lost for every atomic layer of material the ion traverses.

Data obtained by is the number of incoming ions that are scattered through a specified angle ($90°$) with certain energy. Knowledge of the angle, energy and mass of the incoming ion combined with angle, mass and energy of the backscattered ion are used to determine the mass of the atom in the material being analyzed which participates in the scattering event. Depth information can be determined relatively, or absolutely in some cases, by comparing inelastic energy loss due to interaction with atomic electrons.

The data in a RBS energy spectrum is counts versus channel, where channel number is linearly proportional to energy of backscattered beam particles. The counts per channel is proportional to the areal density of atoms of a specific atomic mass that the ion interacted with in the sample material. Volumetric densities and concentrations can be extracted by assuming the densities of target materials. Figure 6.1 shows an example RBS energy spectrum from 50 nm Si/60 nm $Si_{0.8}Ge_{0.2}$/Si heterostructure grown by molecular beam epitaxy, a slow and exacting way to grow films [20, 26]. Counts obtained from incident ions backscattering off of heavier Ge atoms are in the isolated peak at higher channel number, which corresponds to

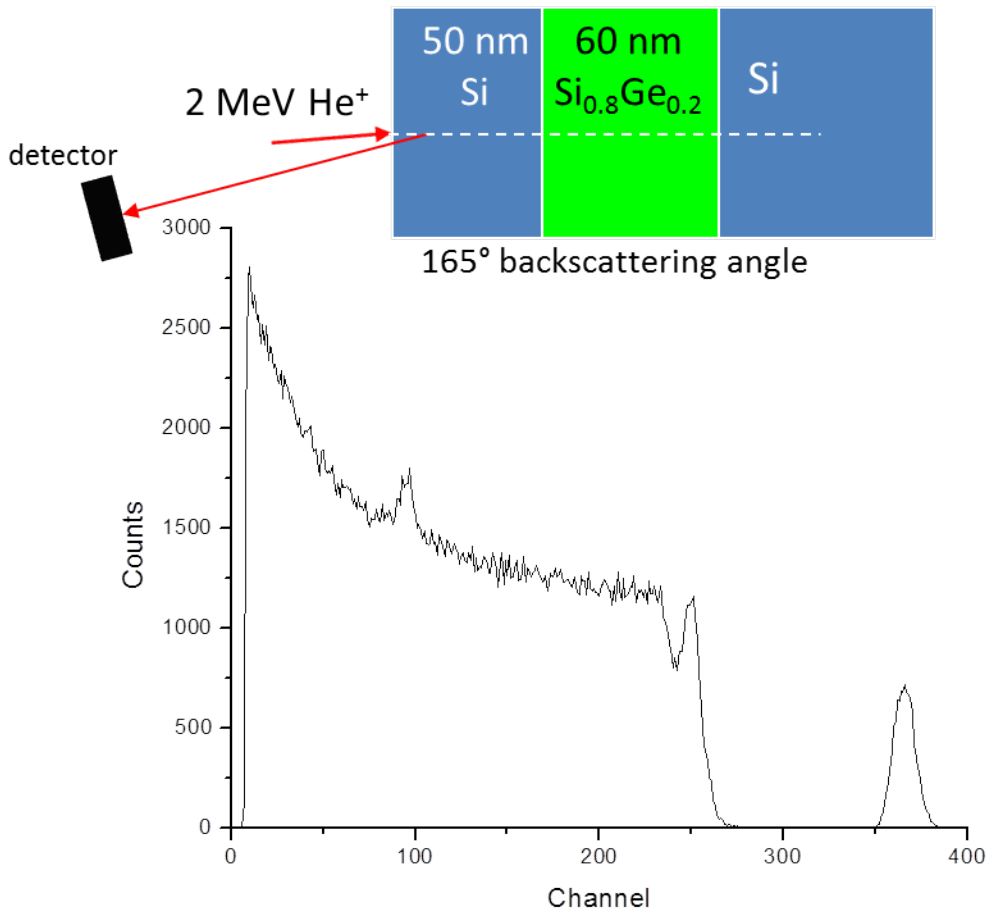

Figure 6.1: Energy spectrum of He ions backscattered 165° from 50 nm Si/60 nm $Si_{0.8}Ge_{0.2}$/Si heterostructure.

higher energy, and counts from lighter Si atoms make the continuum starting at lower channel number, or lower energy. The depletion of Si atoms in the 60 nm thick $Si_{0.8}Ge_{0.2}$ layer is shown by the dip in the Si counts below the surface. The peak at low energy on top of the Si continuum is from carbon deposited on sample surface during RBS analysis.

The ideal backscattering spectrum from a pure material with uniform density has uniform backscattering yield starting at backscattering energy KE_O, which is from ions backscattering from the surface of material, extending to backscattering energy $<< KE_O$. The uniform backscattering yield in each channel (backscattering energy bin) indicates that density of the material does not vary with depth, and that there is little or no noise in the detector electronics. In practice, a logarithmically increasing "tail" of low energy noise is overlaid on every backscattering energy spectrum, but the effect of this can be minimized with properly functioning electronic components and careful experimental design. Also, backscattering from the surface does not appear like the desired step function, but rather has some slope and few counts at higher energy.

RBS is performed in a vacuum chamber with the sample mounted to a goniometer which can manipulate the sample position and orientation with high accuracy (± 0.0005" for translation, $\pm 0.05^\circ$ for rotation). Figure 6.2 shows a schematic of an incoming ion beam incident on a goniometer with a solid state detector at a fixed backscattering angle.

6.1.1 Energy loss due to elastic scattering

For a nuclear, elastic scattering event, the target atom mass M_2 must be greater than the incoming particle mass M_1 for backscattering to occur. The change in energy, $\Delta E = E' - E_0$, for particle with mass M_1, incoming energy E_0 and outgoing

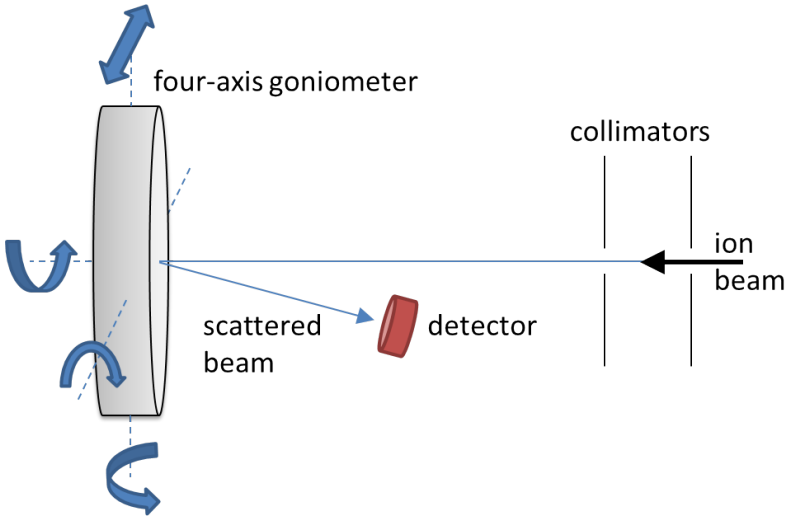

Figure 6.2: Schematic of four-axis goniometer and solid state detector. One axis is rotation of the sample about the beam, one is translation in one direction, and the final two axes are for tilting sample with respect to the beam. The energy of ions backscattered through a fixed solid angle is collected by the solid-state surface barrier detector.

energy E' which elastically scatters is determined by the angle through which M_1 scatters and the mass M_2 of the target atom which is initially at rest. In the laboratory frame of reference, for any combination of projectile mass M_1, target mass M_2 and scattering angle θ, the ratio of energy loss due to elastic scattering is found by solving the conservation of energy and momentum equations. Solving in terms of the ratio of scattered ion energy to incident ion energy gives the equation for K, the kinematic factor,

$$K = \frac{E'}{E_0} = \left[\frac{\left(M_2^2 - M_1^2 \sin^2\theta\right)^{1/2} + M_1 \cos\theta}{M_1 + M_2} \right]^2 \tag{6.1}$$

where E' is the energy of the backscattered ion entering the detector, E_0 is the energy

of the incoming ion beam, θ is the angle through which the ion is scattered in the laboratory frame of reference, and M_1 and M_2 are the masses of the projectile and target atoms, respectively [67]. Values for the kinematic factor K, though easy to calculate, are tabulated by Chu et al and Tesmer et al for common ion beams (e.g. H, He, Li) and target masses up to lead so that quick calibrations can be made to accurately determine the relation of output channel to energy[8, 67].

Rutherford backscattering analysis is best suited for detection of heavy elements on or near the surface of a lighter substrate. In a thick target, the backscattering signal from beam atoms penetrating deeply into the substrate before scattering will obscure the signal of elements with lower atomic mass than the substrate. High concentrations of light elements on the surface of a sample will be observed in the RBS energy spectrum, but this signal will be rendered unusable by the large background contributed by the substrate. Other methods of ion beam analysis such as particle-induced X- or γ-ray emission, elastic recoil detection and nuclear reaction analysis can be utilized if a particular material of interest will not produce satisfactory RBS data [67].

6.2 Channeling RBS

Ion channeling is achieved by aligning the ion beam with a crystal plane or axis in a monocrystalline material. Such alignment, usually within 0.5° or less, causes the backscattering yield to decrease by up to two orders of magnitude in a crystal with low defect concentration. Thermal vibrations of atoms in crystal decrease the width of channel, so measurements are performed on cooled samples or at room temperature. When the beam hits the surface of a material, ions that approach too close to atomic rows are scattered, creating a small peak in channeling backscattering spectra called the surface peak. At a depth near the surface, any remaining ions with

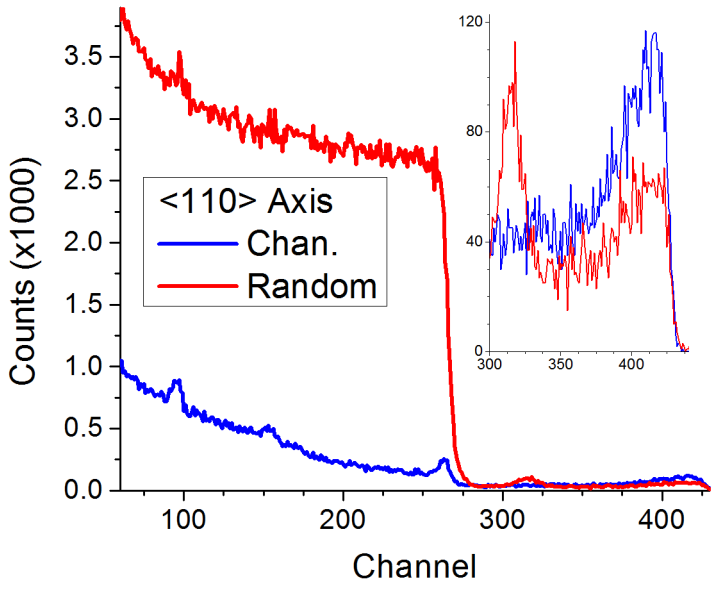

Figure 6.3: Random and channeled backscattering energy spectra from a 2 MeV He beam incident on Si containing buried Ag nanoparticles. Ion beam is aligned with the ⟨110⟩ axis in channeling spectrum.

trajectories unsuitable for channeling are scattered away.

Once the ions are inside the "channel", due to alignment with either crystallographic axis or atomic plane, interaction with atomic electrons has the effect of gently steering and focusing the ions. Essentially, the channeled ion is subjected to continuous electronic potentials due to the rows or atoms, and the inelastic energy loss due to interaction with atomic electrons is less in channeling mode compared to non-oriented random mode. However, there is also thermal vibration which stochastically changes the dimensions of the channel. A small amount of dechanneling is caused by these thermal vibrations which cause the dechanneled ion to encounter sample atoms under different alignment condition. The dechanneled ion can then elastically scatter and possibly contribute to the measured backscattering yield. The

way a channeled ion can be directly backscattered, instead of dechanneling then scattering, is by encountering a crystalline defect in its path.

6.2.1 Backscattering energy spectra

An energy spectrum of backscattered ions obtained by aligning the ion beam with a crystal axis or plane, referred to as a channeling spectrum, is compared to an energy spectrum obtained when the beam is not aligned with a crystal axis or plane, referred to as a random spectrum, to determine the crystallinity of material. Aligning the ion beam with crystal axis or atomic plane reduces the effective areal density of the material interacting with the beam, leading to the decreased backscattering yield. Adjacent to the specimen tilt angle corresponding to effective minimum areal density resulting from channeling the ion beam is a tilt angle corresponding to effective maximum areal density, and more on this can be learned from Fig. 6.4 on page 39. A random spectrum must be obtained by tilting the sample to an orientation such that the areal density is uniform and corresponds to bulk volumetric density of the material being analyzed.

Backscattering yield can be decreased by up to two orders of magnitude by aligning the ion beam within the critical angle of a crystal axis in a sample with low defect concentration. Figure 6.3 shows random spectrum and channeled spectrum measured from the $\langle 110 \rangle$ axis of (001)-oriented silicon containing silver nanoparticles with 2 MeV He analyzing beam. This spectrum is a key experimental result from this research project, and will be explained in that context in Chapter 9. The ideal random spectrum is a box, but this spectrum shows a number of non-ideal characteristics commonly encountered in RBS analysis. At lower energies, the tail of the random energy spectrum increases due to noise caused by overlap of counts. Around channel 90, the presence of carbon contamination on the surface of the sam-

ple, from oil in roughing and high vacuum pumps, is apparent. The small peak in the channeling spectrum around channel 150 is from silicon point defects near the silver nanoparticles. The silicon surface peak is around channel 265. Just below the surface peak, around channel 250, the counts from channeling and random spectrum can be compared to determine the minimum yield in this sample. The inset in Fig. 6.3 shows backscattering counts from silver atoms in the silicon sample. Silver on the surface of the sample is responsible for counts in highest channels, and buried silver is responsible for counts in lower channels. The random spectrum has a peak of buried silver areal density, but the channeling spectrum does not, indicating that silver atoms located in peak are not in the right crystallographic position to dechannel ions travelling in the $\langle 110 \rangle$ axis. The crystallographic position of defects, in this case silver atoms, can be elucidated by careful investigation using angular scanning, discussed later in this chapter.

6.2.2 Extracting quantitative data from RBS channeling

A simple way to extract quantitative data from channeling and random energy spectra is to compare the counts collected in the same channel of different spectra. The channeling yield, χ, is the ratio of the counts in the same channel of aligned and non-aligned energy spectra,

$$\chi = \frac{C^i}{\overline{C}_R} \tag{6.2}$$

where C^i is counts in channel i in an aligned energy spectrum and $\overline{C}_R$ is counts in channel i in a non-aligned, random energy spectrum. A control sample, unaltered by experiment, should also be used as a reference. This reference sample is commonly referred to as the "virgin" sample, and this terminology unfortunately persists. For

the control sample, unaltered by experiment, the channeling yield should be 1–4%, as stated in Subsection 6.2.3. The relative disorder, which can be normalized defect concentration in limited cases, n_D/n, in the axis being analyzed can be expressed as

$$\frac{n_D}{n} = \frac{\chi_E^i - \chi_V^i}{1 - \chi_V^i} = \frac{C_E^i - C_V^i}{\overline{C}_R - C_V^i} \tag{6.3}$$

where superscript i is the channel in all spectra, subscripts E and V refer to channeling spectra from experimental samples and virgin (reference) sample, subscript R refers to random spectrum, χ refers to channeling yield and C^i refers to counts in channel i as described in equation 6.2.

It must be noted that the random spectrum must be close to ideal for this comparison of channeled and random yield to be accurate. By definition, different depths are represented by the same channel number in random and channeling spectra. Different ion beam alignment conditions result in different amount of energy loss when an ion penetrates a given depth before scattering. If the material of interest is on the surface, this difference is negligible. However, increasing depth from the surface causes increasing separation of channels corresponding to same depth. For an ideal (or near-ideal) random backscattering energy spectrum, the backscattering yield changes little with increasing depth into the sample so that $\overline{C}_R\ C_R^i\ C_R^{i-10}\ C_R^{i+10}$ rendering this point moot.

6.2.3 Angular scanning

The angular "width" of the channel can be found by plotting counts versus tilting angle across the channel. This width indicates the allowable angle interval for the ion beam to be channeled [43]. This value can be calculated for any combination of incoming particle, target atom and ideal crystalline axis by the equation

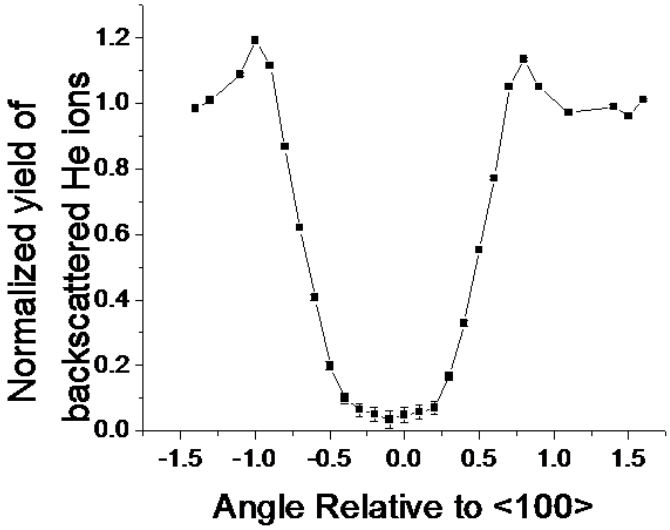

Figure 6.4: Backscattering yield from the near-surface region as a function of tilt angle across the $\langle 100 \rangle$ axis in bulk Si. The half-angle $\Psi_{1/2}$ is half of the full-width half-maximum of the dip.

$$\Psi_{1/2} = \sqrt{\frac{2Z_1 Z_2 e^2}{Ed}} \tag{6.4}$$

where Z_1 and Z_2 are the atomic numbers of the incoming ion and target atoms, respectively, e is the charge of an electron in coulombs, E is the energy of the incoming ion in MeV, d is the atomic spacing along the crystalline axis being probed in angstroms and the resulting value is given in units of degrees [8]. Thermal vibrations cause displacements of the atomic rows, and other crystalline defects can also cause irregularities in the atomic rows, so this value should be treated as an estimate.

The value $\Psi_{1/2}$ can be measured from an angular scan like Figure 6.4 by measuring the minimum yield value, χ_{min}, and measuring the angular width corresponding to a height determined by

$$\frac{1-\chi_{min}}{2}. \tag{6.5}$$

The measured angular width is $2\Psi_c \approx 2\Psi_{1/2}$ [21]. Experimentally measured values for the critical angle of the $\langle 100 \rangle$ axes for Si, Ge and W are 0.63°, 0.80° and 1.97°. Figure 6.4 shows an example of normalized yield of 2 MeV He ions backscattered from the near-surface region of bulk (100)-oriented Si as it was tilted through the $\langle 100 \rangle$ axis.

The backscattering yield of angular scans are normalized by using calculating the channeling yield of the desired energy range in channeling and random backscattered energy spectra. These data are plotted versus tilting angle, where the center of the axial channel is defined as 0°. The sample is rotated so that the tilting of the sample is not parallel to a plane channel, ensuring the beam does not strike a plane channel. Every axis is composed of the convergence of multiple atomic planes. More than a few degrees from the axis, the backscattering yield has no strong dependence on tilt angle. This condition is referred to as "un-aligned" or "random". As the beam approaches the axis (within 1–2°), it scans through a portion of effective maximum areal density, creating a "shoulder" in the yield curve. After the beam scans past this "shoulder" region, yield begins to decrease to values from 1–4% of the yield of the non-aligned portion of the curve, depending on the energy and species of the projectile and the target, and if the target is free of defects.

The position of defects can be determined by comparing angular scans across different crystalline axes. Preferred orientation of interstitial defects, for example, can be determined by investigation of two or three major axes. Tetrahedral interstitials in a face centered cubic and diamond-like lattices can be found by comparing angular

scans of the ⟨100⟩ and ⟨110⟩ axes, as shown in Figure 6.5. In the projection of the channel of the ⟨111⟩ FCC axis, tetrahedral interstitials are shielded by atomic rows. Helium atoms take tetrahedral positions in silicon and diamond, but the angular scans of ⟨110⟩ axis show single peak at center of axial channel instead of a bi-modal peak [2]. The tetrahedral interstice of diamond-like lattice measured experimentally is not a bi-modal peak centered in the channel, as Fig. 6.5 suggests, but a broad peak centered in the channel.

6.3 Transmission electron microscopy

The resolution limit of light microscopy is around one-half of the wavelength of light being used, so for green light with wavelength 500 nm, the smallest resolvable object must be larger than 250 nm. Electron microscopy is able to resolve smaller objects than light microscopy because the wavelength of 200 keV electrons is 2.5 pm [25]. An electron microscope is required to resolve voids and particles on the order of tens of nanometers. For this project, which has voids and nanoparticles at depth of several hundred nanometers buried inside silicon wafer, an electron beam probes a thin specimen of material containing voids and/or nanoparticles.

A transmission electron microscope consists of many components, shown in Figure 6.6. A focused beam of electrons with high energy originate from an electron source. The beam is manipulated by multiple apertures and electromagnetic or electrostatic lenses before and after penetrating the specimen to be analyzed. Finally, electrons are collected, and the manner in which the beam is manipulated determines the type of final "image", or micrograph, formed.

Bright-field TEM is the most common mode of operation, easiest to obtain and straight-forward to analyze. In the case of bright-field TEM, brighter spots correspond to low-Z material (with fewer atomic electrons) and darker spots to high-Z

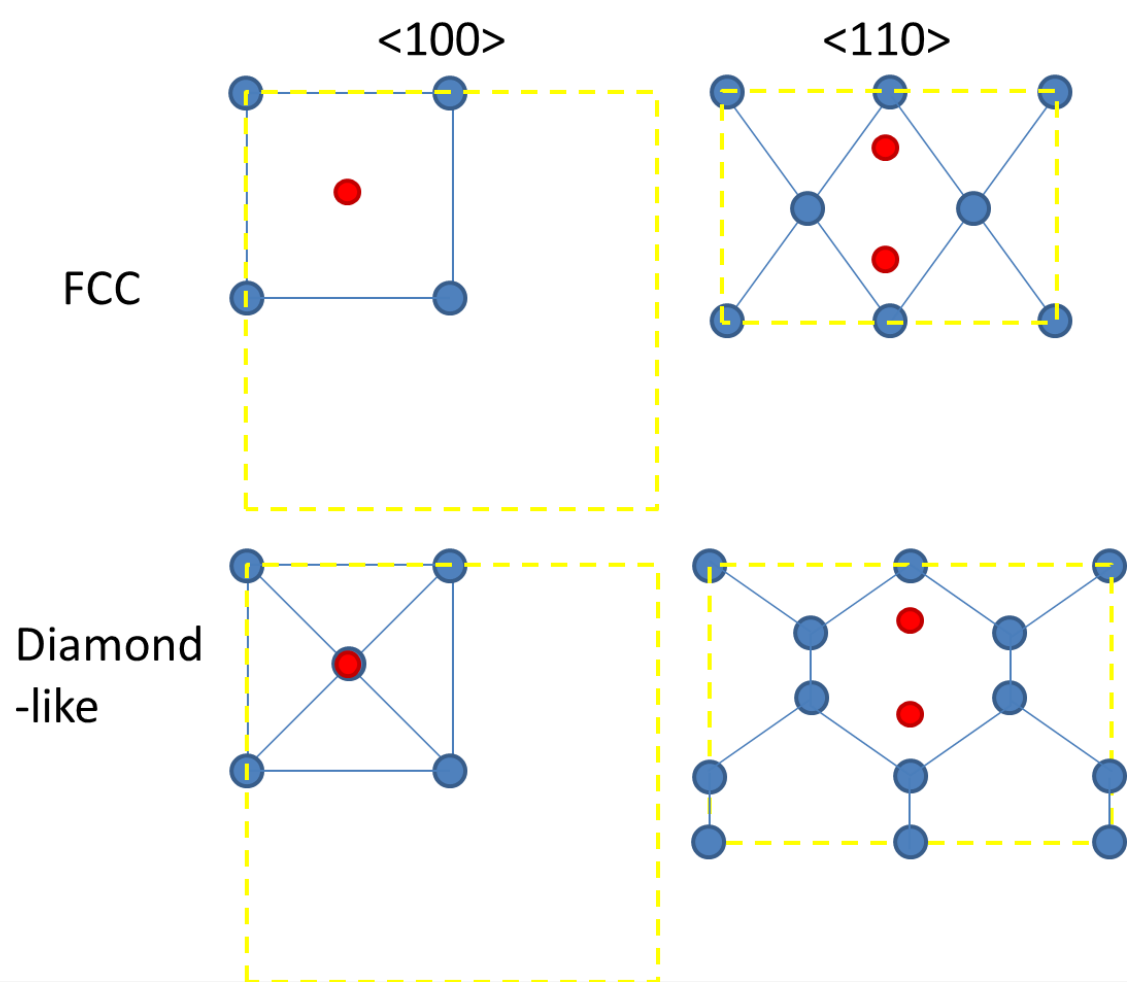

Figure 6.5: (blue) Lattice and (red) tetrahedral interstitial positions and their projection into the $\langle 100 \rangle$ and $\langle 110 \rangle$ axes of face-centered cubic (FCC) and diamond-like crystal structure. Yellow dashed lines outline one unit cell.

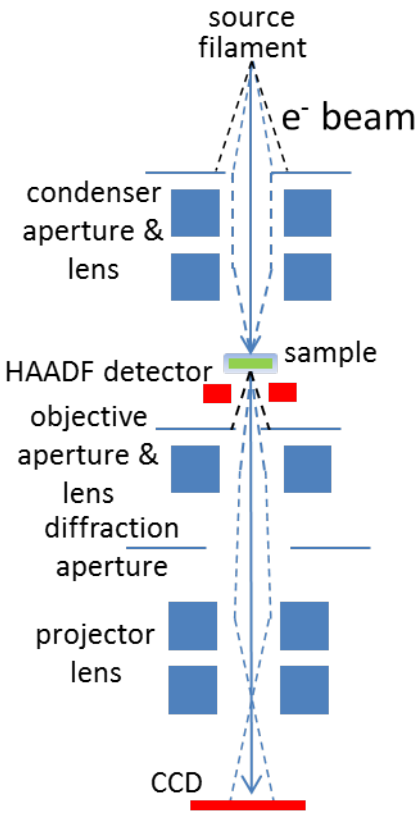

Figure 6.6: Schematic of transmission electron microscope.

material (with more atomic electrons). Other sources of contrast do not depend on the amount of electrons but can depend on the amount of stress/strain in the material, e.g. around a dislocation loop or the thickness of material if specimen is not uniform.

6.4 Electron diffraction

The beam of electrons made in a transmission electron microscope is coherent, meaning all electrons have the same velocity and phase. An electron diffraction pattern results from coherent scattering which satisfies Bragg's Law, shown in Eq. 6.6,

$$n\lambda = 2d\sin\theta \tag{6.6}$$

where n is an integer, λ is the wavelength of particle before scattering, d is the separation between neighboring atoms that cause scattering, and θ is the angle of incident particle. Constructive interference between particles scattered from different atoms occurs if the difference in distance traveled between the two is $2d\sin\theta$. Thus, spots in an electron diffraction pattern indicate the spacing of atomic planes that scattered the incident electron beam. For an electron beam hitting a monocrystalline specimen, the few spots indicate that Bragg's law is satisfied for that geometry, and the spatial separation and orientation of atomic planes can be determined by applying Eq. 6.6. Destructive interference causes the large area with no diffraction spots. For a polycrystalline sample, there are well defined rings that show the spacing of atomic planes but not orientation due to presense of crystals with many different orientations. The electron diffraction pattern from an amorphous material should not contain any sign of ordering, and should appear to be one big fuzzy dot.

6.5 Scanning TEM and energy-dispersive X-ray spectroscopy

Scanning TEM (STEM) is based on measuring highly scattered and secondary electrons from specimen using high-angle annular dark field (HAADF) detector placed near the back side of specimen, shown in Fig. 6.6. In the case of STEM, bright contrast indicates more atomic electrons, which means higher-Z atoms, and dark contrast indicates fewer atomic electrons, or lower-Z atoms. The electron beam is focused into a very small probe, possibly less than 1 nm diameter, and scanned or rastered over the area of interest. The intensity of highly scattered or secondary electrons collected in HAADF detector with probe on each pixel is then displayed as a scanning transmission electron micrograph.

Energy-dispersive X-ray spectroscopy is a technique to measure elemental concentration by the energy and relative quantity of X-rays emitted from specimen. The electron beam excites atomic electrons sufficiently for ejection from the atom, and characteristic X-rays are emitted when electrons in higher orbitals take the place of electrons ejected from more tightly-bound lower orbitals. The sensitivity of this technique is around 2 at.%.

7. DECORATION OF VOIDS IN SILICON BY GOLD ATOMS

7.1 Experimental methods

A limited number of successful experimental conditions have been found among a broad number of attempts. These parameters are summarized in Tables 7.1, 7.2 and 7.3. All experiments are performed on 300 um thick p-type silicon wafers with (001) orientation grown by float-zone technique doped with boron to resistivity $5-10$ $-cm$.

Table 7.1 details a straightforward approach consisting of forming voids by He ion irradiation and annealing followed by Au film deposition and diffusion heat treatment. Two high He ion fluences, 1×10^{17} and 5×10^{16} cm^{-2}, and two high temperatures for defect annealing, 750 and 950°C, for fixed time of two hours are investigated. After ion irradiation and defect annealing, 100 nm of Au is deposited by magnetron sputtering without any surface pre-treatment. Then, Au is diffused during 20 minute heat treatment at 750°C.

Both defect annealing and diffusion heat treatment are performed in vacuum utilizing a hot-zone approach, where samples are placed in quartz boat and inserted into the hot-zone of the furnace at stated temperature using transfer rod. Two minutes are added to each anneal or heat treatment to allow the sample and quartz boat to heat up to furnace hot-zone temperature.

An attempt to understand the role of the sequence of ion irradiation, defect annealing, metal deposition and diffusion heat treatment is attempted in experimental conditions listed in Table 7.2. The ion fluence for each of Au5-16 is fixed at 5×10^{16} cm^{-2} He ions. However, for Au5-13, 55 nm thick Au film is deposited before ion irradiation, and for Au14-16, 55 nm thick Au film is deposited after ion irradiation

Label	Fluence (cm^{-2})	Anneal Temp. (°C)	Anneal Time (hr.)
Au1	1×10^{17}	950	2
Au2	1×10^{17}	750	2
Au3	5×10^{16}	950	2
Au4	5×10^{16}	750	2

Table 7.1: Summary of experimental conditions attempted to fabricate gold nanoparticles in silicon. Following defect annealing, samples were deposited with 100 nm Au by magnetron sputtering, then heat treated for 20 minutes at 750°C to diffuse metal to voids. All annealing occurred in vacuum furnace.

and defect annealing. In order for He ions to penetrate to same depth in both cases, He ion energy for Au5-13 is set to 120 keV, and for Au14-16 to 100 keV. The goal of Au5-10 is to irradiate Si that has Au film on the surface with He ions and then anneal for one hour at temperatures ranging from $350 - 850$°C to study Au diffusion while voids are formed. The pressure in vacuum furnace for this series varies between $0.1 - 2 \times 10^{-6}$ torr while sample is in hot-zone. Before Au film deposition, samples are rinsed with acetone, methanol and DI H_2O five times, then held over open container of HF acid for 15 seconds "vapor etching" and finally rinsed in DI H_2O.

Void nucleation and metal diffusion do not necessarily have to be caused by separate processes. We investigate if the four step process with two heat treating steps, first investigated by samples Au1-4, can be decreased to three steps by conflating defect annealing and diffusion heat treatment into one heat treatment. The series of samples Au11-13 and Au14-16 are designed to be a direct comparison of the effect of the sequence of metal film deposition with one final heat treatment versus ion irradiation and defect annealing followed by metal film deposition and diffusion heat treatment. Samples Au11-13 are deposited with 55 nm thick Au film by magnetron sputtering, then implanted with 5×10^{16} cm^{-2} 120 keV He ions. After metal film deposition and ion implanation, each sample is subjected to a compound annealing

Label	Fluence (cm^{-2})	He^+ Energy (keV)	Anneal Temp. (°C)	Anneal Time (hr.)
Au5	5×10^{16}	120	350	1
Au6	5×10^{16}	120	450	1
Au7	5×10^{16}	120	550	1
Au8	5×10^{16}	120	650	1
Au9	5×10^{16}	120	750	1
Au10	5×10^{16}	120	850	1
Au11	5×10^{16}	120	500	1*
Au12	5×10^{16}	120	650	1*
Au13	5×10^{16}	120	800	1*
Au14	5×10^{16}	100	500	1
Au15	5×10^{16}	100	650	1
Au16	5×10^{16}	100	800	1

Table 7.2: Summary of experimental conditions attempted to fabricate gold nanoparticles in silicon. All annealing occurred in vacuum furnace. For samples Au5-13, Au film with thickness 55 nm deposited before He ion irradiation and subsequent annealing. For samples Au14-16, silicon wafers are first implanted with He ions, then annealed at listed temperatures. Following this defect annealing, 55 nm Au deposited and then samples annealed for an additional hour at 450°C in vacuum. Samples Au11-13 were subjected to compound annealing, where samples are first annealed at 450°C for one hour, then removed from hot zone and furnace turned up to listed temperature and sample annealed for one additional hour. The time between compound anneals is 20 minutes. This compound annealing step is undertaken so that total thermal budget for samples Au11-13 and Au14-16 are equivalent.

step, where samples are annealed for one hour at 450°C, then removed from hot-zone for 20 minutes. After 20 minutes, the samples are re-inserted into the hot-zone that has been heated to higher temperature, listed in Table 7.2, for additional hour. The purpose of this torturous heat treatment is so the thermal budget of samples Au11-13 matches those of samples Au14-16, which are subjected to separate defect annealing and diffusion heat treatment.

Samples Au14-16 are implanted with 5×10^{16} cm^{-2} 100 keV He ions first, then defects are annealed for one hour at temperatures listed in Table 7.2. Then, samples are deposited with 55 nm Au by magnetron sputtering and diffusion heat treatment of 450°C for one hours is applied.

Deposition of Au film leads to abundant diffusion of Au into Si, shown in results in section 7.2 of this chapter. Therefore, investigation proceeded involving low-fluence irradiation of 60 keV Au ions to limit the amount of Au atoms available to diffuse into silicon. The four-step process of He ion irradiation, annealing, metal ion irradiation and diffusion heat treatment are employed. Samples Au17-32 are implanted with 1×10^{17} or 5×10^{16} cm^{-2} 100 keV He ions. Defect annealing times are fixed to either 20 minutes or two hours at 350, 550, 750 or 950°C in quartz tube furnace utilizing hot-zone method. Then, samples are irradiated with 60 keV Au ions at University of Houston Ion Beam Laboratory to fluence 1×10^{15} cm^{-2} 60 keV Au ions, which are expected to penetrate 32 ± 6 nm [76]. Heat treatment for two hours at 750°C in flowing N_2 gas is applied to cause diffusion of Au to void region.

Following cross-sectional TEM analysis of samples in the series Au17-32, it was decided to try to Samples Au33-35 are implanted with 1×10^{16}, 1×10^{15} or 1×10^{14} cm^{-2} 100 keV He ions, respectively, and the rest of parameters are identical to Au17 (1×10^{17} cm^{-2}) and Au25 (5×10^{16} cm^{-2}). The purpose is to decrease void size and density so the number density of trapping sites for Au atoms would be decreased so

Label	Fluence (cm^{-2})	Anneal Temp. (°C)	Anneal Time (hr.)
Au17	1×10^{17}	950	2
Au18	1×10^{17}	750	2
Au19	1×10^{17}	550	2
Au20	1×10^{17}	350	2
Au21	1×10^{17}	950	0.33
Au22	1×10^{17}	750	0.33
Au23	1×10^{17}	550	0.33
Au24	1×10^{17}	350	0.33
Au25	5×10^{16}	950	2
Au26	5×10^{16}	750	2
Au27	5×10^{16}	550	2
Au28	5×10^{16}	350	2
Au29	5×10^{16}	950	0.33
Au30	5×10^{16}	750	0.33
Au31	5×10^{16}	550	0.33
Au32	5×10^{16}	350	0.33
Au33	1×10^{16}	950	2
Au34	1×10^{15}	950	2
Au35	1×10^{14}	950	2

Table 7.3: Summary of experimental conditions attempted to fabricate gold nanoparticles in silicon. Samples first implanted with 100 keV He ions then annealed in vacuum furnace for indicated time and temperature. Then, samples implanted with 60 keV Au ions to fluence 1×10^{15} cm^{-2} followed by diffusion heat treatment for two hours at 750°C in flowing N_2 gas.

that amount of Au trapped in each void might increase. Analysis of Au diffusion is performed by RBS analysis at UH Ion Beam Laboratory with detector positioned at 165° backscattering angle detecting backscattered ions from 2 MeV He ion beam incident in random mode.

The concentration of Au as a function of depth from surface is measured by RBS in random mode utilizing 2 MeV He ion beam. A surface barrier detector is set at 165° backscattering angle in IBM geometry at University of Houston Ion Beam Laboratory.

Cross-sectional TEM specimens are made by mechanical polishing, dimpling and Ar ion milling. Specimens of sample Au1 are made after ion irradiation, after ion irradiation and defect annealing, and after ion irradiation, defect annealing, metal film deposition and diffusion heat treatment. Specimens of samples Au12, -13, -18, -25, -26, -29 and -33 are fabricated by traditional mechanical method. These specimens are analyzed in JEOL JEM-2010 transmission electron microscope or FEI Tecnai G2 F20 ST FE-TEM transmission electron microscope, both operated at 200 kV, in the Microscopy and Imaging Center at Texas A&M University.

7.2 Experimental results and discussion

There are multiple steps to creating each sample, and Figure 7.1 shows transmission electron micrographs of silicon wafer after **A** irradiation with 1×10^{17} cm^{-2} 100 keV He ions, **B** after irradiation (shown in **A**) and defect annealing at 950°C for two hours, and **C** after irradiation and defect annealing (shown in **B**) followed by 100 nm Au film deposited on surface and diffusion heat treatment at 750°C for 20 minutes. The large amount of disorder following irradiation with 1×10^{17} cm^{-2} 100 keV He ions results in a thick band of defects, and annealing at 950°C for two hours results in defect recombination and evolution into larger structures. Helium

gas desorbs from from silicon sample in a few minutes at this annealing temperature [9].

Rutherford backscattering spectra from samples Au1-4, described in Table 7.1, are obtained to determine the amount of gold that diffuses and if gold is preferentially trapped at voids. These data, shown in Figure 7.2, indicate that gold diffuses readily into silicon following irradiation and defect annealing. There is also a small peak in front of the Si peak that shows that Si diffuses into Au surface layer in Au1, indicating the formation of gold silicide compound. However, no preferential trapping is measured by RBS or TEM.

Analysis by TEM and RBS of samples Au1-4, shown in Figures 7.1 and 7.2, show that the method used to fabricate the samples results in large voids, around 50 nm, at the end of range of 100 keV He ions. However, no nanoparticles are seen in TEM and no significant amount of Au trapping is measured by RBS. Gold diffuses too readily into silicon, with the diffusion tail possibly obscuring a small amount of gold atoms trapped on inner surface of voids. The binary phase diagram of Au-Si shows that Au and Si are immiscible, with a eutectic point when Au concentration is 18.6 at%. The diffusion heat treatment temperature is 750°C, but the Au-Si eutectic temperature is 363°C [50]. It is desirable to avoid formation of liquid phase Au-Si. However, thermally driven diffusion below the eutectic temperature would require diffusion times of hundreds of hours or more for Au to diffuse to voids at depth around 650 nm.

Decreasing the thermal budget for annealing and heat treatment and changing the order of ion irradiation and Au film deposition are investigated for several conditions listed in Table 7.2. The possibility of accomplishing the dual goals of void nucleation and metal diffusion in one annealing step are investigated. Samples Au5-10 are float zone Si(100) wafers deposited with 55 nm Au by magnetron sputtering,

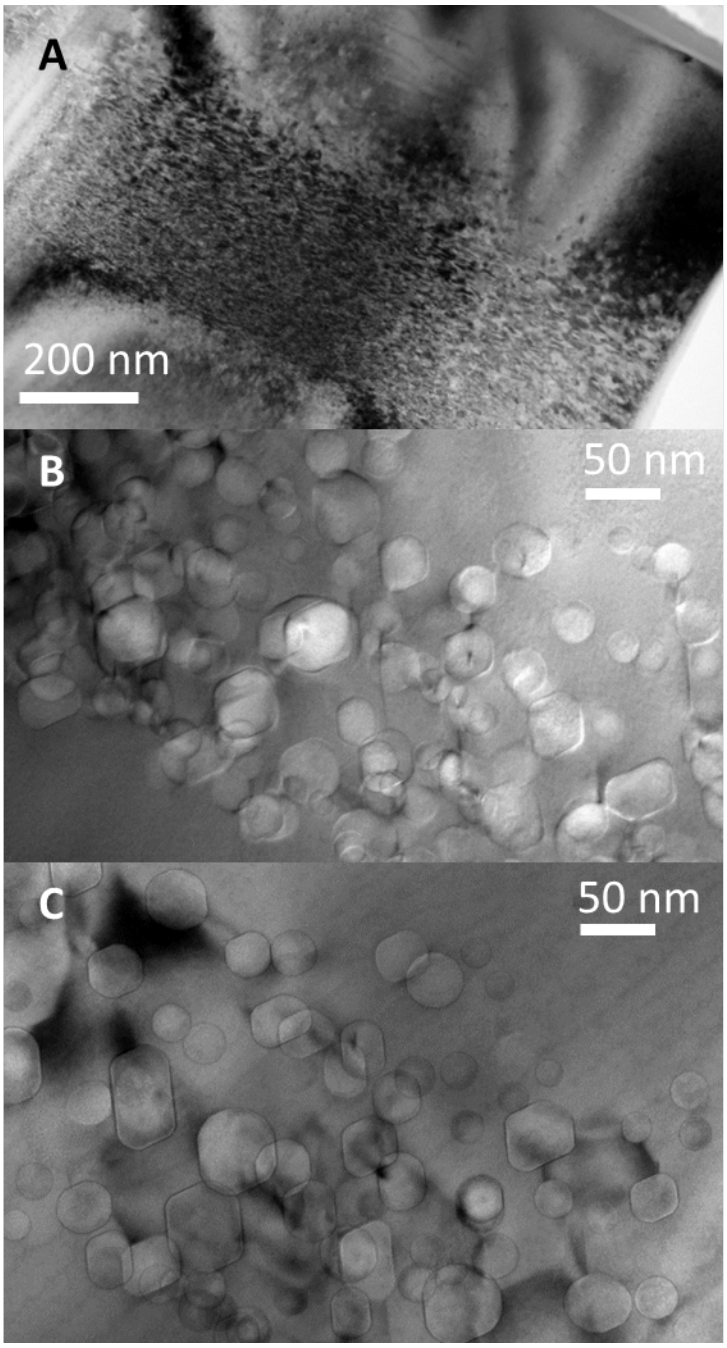

Figure 7.1: Cross-sectional transmission electron micrographs of sample Au1 after different stages of fabrication process. **A** following irradiation with 1×10^{17} cm^{-2} 100 keV He ions. **B** after irradiation shown in **A** and defect annealing at 950°C for two hours. **C** after irradiation and defect annealing shown in **A** and **B** followed by 100 nm Au film deposited on surface and diffusion heat treatment at 750°C for 20 minutes.

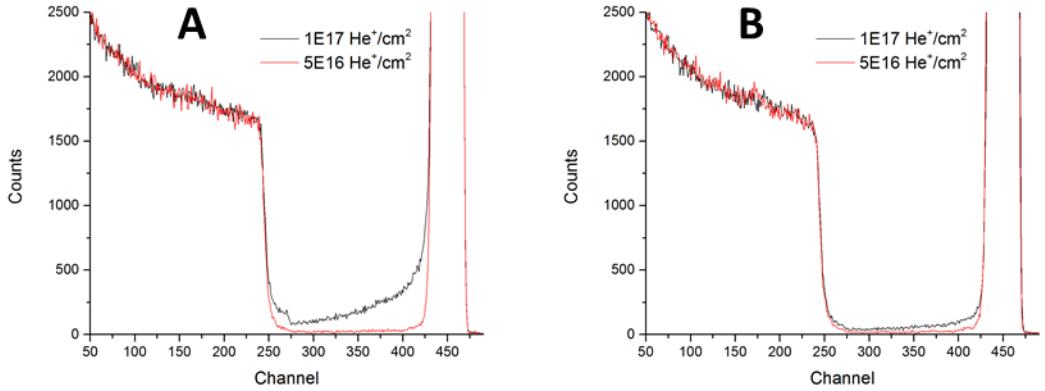

Figure 7.2: Rutheford backscattering spectra **A** from samples Au1 and -3, annealed at 950°C for two hours following He ion irradiation to stated fluence and **B** from samples Au2 and -4, annealed at 750°C for two hours following He ion irradiation to stated fluence. Following defect annealing for two hours, all samples are deposited with 100 nm Au film by magnetron sputtering and heat treated for 20 minutes at 750°C to diffuse metal inside sample.

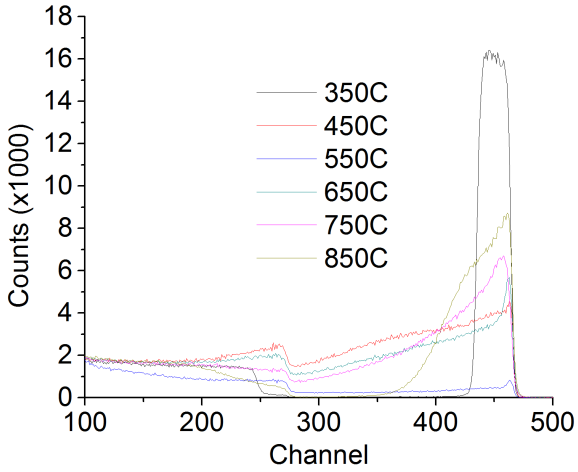

Figure 7.3: Rutheford backscattering spectra showing Au diffusion into Si wafer from samples Au5-10. Samples are deposited with 100 nm Au film by magnetron sputtering then implanted with 100 keV He ions to fluence 5×10^{16} cm^{-2}. Void nucleation and metal diffusion are attempted in one annealing step for one hour at specified temperatures.

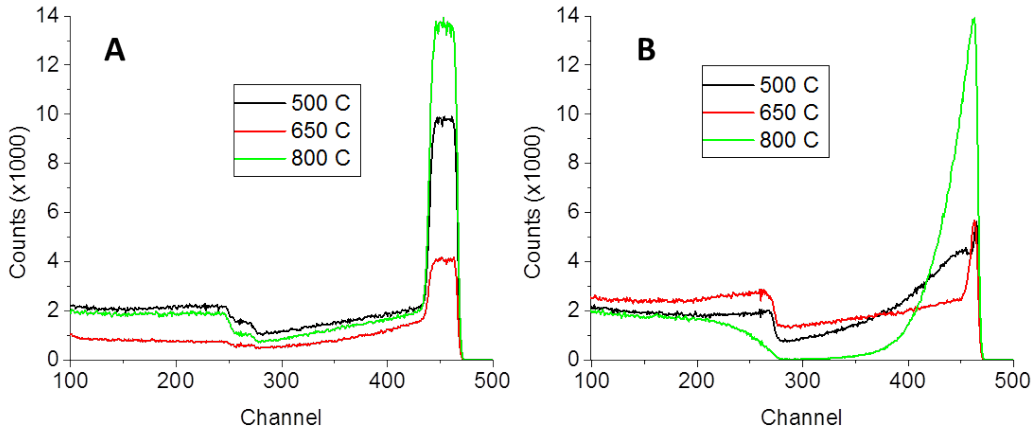

Figure 7.4: Rutheford backscattering spectra showing Au diffusion into Si wafer from samples **A** Au14-16 and **B** Au11-13. The effect of changing the order of ion irradiation and Au film deposition are investigated. Thermal budget for all samples are equal, and further details are found in Table 7.2.

followed by irradiation with 5×10^{16} cm^{-2} 100 keV He ions and one hour treatment at temperatures ranging from $350 - 850$°C. Results for Au diffusion are determined by RBS, and shown in Figure 7.3. The least diffusion occurs in annealing at 350°C, which is expected because that is the lowest temperature and below the eutectic point, but the next lowest amount of Au diffusion from the surface is caused by annealing for one hour at 850°C. The least amount of Au is left on the surface by annealing at 550°C. The diffusion of Au from surface into bulk is maximum at this temperature, 550°C, and decreases as temperature is lowered to 350°C as well as when temperature is raised to 850°C.

The results for Au diffusion determined by RBS for samples Au11-16 are shown in Figure 7.4. The effect of the order of He ion irradiation and Au film deposition are investigated. The results from samples Au14-16 are shown in **A**, the case of He ion irradiation and defect annealing followed by metal film deposition and diffusion heat

treatment. Gold is most efficiently diffused into the bulk after defect annealing at the intermediate temperature, 650°C in this case. The results from samples Au11-13 are shown in **B**, the case of metal film deposition followed by He ion irradiation and annealing. These three curves show varying degrees of diffusion of Au into the bulk, but nothing that indicates the results are particularly promising for nanoparticle formation.

Transmission electron micrographs showing overviews of damaged layer and small nanoparticles near the Si surface are shown in Figures 7.5 and 7.6. The effect on void size due to annealing at 650°C, in Fig. 7.5**A**, and 800°C, in Fig. Fig. 7.6**A**, is significant. Lower temperature does not evolve voids or anneal out most of the disorder, whereas higher temperature creates large voids and anneals out other defects besides dislocations. The nanoparticles formed near the Si surface shown in Fig. 7.5**B** are sperical and less than 1 nm diameter, and those formed in Fig. 7.6**B** are spherical and around 2 nm diameter. Transmission electron micrographs and RBS data, shown in Fig. 7.4, show that there are voids, at least in Au13, and an abundant amount of Au diffused into Si substrate, but no Au is trapped in voids.

One strategy to limit the excess Au atoms that diffuse into Si because of heat treatment is to implant low energy Au ions into Si wafers after defect annealing instead of depositing a film on the surface, thereby limiting the amount of Au in the system. Samples Au17-35 are irradiated with 60 keV Au ions to fluence 1×10^{15} cm^{-2} in order to limit the number of Au atoms available to diffuse into Si.

RBS spectra obtained in random mode from samples Au17, -18, -25 and -26 are shown in Figure 7.7. Inset shows channel range which has backscattering yield from Au atoms in Si. The curve labelled "No Diff. H.T." is taken from a Si sample irradiated with Au ions but not heat treated to cause Au diffusion, and shows distribution of irradiated Au ions. The rest of the curves show that a portion of irradiated Au

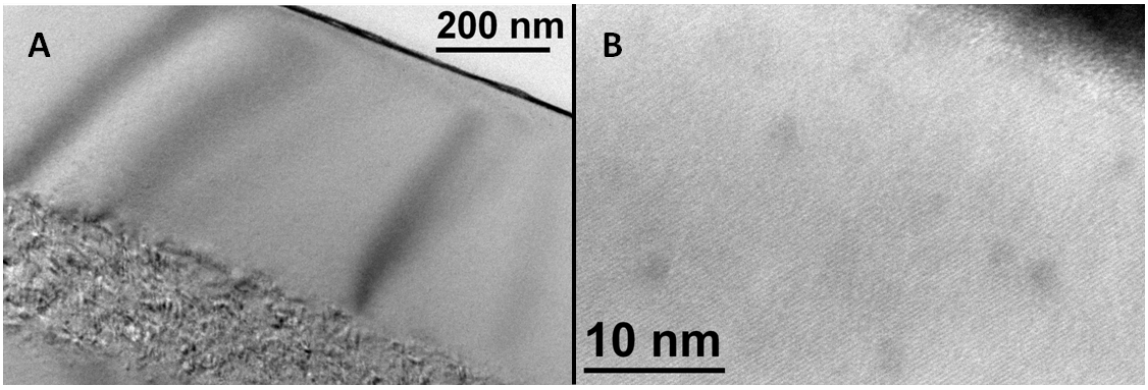

Figure 7.5: Transmission electron micrograph cross-sections of sample Au12. **A** is an overview of surface and defect band that does not appear to contain void. **B** is higher resolution micrograph showing possible small nanoparticles formed in the near-surface region.

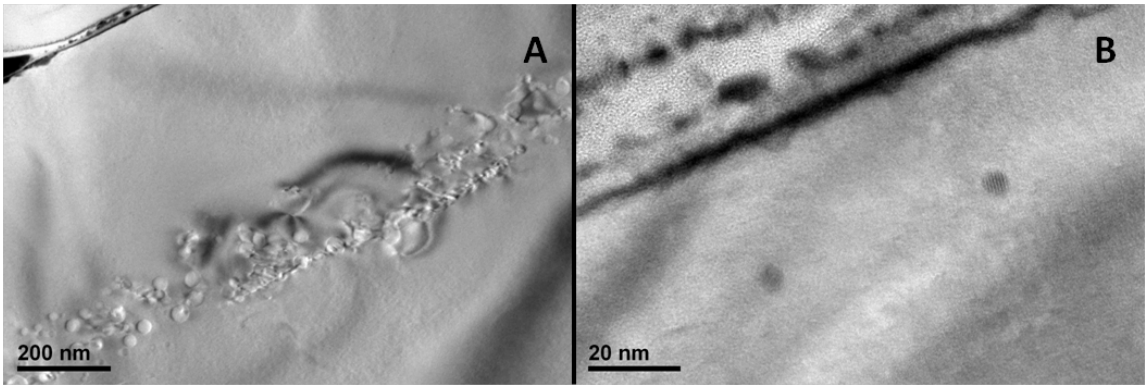

Figure 7.6: Transmission electron micrograph cross-sections of sample Au13. **A** is an overview of surface and void region. **B** is higher resolution micrograph showing small nanoparticles formed near the surface.

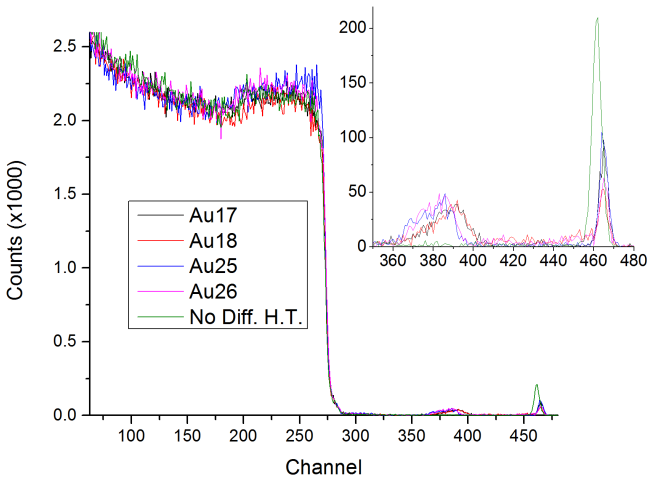

Figure 7.7: Rutherford backscattering spectra from samples Au17, -18, -25 and -26. Samples Au17 and -18 have been irradiated with 1×10^{17} cm^{-2} and samples Au25 and -26 with 5×10^{16} 100 keV He ions. Defect annealing for two hours is performed at 950°C for Au17 and -25, and 750°C for Au18 and -26.

remains near surface and a portion diffuses to voids. Another feature of these curves is the odd shape of the Si backscattering yield.

Figure 7.8 shows the random RBS spectrum from sample Au26 plotted with a simulated RBS spectrum obtained using the RBX simulation code [39]. The thicknesses and concentrations of Au layers extracted by simulation are estimates based on assumption of bulk density of Au and that the only two elements measured are Au and Si. The simulation shows that there is a region 170 nm wide where Au is trapped. One feature not accurately described by the simulation is Si from surface to depth 660 nm, near the projected range of He ion irradiation. Either this surface layer of Si has higher density than bulk Si or the voided layer has significant depletion of Si, or both. If there is a depletion of Si, it is not symmetric and extends beyond projected range of He ion irradiation.

Transmission electron micrographs showing surface through void region of sam-

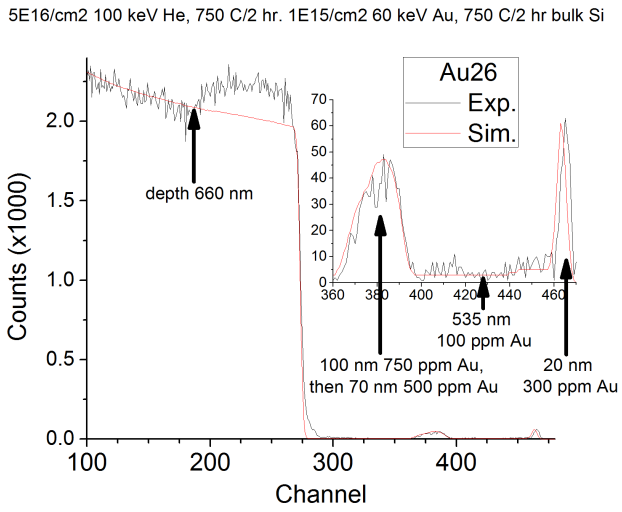

Figure 7.8: Simulated and experimental Rutherford backscattering spectra from samples Au26. The thicknesses extracted by simulation are based on assumption that Au nanoparticles have bulk density of 19.30 g cm^{-3}.

ples Au26 and -18 are shown in Figure 7.9**A** and **C**, respectively. The difference between the two samples is Au26 has lower He ion irradiation fluence than Au18 by a factor of two. The significantly decreased width of the void layer in Fig. 7.9**A** compared to **C** reflects this difference. The near surface regions of Au26 and -18 are shown in Fig. 7.9**B** and **D**, and nanoparticles are created in this region in both samples. According to RBS spectra in Fig. 7.7, Au26 and -18 have similar quantity of Au atoms throughout depth of interest, except Au26 has slightly more Au trapped in void layer than Au18. Despite the number of nanoparticles observed near the surface, and Au trapped in void layer measured by RBS, no nanoparticles are observed in void layer. Monolayer or less coverage of voids near projected range of He ion irradiation is likely.

Trapping of Au atoms in void layer in samples Au21, -22, -29 and -30 is large according to Figure 7.10, larger than trapping observed for samples Au17, -18, -

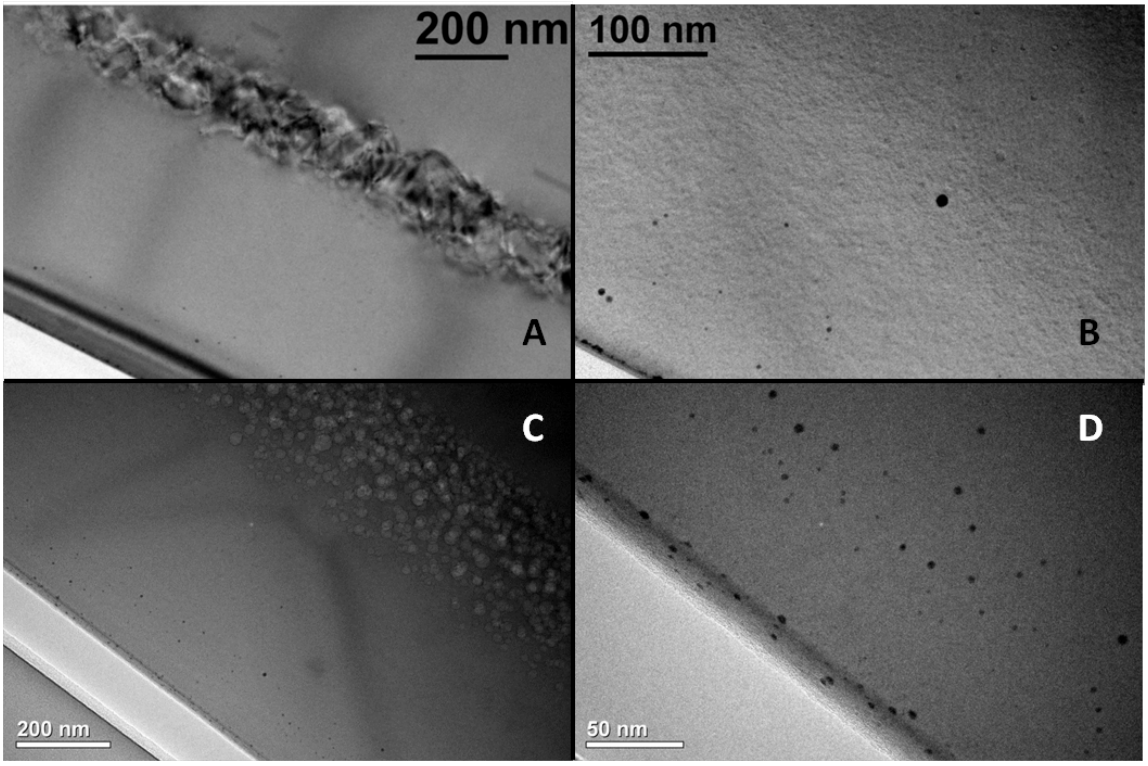

Figure 7.9: Cross-sectional transmission electron micrographs of samples **A** and **B** Au26 and **C** and **D** Au18 implanted with 100 keV He ions to fluences 5×10^{16} and 1×10^{17} cm^{-2}, respectively. **A** and **C** are overviews of surface and void regions. **B** and **D** are higher resolution micrographs showing small nanoparticles formed near the surface.

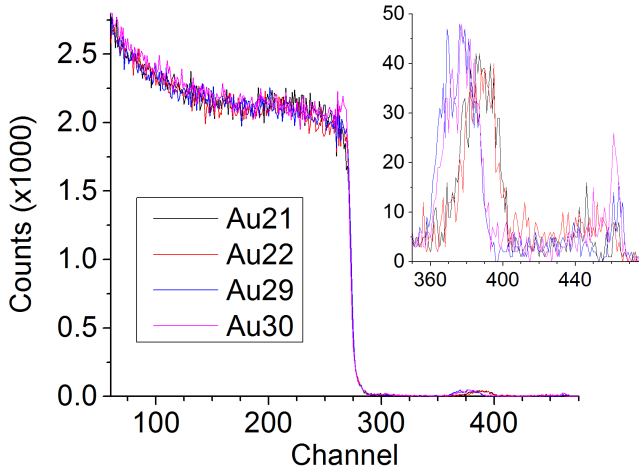

Figure 7.10: Rutherford backscattering spectra from samples Au21, -22, -29 and -30. Samples Au21 and -22 have been irradiated with 1×10^{17} cm^{-2} and samples Au29 and -30 with 5×10^{16} 100 keV He ions. Defect annealing for 20 minutes is performed at 950°C for Au21 and -29, and 750°C for Au22 and -30.

25 and -26 in Figure 7.7. The difference between the sets of four samples is that Au21, -22, -29 and -30 are annealed for 20 minutes, whereas Au17, -18, -25 and -26 are annealed for two hours. Therefore, samples shown in Fig. 7.10 have more residual defects. Diffusion of Au is greater for lower thermal budget defect annealing compared to higher thermal budget defect annealing, shown by increased trapping of Au in void layer and dramatically decreased retention of Au atoms at Au ion irradiation range.

Transmission electron micrographs from two samples irradiated with 100 keV He ions to fluence 5×10^{16} cm^{-2} followed by defect annealing at $950C$ for two hours and 20 minutes are shown in Figure 7.11**A** and **B**, respectively. The band of defects at projected range of 100 keV He ion irradiation created by longer annealing time in **A** has more voids and fewer dislocation-type defects than defect band created by shorter annealing time in **B**. Insets in each micrograph contain nanoparticles that

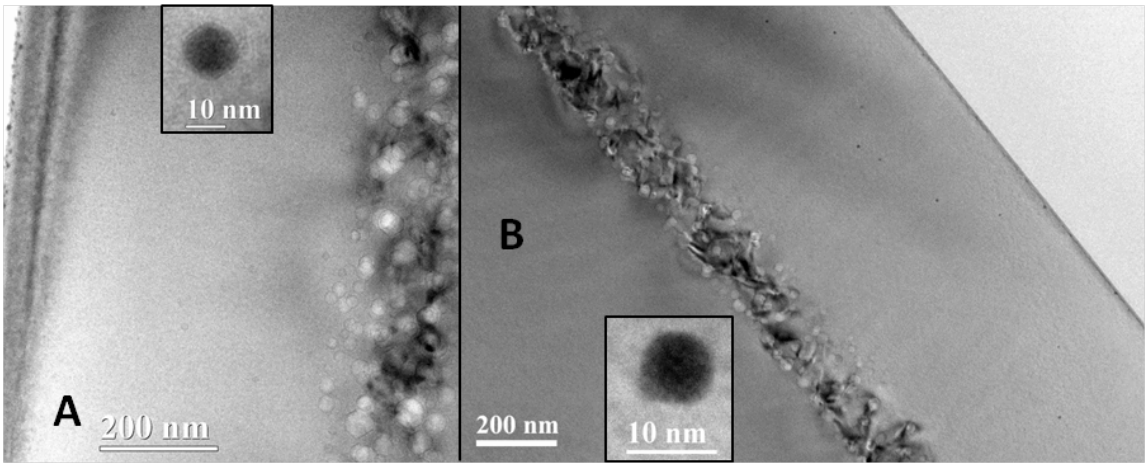

Figure 7.11: Cross-sectional transmission electron micrographs of samples **A** Au25 and **B** Au29 implanted with 100 keV He ions to fluence 5×10^{16} cm^{-2} and annealed at 950°C for two hours and 20 minutes, respectively. Insets in both show nanoparticles that form near the surface.

are formed near the surface, and longer annealing time creates larger near-surface nanoparticles. However, similar to other cases, Au trapping determined by RBS does not result in nanoparticle formation in void region, indicating that small amount of Au is trapped in each void or trapped in other types of defects.

In general, voids are difficult to image using TEM. However, changing the focusing condition of the transmitted electron beam increases the Fresnel contrast of edges of voids. The method used to image voids is generally referred to as the under-focus over-focus method, named for progression of micrographs in under-focused, in-focus and over-focused conditions that is used to determine void location and size. In the case of TEM results shown from samples investigated thus far, voids are relatively easy to image because of known location and high density.

Analysis by RBS in random mode shows that measurable amount of Au atoms are trapped in void layers, but does not indicate what defects are trapping Au atoms. The question of coverage of inner surfaces of voids with thin layers, even monolayers

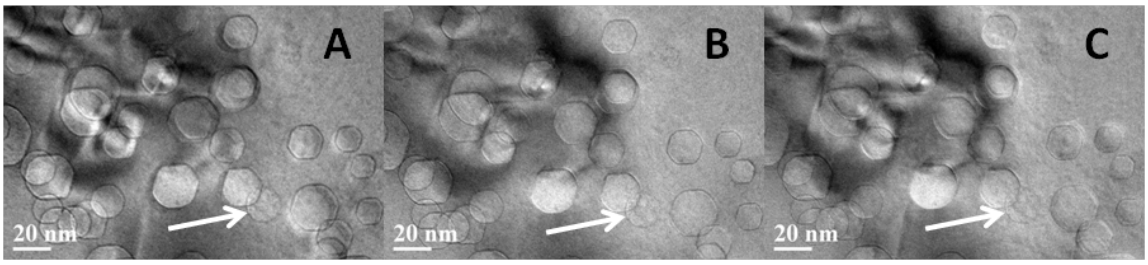

Figure 7.12: Cross-sectional transmission electron micrographs of sample Au29 in **A** under-focused **B** in focus and **C** over-focused condition. Even by using this technique, the density of bubbles makes it difficult to determine if Au atoms are coated on inner surface.

or less, with Au atoms is not resolved by TEM results already displayed. Figure 7.12 shows a series of micrographs obtained with electron beam **A** under-focused, **B** in-focus and **C** over-focused. If there is no thin layer of Au, then each void should be almost invisible in micrograph that is in-focus, and contrast should be greater when micrograph is slightly out-of-focus. Of all voids shown in region probed by micrographs in Fig. 7.12, the only one which exhibits normal void contrast is indicated by white arrow. It is almost spherical. There are a number of other voids that either do not exhibit the same behavior or are not spherical or both. One possible reason for the expected contrast change to be exhibited by one void and no others is that no other voids are located at the same position in the specimen with respect to the electron beam. However, there are many voids and this seems unlikely. The under-focus over-focus analysis does not prove that some voids have monolayer of Au adsorbed on inner surfaces, but it does show that contrast changes normally associated with changing electron beam focusing conditions are not followed by at least some voids.

The diffusion of Au atoms in samples that have defects annealed at 350 and 550°C for 20 minutes or two hours following He ion irradiation are shown in Figure 7.13.

All samples are irradiated with 100 keV He ions to fluences **A** 1×10^{17} or **B** 5×10^{16} cm^{-2}. Sample Au27, in Fig. 7.13**B**, shows an unusual tri-modal Au distribution instead of the normal bi-modal distribution expected from near-surface irradiation and buried Au trapping layer. The tri-modal distribution, also seen less conclusively in random RBS spectra in Fig. 7.13**A**, indicates that there is an intermediate defect peak, possibly at depth corresponding to one-half the projected range of He ion irradiation ($R_p/2$), that traps Au atoms diffusing from near-surface. The irradiation fluence of four samples shown in Fig. 7.13**A** is factor of two greater than four samples shown in **B**, so quantities of residual defects in each of four samples in **A** are greater than counterparts in **B**. Of all eight samples with RBS data displayed in Fig. 7.13, sample Au27 has lowest He ion irradiation fluence, 5×10^{16} cm^{-2}, and highest thermal budget of defect annealing, 550°C for two hours. Sample Au19 has same defect annealing thermal budget but higher He ion irradiation fluence. Weak intermediate Au trapping peak is observed in **A** from four samples with most defects, and strong intermediate Au trapping peak is observed in sample Au27, which has the least residual point defects of any of eight samples shown in Fig. 7.13. Low temperature defect annealing and the observed intermediate Au trapping peak are of little utility to the stated goals of this project, but should be studied for sake of understanding intermediate $R_p/2$ defect behavior. No TEM specimens are made of any samples investigated by RBS in Fig. 7.13 which could elucidate this question.

Samples Au33-35 are irradiated with decreasing He ion irradiation fluence in order to limit the number of Au trapping sites in order to acheive nanoparticles with measurable size at projected range of 100 keV He ions. Random RBS spectra in Figure 7.14 obtained from these samples show that appreciable Au trapping in void region is limited to sample Au33, and extremely limited amount of Au is trapped in void region in samples Au34 and -35. RBS curves of samples Au34 and -35 also show

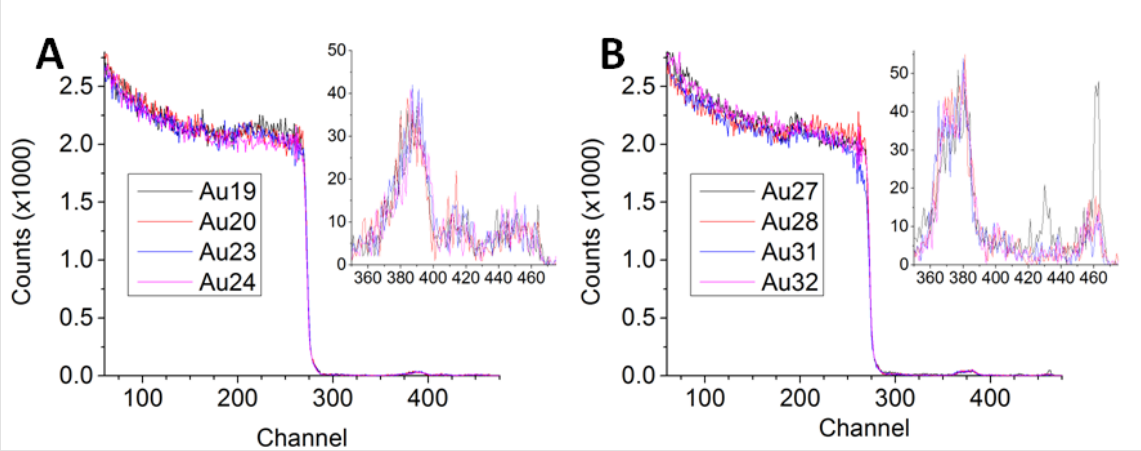

Figure 7.13: Rutherford backscattering spectra showing Au trapped in samples **A** Au19, -20, -23, and -24 and **B** Au27, -28, -31 and -32. Samples measured in **B** have more Au atoms trapped in void region than **A**, and Au27 in **B** appears to have significant amount of Au atoms trapped at an intermediate peak.

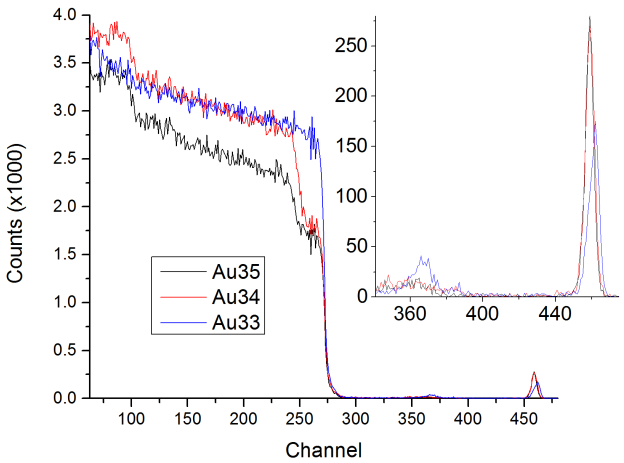

Figure 7.14: Rutherford backscattering spectra showing Au trapped in samples Au33, -34 and -35. Samples have identical fabrication parameters except for decreasing fluence of 100 keV He ions: Au33 1×10^{16}, -34 1×10^{15} and -35 1×10^{14} cm^{-2}. Ion fluences of 1×10^{15} and 1×10^{14} cm^{-2} do not cause Au atoms to diffuse from surface into bulk, based on comparison with "No Diff. HT" curve in Fig. 7.7.

significant surface contamination, indicated by decreased yield of Si and increased yield of O at surface. Sample Au34 has a thin oxidized surface layer, but sample Au35 has surface oxide layer more than 1 μm thick. The effect of oxidation on diffusion of Au is not known.

Spectrum of sample Au33 shows that there is no surface oxidation, Au atoms are trapped at an intermediate position between projected ranges of Au and He ion irradiation near to void layer, and that Au diffuses from near-surface to void layer. The experimentally obtained random RBS spectrum is simulated using RBX, and simulated and experimental spectra are plotted in Figure 7.15 [39]. The comparison of simulated spectrum assumes only Si and Au are present in sample Au33, and that Au atoms have bulk Au density. Layer thicknesses and concentrations of Au are estimates. The backscattering from Si shows that there are no variations in density of Si throughout depth of interest and beyond, unlike sample Au26 shown in Fig. 7.8. The region with significant amount of Au trapping is 90 nm wide, according to simulation.

Figure 7.16 contains micrographs from Au33 cross-sectional TEM specimen. The overview micrograph, **A**, shows some small particles with dark contrast interspersed in dislocations. Micrographs in Fig. 7.16**B** and **C** show partially and fully filled nanoparticles, respectively, surrounded by voids. No nanoparticles are observed near the surface, as in several other samples shown previously. Gold atoms decorate voids in void layer.

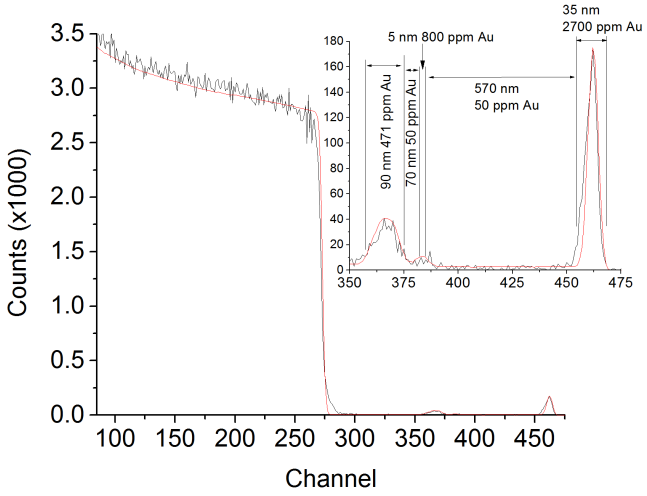

Figure 7.15: Simulated and experimental Rutherford backscattering spectra from sample Au33. The thicknesses extracted by simulation are based on assumption that Au nanoparticles have bulk density of 19.30 g cm^{-3}.

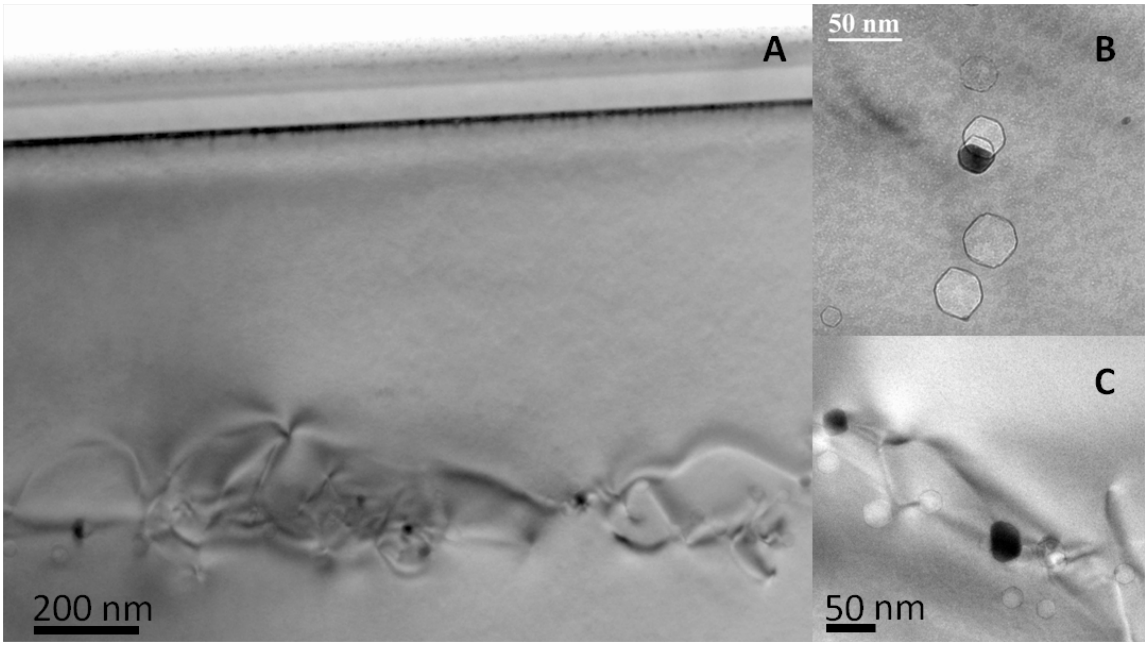

Figure 7.16: Cross-sectional transmission electron micrographs of sample Au33 **A** overview **B** void partially filled with Au atoms and **C** voids fully filled with Au atoms.

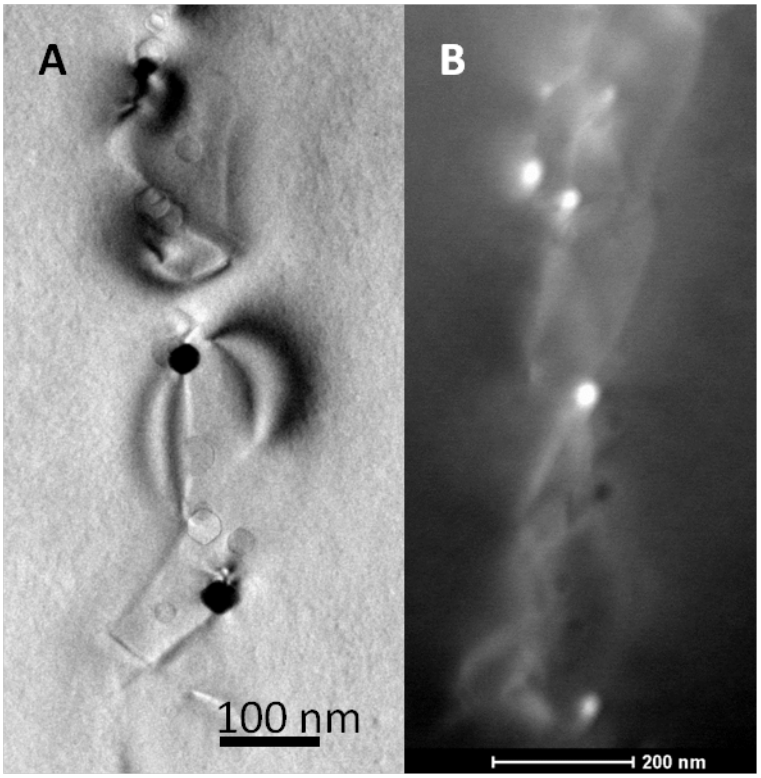

Figure 7.17: **A** Cross-sectional transmission electron micrograph and **B** scanning transmission electron micrograph of sample Au33.

7.3 Analysis of gold nanoparticles by high-resolution transmission electron microscopy, scanning transmission electron microscopy, and energy-dispersive X-ray spectroscopy

The nanoparticles in sample Au33 are examined in more detail by additional electron microscopy techniques to determine elemental composition and, if possible, crystallographic structure of nanoparticles and surrounding silicon host material. Comparison of TEM and scanning TEM in Figure 7.17 indicates that dark particles in bright-field TEM contain high-Z material, and that more high-Z material is dispersed throughout the void layer. Voids are clearly seen in STEM (Fig.7.17**B** as large holes with dark contrast. The source of hazy, dispersed secondary electrons is assumed to be Au atoms trapped at defects other than voids or nanoparticles, but the nature of these defects is not known.

Presence of Au is confirmed by energy-dispersive X-ray spectroscopy (EDS). Figure 7.18 contains **A** transmission electron micrograph with two red arrows showing the damage caused by line scans of the electron beam across two features collected in scanning mode: **B** a nanoparticle and **C** a void and dislocation. Scanning transmission electron micrographs, where the image is formed by highly scattered or secondary electrons collected by a high-angle annular dark field (HAADF) detector, are shown in **B** and **C**, and X-ray yield collected right-to-left from each position of the energy-dispersive X-ray spectroscopy (EDS) line scans indicated by red arrows are displayed in bottom panes. X-ray yields with characteristic energies of Si-K, Au-M and Au-L shells are plotted. The energies of the Au-M electron shells are 2.21-3.42 keV, for Au-L 11.2-14.4 keV, and for Si-K 1.84 keV [64, 33]. The transmission electron micrograph is obtained following scanning TEM and EDS collection, and the damage from focusing intense electron beam at each position indicates position and

breadth of each line scan.

The EDS line scan across the nanoparticle is straight-forward to interpet: Au atoms are trapped in void, and the large yield of Au-M and Au-L characteristic X-rays confirms this. Accompanying the presence of Au is depletion of Si-K characteristic X-rays, showing that Au replaces Si for a portion of the thickness of the TEM specimen. However, there is another effect that causes Si characteristic X-ray yield to be reduced even further. The electron beam penetrates the specimen ejecting electrons from the K-shell of Si atoms, and some fraction of the characteristic X-rays are emitted into the solid angle subtended by the HAADF detector. X-rays emitted from Si electron shells that have to penetrate Au nanoparticle have lower probability of being collected in HAADF detector than X-rays that do not have to penetrate Au, so the apparent Si atom concentration appears lower in the region with Au nanoparticle. The Au nanoparticle shields Si atoms lying beyond it from the electron beam, and shields the HAADF detector from some characteristic X-rays emitted from Si atoms.

The EDS line scan across the void in Figure 7.18 is challenging to interpret. There exist in this sample fully- and partially-filled nanoparticles, voids that may or may not have monolayer coverage of Au atoms on inner surfaces, and dislocation lines and loops. Gold atoms trapped in dislocations would cause sharp increase in Au-L or -M characteristic X-ray yield, and lack of such a signature indicates no highly localized Au trapping. Small increase in Au characteristic X-ray yield indicates the presence of Au atoms is related to the strain in the system due to irradiation induced defects and/or nanoparticles and voids. The barely measurable Au enrichment across a wide region indicates that the source measured Au atoms are not trapped in dislocations, but rather diffusion trapped in point defects or some other defects. One possible explanation is that Au atoms are diffusing into or out of Au nanoparticles because

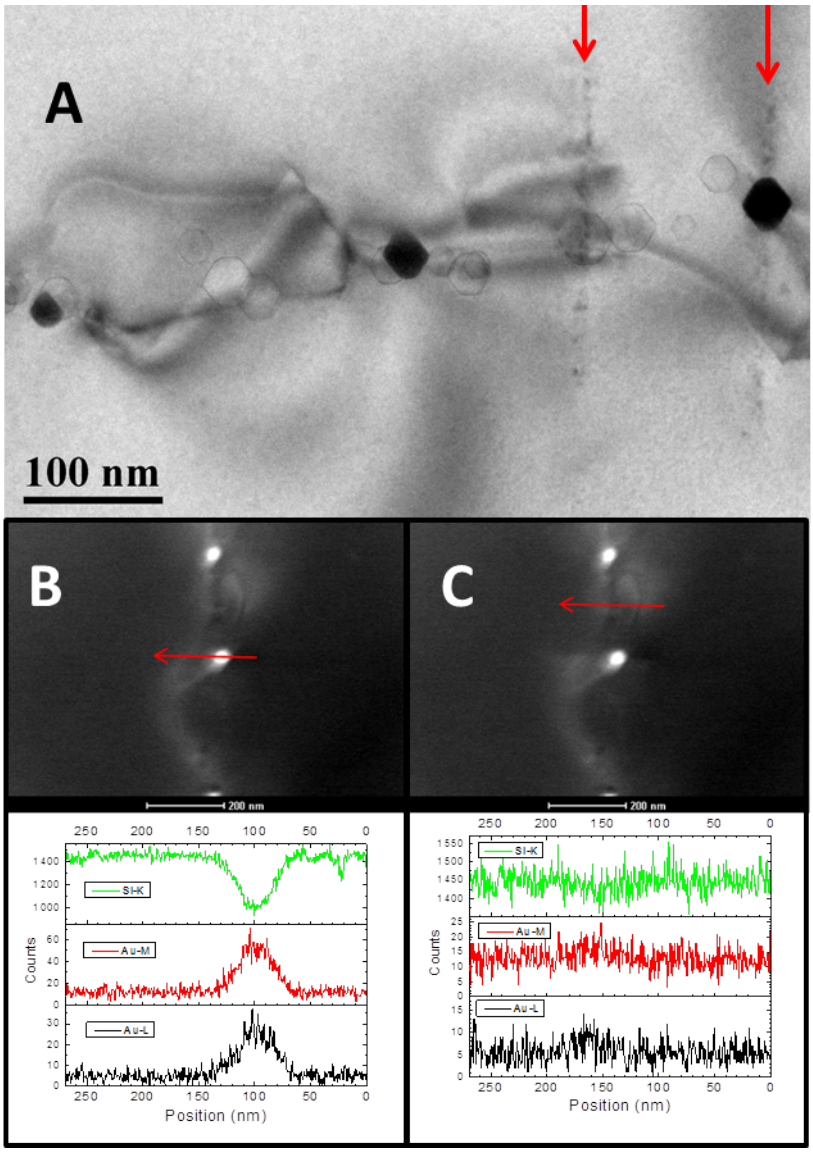

Figure 7.18: Sample Au33 **A** Cross-sectional TEM and **B** and **C** scanning TEM and energy dispersive X-ray yields of Si-K, Au-M and Au-L lines of **B** high-Z nanoparticle adjacent to dislocation and dilute high-Z area and **C** void adjacent to a dislocation in dilute high-Z area.

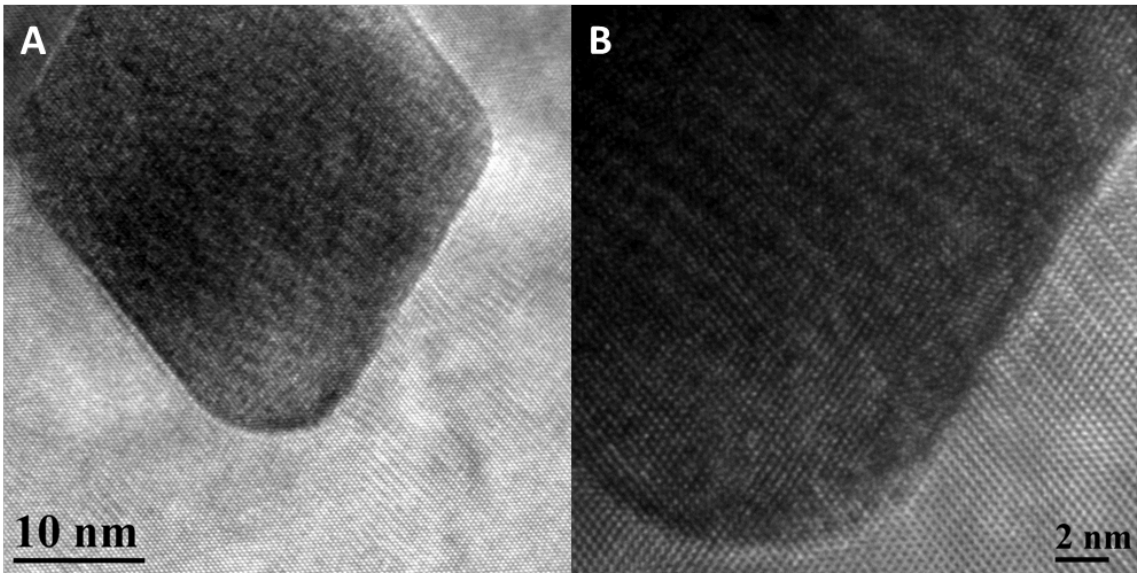

Figure 7.19: High-resolution cross-sectional transmission electron micrographs of nanoparticle in sample Au33 showing Au/Si interface.

the final processing parameter, annealing at 750 C for two hours, is not optimized to form Au nanoparticles.

High-resolution micrographs of one Au nanoparticle in sample Au33 are shown in Figure 7.19. Individual atomic planes of silicon are visible, and extend into the nanoparticle region. However, the atomic planes that extend without any deviation from silicon region into nanoparticle region are from pure silicon surrounding the nanoparticle. Unfortunately, no definitive crystallographic data determining the atomic structure of Au atoms in Au nanoparticles have been obtained. From Figure 7.19, we can see that there are no great distortions in silicon atomic planes near to the Au nanoparticle, and that it has a sharp interface. Furthermore, recognizing that the zone axes of these two micrographs are near to [011] the nanoparticle shape is bound by (111) and (100) planes.

7.4 Conclusions

In samples Au1-4, it is clear that Au readily diffuses into Si from a film on the surface. The diffusion is probably enhanced by defects created by He ion irradiation. Voids are created, but other point defects and extended defects clearly present a greater number of more stable trapping sites for Au atoms, so no Au trapping in void layer is observed.

Samples Au5-10 undergo heat treatment at temperatures ranging from 350-850°C without defect annealing. For the temperature range from 350-550°C, the simple case of increasing temperature causing increased diffusivity causes increased diffusion. However, as temperature increases from 550-650°C and so on, point defect recombination becomes progressively more important with increasing temperature, and diffusion decreases. Gold diffusion in silicon is mediated by silicon point defects, interstitials and vacancies, so annihilation of point defects at higher temperatures decreases Au diffusion.

Based on RBS results of comparing samples Au11-13 and Au14-16, changing the order of high temperature and low temperature heat treatments probably had a significant effect on the results, rendering the comparison of these sets of samples weak and uninformative.

Significant diffusion of Au is observed for samples Au1-16, but no trapping of Au in void layer is observed. Deposition of Au on surface in thick film introduces excessive amount of Au into Si, and trapping by open-volume defects is not observed following diffusion heat treatment.

Irradiation with small fluence of low energy Au ions controllably introduces Au into Si samples. Trapping of Au atoms in void layer is observed for samples Au17-32, but no nanoparticles are observed. Additional odd Au trapping behavior is also

noted, such as strong trapping at an intermediate peak in sample Au27. However, investigation by TEM shows that no nanoparticles are formed as a consequence of Au trapping observed by random RBS spectra for samples Au17-32. Decreasing He ion irradiation fluence by factor of five, to 1×10^{16} cm^{-2}, accompanied by maximum thermal budget for defect annealing accomplishes nanoparticle formation at projected range of He ion irradiation. However, further decreasing ion irradiation fluence by one order of magnitude did not accomplish nanoparticle formation.

Gold is contained in nanoparticles formed in sample Au33, evidenced by characteristic X-rays emitted by excitation with electron beam. Other locations of trapped Au could not be determined, but it is likely that dislocations do not contribute to significant amount of Au trapping. High-resolution TEM shows that Au nanoparticles have sharp interface with Si, and that Si surrounding nanoparticles is not strained. However, the atomic structure of Au nanoparticles has not been determined.

8. DECORATION OF VOIDS IN SILICON BY SILVER ATOMS

Irradiation species, fluence and defect annealing temperature are chosen so that low density of voids are nucleated free of helium and other chemical bonding that grow to sizes of few tens of nanometers accompanied by minimum amount of dislocations [28, 68, 59]. Silver atoms are diffused from the substrate surface and chemisorbed on the inner surface of voids in silicon. Nanoparticles are formed with size up to 40 nm. A range of fully filled nanoparticles, not accompanied by free volume, and partially filled nanoparticles, with widely vary free volume, are observed adjacent to each other.

8.1 Experimental methods

The method to fabricate nanoparticles by chemisorption onto an inner surface consists of three steps: create open volume defects in a suitable material, deposit immiscible metal on surface, and diffuse metal into defects. Voids are preferred open-volume defect in this research. For all samples deposited with Ag, ion irradiation fluence is 5×10^{15} cm^{-2}, except for Ag10-12 and Ag15-17, which are irradiated with 1 and 10×10^{15} cm^{-2} 100 keV He ions, respectively. Voids nucleate and grow by defect annealing at high temperature. Samples Ag1-8 and Ag18-27 are annealed in quartz tube furnace with flowing ultra-high-purity Ar gas at 950°C for 10, 30, 60 or 90 minutes. This furnace is in Prof. K. Ted Hartwig's research group located in the Doherty building on Texas A&M University campus. Details of samples Ag1-8 are found in Table 8.1 and Ag18-27 in Table 8.2. Samples Ag9-17 are annealed in different quartz tube furnace, designed to be ultra-high vacuum atmosphere, at 927°C for 1, 3.5 or 5 hours, and details of individual samples can be found in two tables.

Label	D.A. Time (min.)	Diff. H.T. Time (hr.)	Atmosphere
Ag1	10	1	UHP Ar
Ag2	10	2	UHP Ar
Ag3	30	1	UHP Ar
Ag4	30	2	UHP Ar
Ag5	60	1	UHP Ar
Ag6	60	2	UHP Ar
Ag7	90	1	UHP Ar
Ag8	90	2	UHP Ar
Ag9	210	2	Mixed

Table 8.1: Summary of defect annealing (D.A.) and diffusion heat treatment (Diff. H.T.) conditions. All samples are implanted with 5×10^{15} cm^{-2} 100 keV He ions before defect annealing, and 100 nm Ag deposited by evaporation on sample surface before diffusion heat treatment. For Ag1-6, approximately 110 nm of Ag is deposited before diffusion heat treatment. The indicated annealing atmosphere applies to both defect annealing and diffusion heat treatment. Defect annealing temperature is 950°C for samples Ag1-8, and 927°C for sample Ag9, and diffusion heat treatment temperature is 750°C for all samples in this table.

The Ag-Si eutectic temperature is 830°C, greater than diffusion heat treatment temperature [51]. Additionally, equilibrium concentration of Ag in Si is one to two orders of magnitude less than that of Au, so Ag metal is introduced by thin film deposition on surface of Si samples [60]. Evaporation of silver onto silicon surface is performed in BOC Edwards Auto 306 Metal Evaporation Chamber in the clean room of Materials Characterization Facility at Texas A&M. Before loading into metal deposition chamber, samples are sequentially dipped in baths of acetone for 15 seconds and isopropanol for 10 seconds then solvents evaporated by blowing dry N_2 gas. This process is repeated one additional time. Samples are mounted on glass slide and stored in desiccator for 15 minutes, then exposed to vapor emitted from open bottle of HF acid for approximately 10 seconds each to etch oxide layer. Then, samples on glass slide carried to clean room within five minutes of HF acid "vapor

etch". Following application of the (acetone-isopropanol-N_2)$_2$-HF procedure 100 nm Ag deposited on samples Ag7-8 and 110 nm on Ag1-6 on different dates. Samples deposited with Ag are stored in desiccator. All annealing heat treatments for Ag1-8 are performed within two days of metal deposition at 750°C for one or two hours in Dr. Hartwig's furnace with flowing UHP Ar gas. The temperature is measured by a thick thermocouple wire in the center of the furnace, and samples are contained in a quartz boat that can inserted into and withdrawn from the hot zone. All annealing heat treatment times are augmented by two minutes to allow for the samples and boat to heat up to furnace temperature. Approximately one minute is required to insert quartz boat into hot zone of furnace, and approximately three minutes are required to remove quartz boat from furnace hot zone. Approximately two minutes after removal from hot zone, samples and quartz boat cool to less than 100°C. Samples Ag1-8 are not removed from flowing Ar for at least two hours after removal from hot zone.

The thickness monitor in BOC Edwards Metal Evaporation Chamber is malfunctioning during this Ag film deposition. RBS measurement of samples after deposition determines approximately 500 nm of Ag film is deposited on these samples. Except for Ag film thickness, same procedures and same equipment, including furnace, is used for Ag18-27 and Ag1-8.

The same procedure is performed for samples Ag18-27 as for Ag1-8, with one notable exception. Deposition of Ag is performed in the same location with the same instrument following same surface preparation procedure, but the deposition rate meter is out of service and a different operator performed the deposition. This led to deposition of around 500 nm of Ag on the surface, measured by RBS. This amount of Ag could not be removed by cotton swab and solvent. An etchant was employed containing 1:1:1 H_2O:NH_4OH:H_2O_2. De-ionized water is used, and the concentration

of ammonium hydroxide and hydrogen peroxide are each 30%. Samples are placed into 30 mL total of etchant mixture for around 15 seconds followed by two rinses in DI-H_2O for five minutes each. Samples are then dried with dry N_2 gas, and rinsed in alternating acetone and methanol baths for five seconds through two iterations before drying again with N_2 gas. The etchant mixture is a portion of the "RCA clean", and reportedly carries the risk of depositing Fe on the surface of Si samples. Samples Ag19 and Ag21-23 are etched by this process first, and balance of samples in the Ag18-27 series are etched later.

Samples Ag9-17 are fabricated as described in Tables 8.1 and 8.2. The story defect annealing of samples Ag9, -11 and -16 will be shared in detail to illustrate difficulties encountered. These samples are loaded into home-made vacuum furnace, different from the one used for samples Ag1-8 and Ag18-27, on March 2, 2011, and vacuum is poor for a few days following. On March 8, 2011, vacuum reads 7×10^{-8} torr and furnace set to 930°C. The target temperature is 927°C because the furnace could not heat up to desired 950°C. The samples are annealed for 3.5 hours plus two minutes, with actual furnace temperature, measured by thermocouple outside quartz tube near heating elements, ranging from $916 - 937$°C and pressure ranging from $6.5 - 9.5 \times 10^{-7}$ torr. Following defect annealing, irradiated surfaces appear clean, but on some samples the back surfaces possessed a rainbow-like discoloration.

Samples Ag9-17 are then deposited with 100 nm Ag by physical vapor deposition following surface preparation procedure described above in Edwards deposition chamber at Materials Characterization Facility at Texas A&M. Before diffusion heat treatment is performed on May 12, 2011, a steadily worsening vacuum leak effecting the home-made vacuum furnace is detected, and furnace is modified slightly into a flowing Ar gas furnace. Diffusion heat treatment is performed with ultra-high purity Ar gas for two hours plus two minutes at 750°C.

Label	Fluence (cm^{-2})	D.A. Time (hr)	D.H.T. Time (hr)	D.H.T. Temp. (°C)
Ag10	1×10^{15}	1	2	750
Ag11	1×10^{15}	3.5	2	750
Ag12	1×10^{15}	5	2	750
Ag13	5×10^{15}	1	2	750
Ag14	5×10^{15}	5	2	750
Ag15	1×10^{16}	1	2	750
Ag16	1×10^{16}	3.5	2	750
Ag17	1×10^{16}	5	2	750
Ag18	5×10^{15}	0.5	0.17	750
Ag19	5×10^{15}	0.5	0.5	750
Ag20	5×10^{15}	0.5	0.17	650
Ag21	5×10^{15}	0.5	0.5	650
Ag22	5×10^{15}	0.5	1	650
Ag23	5×10^{15}	0.5	2	650
Ag24	5×10^{15}	0.5	0.17	550
Ag25	5×10^{15}	0.5	0.5	550
Ag26	5×10^{15}	0.5	1	550
Ag27	5×10^{15}	0.5	2	550

Table 8.2: Ion fluence, defect annealing (D.A.) and diffusion heat treatment (D.H.T.) parameters. All samples are implanted with 100 keV He ions before defect annealing to indicated fluence. After defect annealing, 100 nm Ag deposited by evaporation on substrate surface. Leaks in vacuum furnace during defect annealing at 927°C are suspected to have seriously altered results of samples Ag10-17. Diffusion heat treatment carried out in flowing UHP Ar gas for diffusion heat treatment of Ag10-17. Samples Ag18-27 were annealed and heat treated in flowing UHP Ar gas.

The precise role of contamination from leaking vacuum furnace during defect annealing is not known, but it certainly effected every sample in the Ag9-17 series. For this reason, we believe that fabrication of sample Ag9 can not be repeated.

Cross-sectional TEM specimens of several of Ag9-17 series are fabricated by the author and Alvaro Aranibar, an undergraduate student worker.

Samples are analyzed by TEM and RBS. Cross-sectional TEM specimens from several of Ag9-17 samples are fabricated by mechanical thinning and dimpling so that the thinnest portion is less than 5 microns thick. Then specimens are ion milled with few-keV Ar ions at glancing angle to achieve thickness required for electron transparency, less than 200 nm. JEOL JEM-2010 electron microscope operating at 200 kV and FEI Tecnai G2 F20 ST FE-TEM operated at 200 kV at the Microscopy and Imaging Center at Texas A&M.

Cross-sectional TEM specimens for samples Ag1-8 are fabricated and analyzed by Dr. N. David Theodore at Freescale Semiconductor, Inc. in Chandler, AZ. Specimens are fabricated by the lift-out method using dual-beam scanning electron microscope-focused ion beam using liquid metal Ga source and analyzed using electron microscope operating at 200 kV.

Sample surfaces are prepared for RBS by wiping off excess Ag film remaining on surface. For samples with around 100 nm Ag deposition, wiping with cotton swabs wetted with a solvent such as isopropanol is sufficient to remove Ag. RBS is performed with analyzing beam of 2 MeV He ions, and current is 10 nA or less. Analysis of samples Ag1-8 is performed at Dr. Wei-Kan Chu's ion accelerator lab at University of Houston. Analysis of samples Ag18-27 by 2 MeV He ion beam in random mode is performed on 1.7 MV tandem accelerator at Texas A&M University Ion Beam Lab. In both cases, surface barrier detector is placed at 165° backscattering angle in IBM geometry. No RBS analysis is performed on samples Ag10-17.

Samples Ag1-8 are analyzed by RBS and areal density of trapped Ag atoms with background subtracted are extracted by RBS simulation code RUMP. Areal density is converted to thickness of a continuous film of Ag by assuming the density of Ag to that of bulk Ag. According to results shown in chapter 9, this is a reasonable assumption.

8.2 Results

Samples Ag1-8 are simultaneous investigation of defect annealing and diffusion heat treatment conditions. Transmission electron micrographs of samples Ag1-8 are contained in Figures 8.1 and 8.2 which have varying defect annealing times and diffusion heat treatment times of one and two hours, respectively. Individual nanoparticles from each are expanded in insets, and scale bars in all insets represent 20 nm.

In Fig. 8.1, features are located at depth near the calculated end-of-range of 100 keV He ions [76]. More Ag is trapped in each nanoparticle in Fig. 8.1**A** and **C** than in **B**, but nanoparticles in **B** appear more numerous than in **A**. Varying amounts of dislocations are observed which roughly correspond with defect annealing time. Figure 8.1**A** contains a number of dislocations in band containing nanoparticles, in **B** fewer, smaller dislocations and dislocation loops are visible, and in **C** a few long dislocation lines are visible.

Nanoparticles in each inset of Fig. 8.1 show that presence of Ag causes change in faceting from equilibrium shape of void in Si to something else [14]. Examination of the partially filled void/nanoparticle complexes reveals that the void sizes vary more than nanoparticle sizes, suggesting that Ag trapping is more heavily dependent on diffusion heat treatment thermal budget than on the initial void size. Partially filled voids result from initial void size distribution and diffusion heat treatment parameters that are not optimized. In 8.1**D**, small nanoparticles, 5 nm diameter

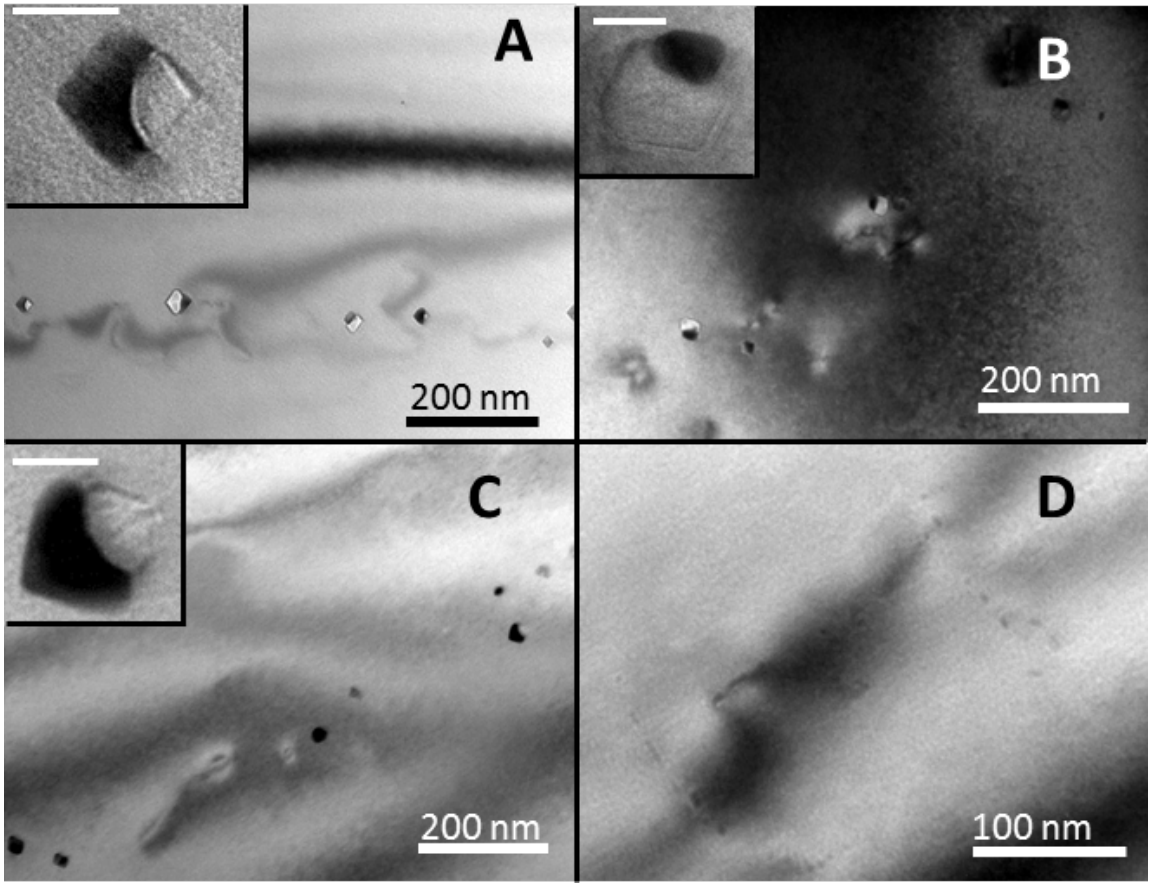

Figure 8.1: Cross-sectional transmission electron micrographs of samples **A** Ag1, **B** Ag3, **C** Ag5 and **D** Ag7. The diffusion heat treatment condition of all is 750°C for one hour, but time of 950°C defect annealing is **A** 10, **B** 30, **C** 60 and **D** 90 minutes. Insets in **A**, **B**, and **C** highlight individual nanoparticles representative of the entire sample, and each scale bar represents 20 nm.

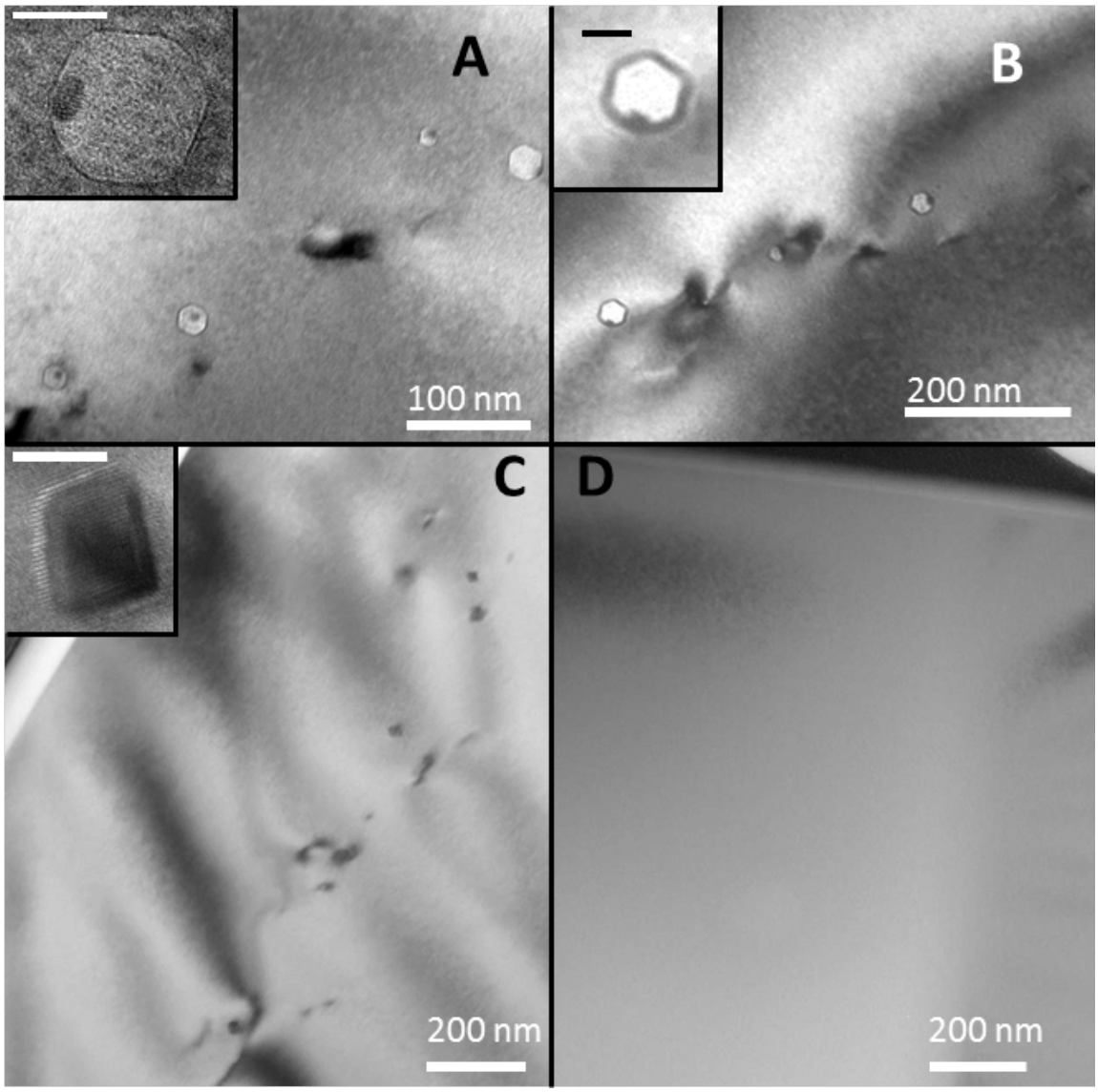

Figure 8.2: Cross-sectional transmission electron micrographs of samples **A** Ag2, **B** Ag4, **C** Ag6 and **D** Ag8. The diffusion heat treatment condition of all is 750°C for two hours, but time of 950°C defect annealing is **A** 10, **B** 30, **C** 60 and **D** 90 minutes. Insets in **A**, **B**, and **C** highlight individual nanoparticles representative of the entire sample, and each scale bar represents 20 nm.

or less, are clustered around something that appears to be a dislocation because of the dark, strain-induced contrast. It is not clear if larger nanoparticles formed and then dissolved or if small quantity of Ag atoms are transported by diffusion from the surface and decorate available, small open volume defects.

The features visible in Figure 8.2 are at depth around 650 nm, close to the calculated end-of-range of 100 keV He ions calculated by SRIM binary collision approximation code [76]. Comparison of the defects in the void/nanoparticle band in **A**, **B** and **C** exhibit the opposite of the expected trend, where dislocations are visible in **B** and **C** but none in **A**. Small differences exist between Fig. 8.2**A** and **B**, with partially filled void-nanoparticles approximately 30 and 40 nm in diameter and small amount of silver trapped in each, but slightly more in **B** than in **A**. Shape of void/nanoparticles in **A** and **B** insets are much different than nanoparticle in **C** inset. Condition Ag8, shown in Fig. 8.2**D**, shows no features visible in TEM. The surface is visible at the top, and the field shows beyond the 650 nm depth at which voids, nanoparticles and dislocations should be located.

Faceting of nanoparticles shown in insets of Figs. 8.1 and 8.2**A** and **B** are markedly different. The amount of trapped Ag also differs significantly, so the faceting must result from presence of Ag in the void. Bonding of Ag to Si must be anisotropic, meaning bonding of Ag on some Si crystallographic planes is energetically favorable over others. In this case, faceting results in lowering the system free energy, as it does for faceting of voids in pure materials. Evidence for this can be seen in the profound difference in nanoparticle morphology in Fig. 8.2**C** compared to **A** and **B**. However, comparison of nanoparticles in Figs. 8.1 and 8.2**C** confuses this story a little, and results using more refined experimental techniques are shown in a later chapter.

The amount of silver atoms trapped in the void region of samples Ag1-8 are

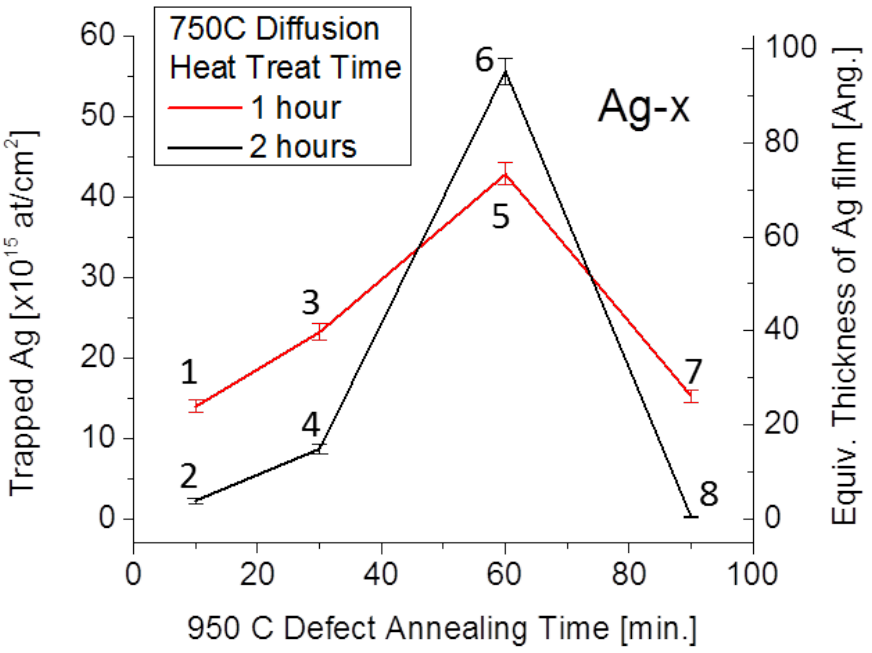

Figure 8.3: Quantity of silver atoms trapped in void region measured by RBS. Numbers at each data point indicate which "Ag-x" sample corresponds to that point, according to Table 8.1.

measured by RBS and compared according to the defect annealing and diffusion heat treatment times in Figure 8.3. The number next to each point shows which condition corresponds to that point, e.g. "1" is Ag1, and sample description is contained in Table 8.1. The left ordinate axis shows the amount of trapped Ag in units of areal density, *atoms* cm^{-2}, the quantity measured by RBS analysis. The right ordinate is areal density converted into the equivalent thickness of silver film with bulk volumetric density, 10.49 $g\ cm^{-3}$, in angstroms. The right ordinate shows significant mass transport occurs in the diffusion heat treatment, more than 9 nm in Ag6. The trend observed in Fig. 8.3 defies easy explanation. It is clear that defect annealing and diffusion heat treatment parameters must be optimized. For defect annealing times of 10, 30 and 90 minutes at 950°C, increased diffusion heat treatment time at 750°C decreases the amount of trapped Ag atoms. Trapping in these cases must be metastable. When defect annealing is 60 minutes at 950°C, trapping of Ag atoms increases when diffusion heat treatment time increases, suggesting trapping in this case is more stable than in defects created by different annealing times.

The trapping of Ag in voids is metastable, which has been shown for void gettering of Au [46]. The defect annealing time has greater effect on the amount of trapped Ag than on the size of individual nanoparticles. Increasing the amount of trapped Ag in each nanoparticle causes the shape of the void containing the nanoparticle to change. The morphology of nanoparticles is effected by amount of Ag trapped and density of voids available for trapping. The amount of Si point defects remaining after defect annealing determine the diffusion of Ag through the fixed distance from surface to voids, possibly by the dissociative mechanism of defect-mediated diffusion discussed for Ag in Si [60]. Comparison of the relative disorder of Si atoms, shown in Chapter 9, with the Ag trapped by one hour diffusion heat treatment in Fig. 8.3 shows Si point defects are not proportional to amount of trapped Ag.

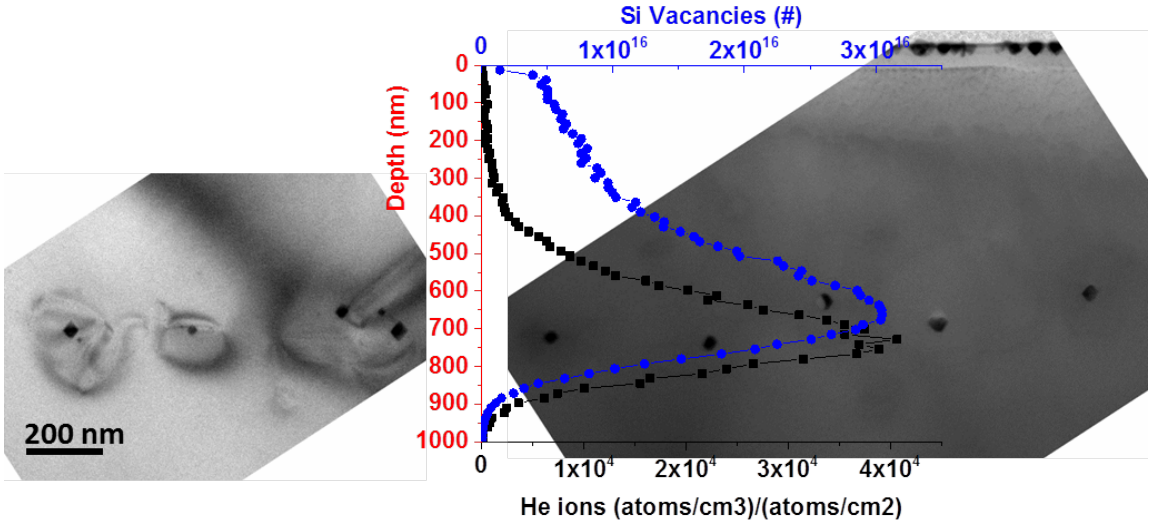

Figure 8.4: Overviews of sample Ag9 aligned with SRIM calculation showing the range of He ions and Si vacancy profile.

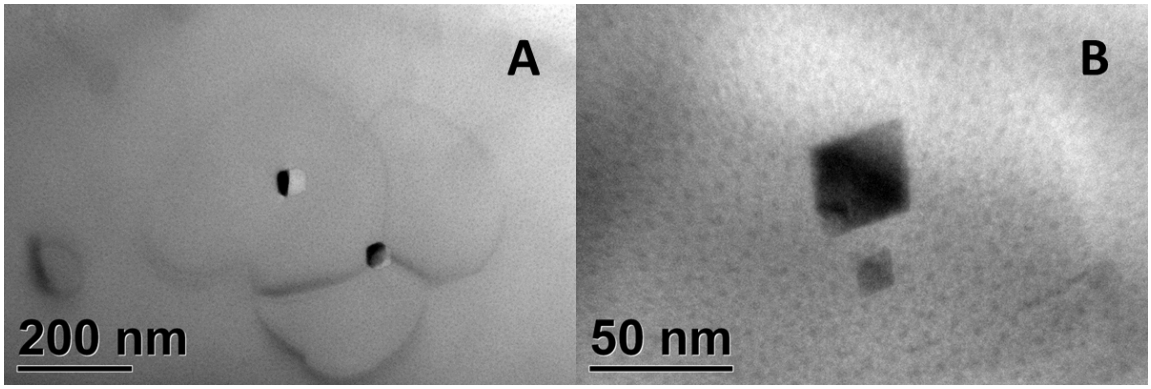

Figure 8.5: Transmission electron micrographs from sample Ag9 showing **A** partially filled and **B** fully filled nanoparticles. All nanoparticles shown are faceted, but fully filled nanoparticles are more strongly faceted.

Figure 8.4 shows nanoparticles from two regions formed at the end of range of 100 keV He ions [76]. The He ion and Si vacancy profiles are extracted from SRIM binary collision approximation simulations and overlaid. In the micrograph on the right, the surface is visible and aligned with plot, and plot length scale applies. In the micrograph on the left, a scale bar is included. Nanoparticles with diameters up to 40 nm are shown. Some voids are partially filled with Ag and some are fully filled. Other sources of dark contrast, seen especially in left micrograph, are extended interstitial-type defects such as dislocations.

Figure 8.5 shows higher magnification of nanoparticles from two regions of sample Ag9. In **A** there are partially filled nanoparticles, and in **B** there are large and small fully filled, highly faceted nanoparticles. There are three lines surrounding the two nanoparticles in **A** that are not explainable yet. They are too small to be thickness differences in the sample, and appear too large to be stress fields.

A micrograph from sample Ag14 is shown in Figure 8.6. This micrograph is in-focus, but voids can still be clearly seen. The thermal budget for defect annealing is very high, five hours at 927°C, explaining the relative dearth of features. It is possible that this sample does contain Ag nanoparticles, but the concentration of trapped Ag is too low to merit significant interest. With questionable repeatability due to defect annealing atmosphere, this sample is not investigated further. However, this micrograph is instructive, showing that excessive defect annealing leaves few features at the end of range of He ion irradiation which are able to trap diffused Ag atoms.

An overview micrograph of sample Ag16 is shown in Figure 8.7 with a damaged and defected surface. It must be assumed that the surface defects were introduced by contamination due to leak in vacuum furnace during three-and-a-half hour defect annealing. Despite the surface irregularities, a surprising amount of nanoparticles are formed. The surface deterioration makes accurate determination of the depth

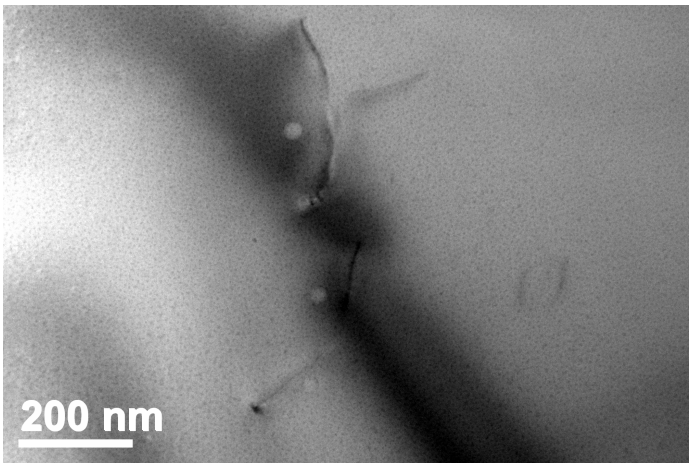

Figure 8.6: Cross-sectional transmission electron micrograph of sample Ag14.

of these nanoparticles impossible, but it is safe to assume that nanoparticles are formed at depth around 650 nm from surface, the projected range of 100 keV He ions. Careful study of the nanoparticles in Figure 8.8 indicates that nanoparticles appear the same as others formed in more "successful" cases, as in Figs. 8.4-8.5. It is doubtful that this sample, or any other from the sequence Ag9-17, could be repeated using the same experimental conditions, but the nanoparticles do exist for study.

The same irradiation condition, 1×10^{16} cm^{-2} 100 keV He ions, annealed for longer time, sample Ag17 is shown in Figure 8.9. This sample shows voids partially filled with nanoparticles with size along greatest dimension around 15-20 nm, and voids containing nanoparticles are strongly faceted. The faceting of the voids is similar to those seen in samples Ag1 and -5, shown in Fig. 8.1, and different from the equilibrium shape of voids in pure Si [14]. Furthermore, voids that would ordinarily require application of the under-focus over-focus method to enhance Fresnel contrast to detect are plainly visible in Figure 8.9**A**.

As with sample Ag16 shown in Fig. 8.7, sample Ag17 suffers from surface irregularities. Dramatic evidence of type of surface defect commonly observed for

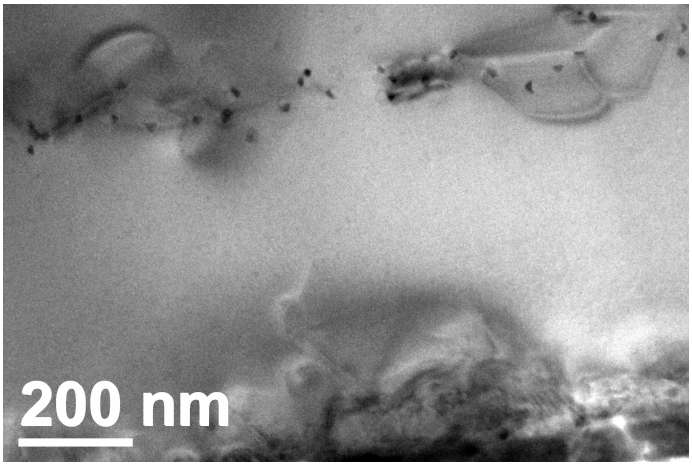

Figure 8.7: Cross-sectional transmission electron micrograph of sample Ag16 showing contaminated surface at bottom.

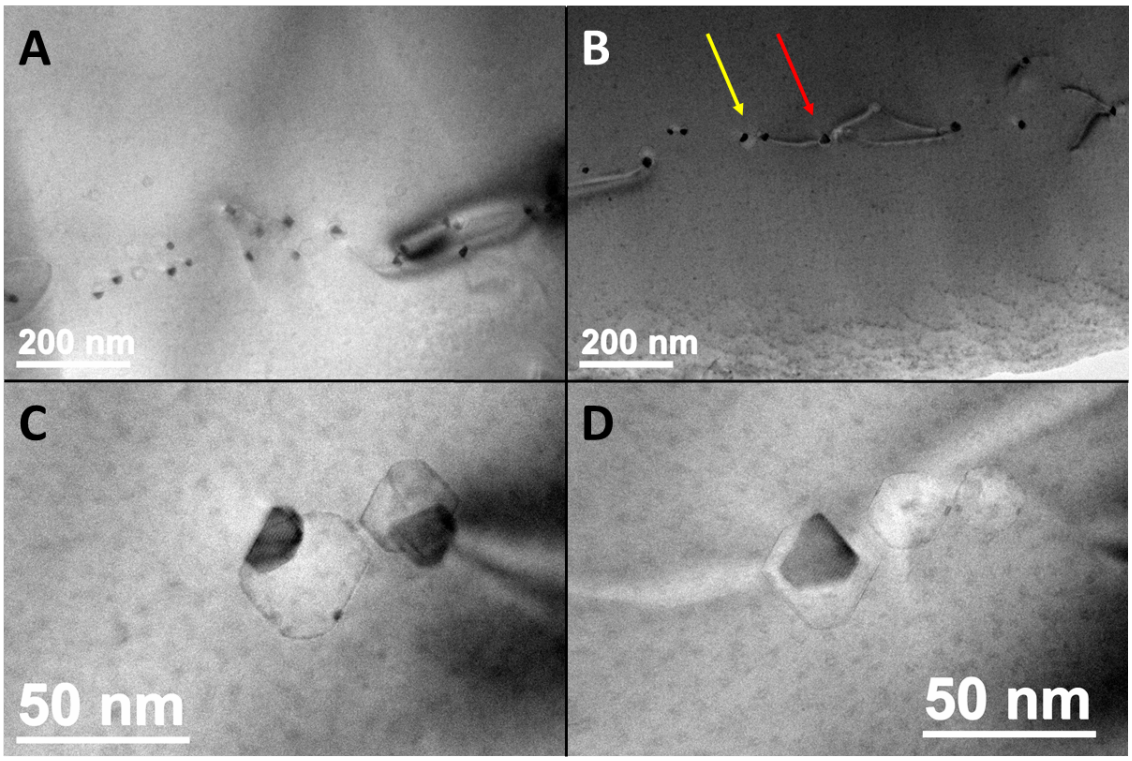

Figure 8.8: Cross-sectional transmission electron micrographs of sample Ag16 showing nanoparticles. **C** and **D** are higher resolution micrographs of nanoparticles indicated by yellow and red arrows, respectively, in **B**.

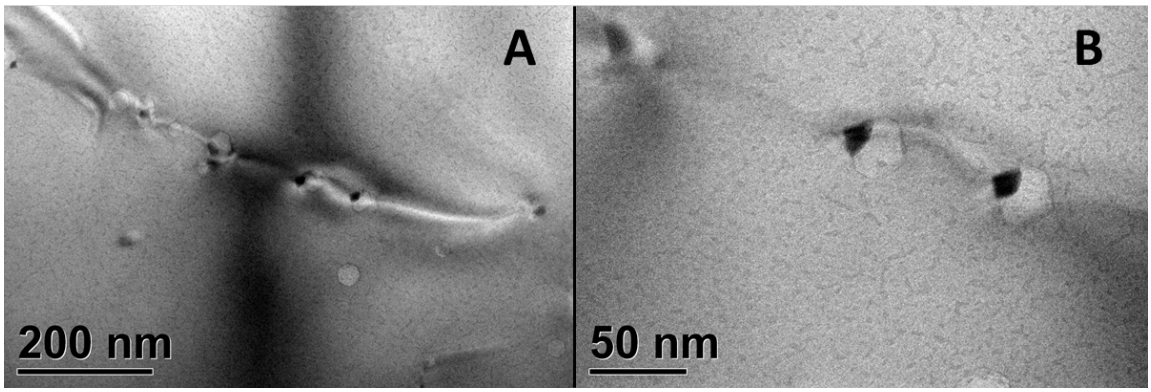

Figure 8.9: Cross-sectional transmission electron micrographs of sample Ag17 showing nanoparticles. **B** is higher resolution micrograph of nanoparticles in center of **A**.

this sample is shown in Figure 8.10. The pitting observed extends several hundred nanometers below the surface. The shape of the pits is almost hemispherical, which can help to eliminate some possible causes. For example, excessive exposure to HF acid would create pits with (111) plane faces. The hemispherical shape could be caused by oxidation of that volume initiated at a small surface defect, which was then promoted by contaminated vacuum during defect annealing, and which was etched away by surface cleaning treatment involving HF acid. Ag16 and -17 suffer from greatest surface irregularities, and they underwent defect annealing together in the last set in the vacuum furnace with a steadily worsening leak.

The final micrograph from the "unsuccessful" series Ag10-17 due to surface contamination comes from sample Ag10, shown in Figure 8.11. No features are shown in the region of interest between the surface and the calculated end-of-range of 100 keV He ions. The implanted ion fluence is too low for voids to nucleate or the defect annealing thermal budget is too large for voids to evolve large enough to be observed by TEM.

Samples Ag18-27 are investigated by RBS to determine amount of Ag atoms

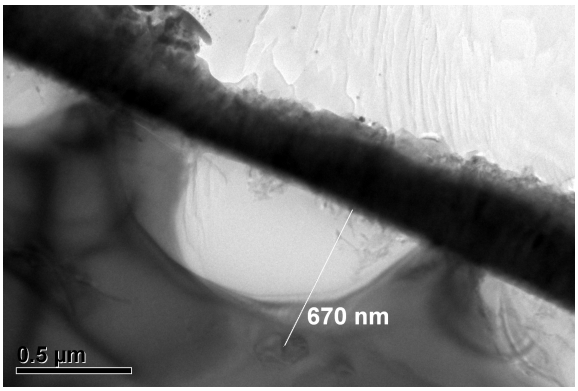

Figure 8.10: Cross-sectional transmission electron micrograph of sample Ag17 showing depth of voids and dislocations created by experimental method listed and large pit with depth several hundred nanometers.

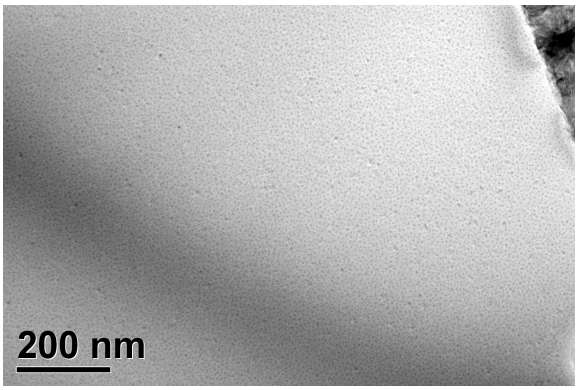

Figure 8.11: Cross-sectional transmission electron micrograph of sample Ag10 showing no voids, dislocations or nanoparticles. The small dots are believed to be created by ion milling with Ar ions to sufficiently thin the sample for TEM.

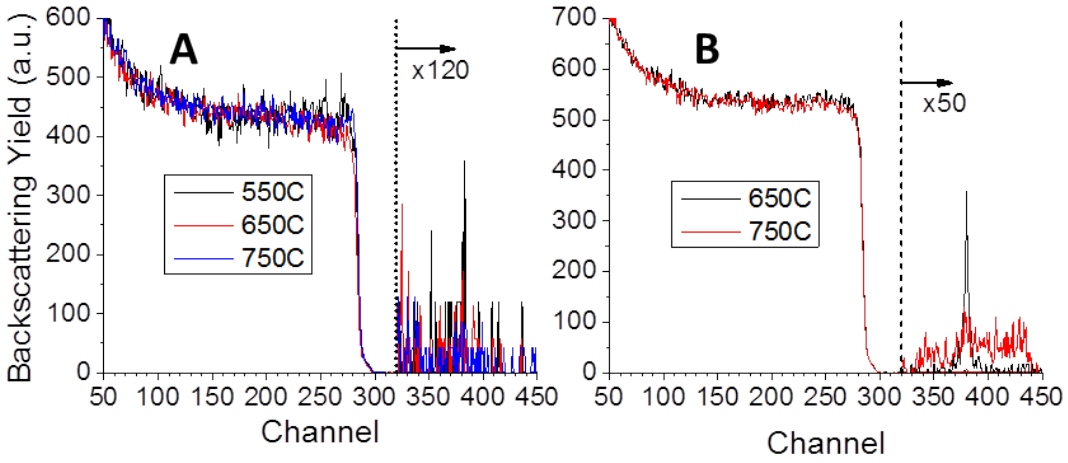

Figure 8.12: Rutherford backscattering energy spectra from **A** samples Ag18, -20 and -24 subjected to diffusion heat treatment for 10 minutes at 750, 650 and 550°C, respectively, and **B** samples Ag19 and -21 subjected to diffusion heat treatment for 30 minutes at 750 and 650°C, respectively. The sharp peak shown in spectra from sample Ag21 is caused by thin layer of Fe contamination on surface of sample due to chemical etching of Ag surface layer.

trapped in void region, shown in Figure 8.12. No trapped Ag is observed except in sample Ag19, the sample with largest diffusion heat treatment thermal budget. Silver is diffused from a surface layer, $\approx$ 500 nm thick, for 30 minutes at 750°C in sample Ag19. The overly thick Ag surface layer is caused by poor operation of a malfunctioning deposition chamber, and it required chemical etching to remove. A consequence of chemical etching was deposition of thin layer of Fe contamination, seen in the sharp peak at channel 382 in spectrum from sample Ag21. The energy of that channel corresponds exactly to backscattering from Fe on surface, and if Ag were trapped in that sample, it would not be confined to such a thin layer with no evidence of trapping anywhere else. Samples Ag22 and -23 (not shown), with diffusion heat treatments at 650°C for one and two hours, respectively, are similar to sample Ag21 in that there is no Ag trapping in voids.

8.3 Conclusions

Silver atoms diffuse into Si mediated by Si point defects, and are chemisorbed at inner surfaces of voids. The morphology of voids changes based on amount of Ag atoms trapped in voids.

The defect annealing and diffusion heat treatment parameters, time, temperature and atmosphere, have strong effect on Ag trapping at voids. Defect annealing creates two conditions that effect Ag trapping in voids: first, the void size, which increases with increasing time or temperature, and shape, which is spherical or faceted; second, the concentrations of point defects which mediate diffusion of Ag from surface to voids. The diffusivity of Ag atoms in Si samples containing some concentration of point defects throughout and voids localized far from surface depends on diffusion heat treatment time and temperature as well as point defect concentrations. However, temperature of diffusion heat treatment is sufficient to anneal defects that are not stable, including point defects, so diffusivity is also dependent on diffusion heat treatment time. It is observed that void size does not change dramatically with increased diffusion heat treatment time, so we consider He-induced voids at depth 650 nm in Si stable defects at 750°C.

High density of nanoparticles are formed as well as large nanoparticles, but the parameters used to fabricate samples Ag9-17 are not repeatable due to contaminated atmosphere during defect annealing. However, these questionable samples prove it is possible.

The study of Ag trapping by RBS of samples Ag18-27 leads to a couple of important conclusions about what will not work or cause additional difficulties in Ag nanoparticle fabrication process in Si. First, diffusion heat treatment times of 30 minutes or less and temperatures of 650°C or less cause no Ag to be trapped in void

layer. Increasing temperature to 750°C for time of 30 minutes causes some Ag to be diffused to and trapped in voids, but very small amount. Secondly, etching a thick layer of Ag can lead to other, unexpected contamination on the surface. In this case, Fe is deposited on surface, and the ready diffusion and compound formation of Fe in Si is problematic for electronic devices. This etching should be avoided by only applying Ag films on the surface thin enough to remove by common solvents.

9. CHARACTERIZING THE ATOMIC STRUCTURE OF SILVER NANOPARTICLES IN SILICON

This chapter studies silver nanoparticles in samples Ag3 and Ag9, described in Table 8.1 on page 76. Heteroepitaxial growth of Ag on Si111 and Si110 utilizes 4:3 coincident-site lattice (CSL), and on Si100 2:3 CSL. The co-incident site lattice depends on the configuration of the void, specifically the family or families of atomic planes that define the void shape are inner surfaces. The implicit assumption in the exercise of defining CSL's is that inner surfaces of voids do not restructure.

Metal nanoparticles are grown inside silicon voids with atomic planes of Ag and Si parallel, measured by electron microscopy and diffractometry. Channeling RBS analysis measures the amount of residual disorder in material surrounding nanoparticles, and angular scans confirm alignment of multiple Si and Ag channeling axes.

9.1 Experimental methods

The two samples investigated in this chapter are irradiated with 100 keV He ions to fluence 5E15/cm2 100 keV He ions at room temperature with a well-focused, rastered beam into same p-type (100)-oriented Si wafer grown by float-zone technique. Defect annealing to nucleate and grow voids in sample Ag3 is performed for 30 minutes at 950°C in flowing ultra-high purity Ar in a quartz tube furnace utilizing a hot-zone method. Defect annealing of sample Ag9 is performed for 210 minutes at 927°C in vacuum in a quartz tube furnace utilizing a hot-zone method. The sample rests in a quartz boat and is inserted into and withdrawn from the furnace at temperature as rapidly as possible. Reported annealing times do not include fixed two minutes added to allow the sample to heat up to hot-zone temperature. After defect annealing and before physical vapor deposition (PVD), sample surfaces are

cleaned by sequential acetone and ethanol baths followed by evaporation with dry N2 gas, performed twice, then etching with HF acid vapor for 10 s. Evaporation of 100 nm Ag onto Si surface is performed in BOC Edwards Auto 306 Metal Evaporation Chamber in the Materials Characterization Facility at Texas A&M. Heat treatment to diffuse Ag into Si is performed at 750 C for one hour (Ag1, -3, -5 and -7) or two hours (Ag6 and -9) in quartz tube furnace with flowing ultra-high purity Ar utilizing same hot-zone method. Samples Ag1, -3, -5, -6, -7, and -9 are analyzed by different methods in this chapter. Additional details not listed here of the ion irradiation, defect annealing, Ag film deposition and diffusion heat treatment parameters that each sample is subjected to are listed in Table 8.1 on page 76 in chapter 8.

All samples listed above are examined by transmission electron microscopy, but in this chapter samples Ag3 and Ag9 are examined more closely than the results shown in chapter 8. Cross-sectional specimens for transmission electron microscopy are created by mechanically polishing and dimpling followed by Ar ion milling at shallow angle in the case of Ag9, or by dual-beam SEM/FIB at Freescale, Inc. in the case of Ag3. TEM specimens from Ag9 are characterized in JEOL JEM-2010 microscope operated at 200 kV at the Texas A&M Microscopy and Imaging Center, and Ag3 specimen in at Freescale, Inc. The spacing of Ag atomic planes measured by diffraction patterns obtained are normalized to Si atomic planes.

Portions of micrographs are filtered by process of fast Fourier transformation, masking, and inverting the transformation. These transformed images are then averaged with original micrograph to yield Fourier-filtered micrographs which emphasize a feature that is weak due to noise. This is performed in Digital Micrograph software from Gatan, Inc.

Ion backscattering measurements were performed at Texas Center for Superconductivity at University of Houston. A 2 MeV He ion analyzing beam probes the $\langle 100 \rangle$

	a ($\times 10^{-3}$)	b	c ($\times 100$)	d ($\times 10^{4}$)
Ag1	-1.6571940476906	1.0036617692766	-2.0057048250340	3.0321860590388
Ag3	-1.0130434903008	0.55229231822304	-1.0203886839419	1.5079594626911
Ag5	-1.1481679748530	0.60594918248434	-1.0892069580227	1.5074684333392
Ag6	-1.4926311321181	0.76976354146469	-1.3509693790977	1.6974488155311
Ag7	-1.6313516098711	0.79382548456974	-1.3025228785271	1.6369719973077
Si	-2.2667254034740	1.0969971791027	-1.8355976432599	2.0460487198490

Table 9.1: Coefficients for third-order polynomial of type $f(x) = ax^3 + bx^2 + cx + d$ fitted to RBS random spectra obtained from samples in channel interval 50-200, where x is channel number and $f(x)$ is counts.

and $\langle 110 \rangle$ axial channels, and the beam is aligned with the (100) plane channel as it scanned across the $\langle 110 \rangle$ axial channel. During angular scans of the $\langle 100 \rangle$ axis, the beam is not aligned with a plane channel. A surface barrier detector collects He ions backscattered 165° from incident direction. RBS spectra obtained under random orientation are fitted with third-order polynomials using the Microsoft Excel program in the channel range 50-200, and these fitted polynomials are used instead of raw data of random spectra to extract relative disorder profiles. Values for R^2 variance for fitted functions are 0.971, 0.966, 0.970, 0.970 and 0.963 for random spectra from samples Ag1, -3, -5, -6 and -7, respectively, and is 0.987 for random spectrum from pure Si. Values of the coefficients and variance are listed in Table 9.1. The purpose of this additional fitting is to compare channeling spectra to random spectra that are close to ideal random spectra, discussed in chapter 6.

9.2 High-resolution cross-sectional transmission electron microscopy and diffractometry indicating alignment of atomic planes

Transmission electron micrograph in Figs. 8.4 and 8.5 on pages 87 and 87 show voids evolved by defect annealing for 3.5 hrs and Ag nanoparticles grown by diffusion heat treatment at 750°C for two hours, with additional details described in section

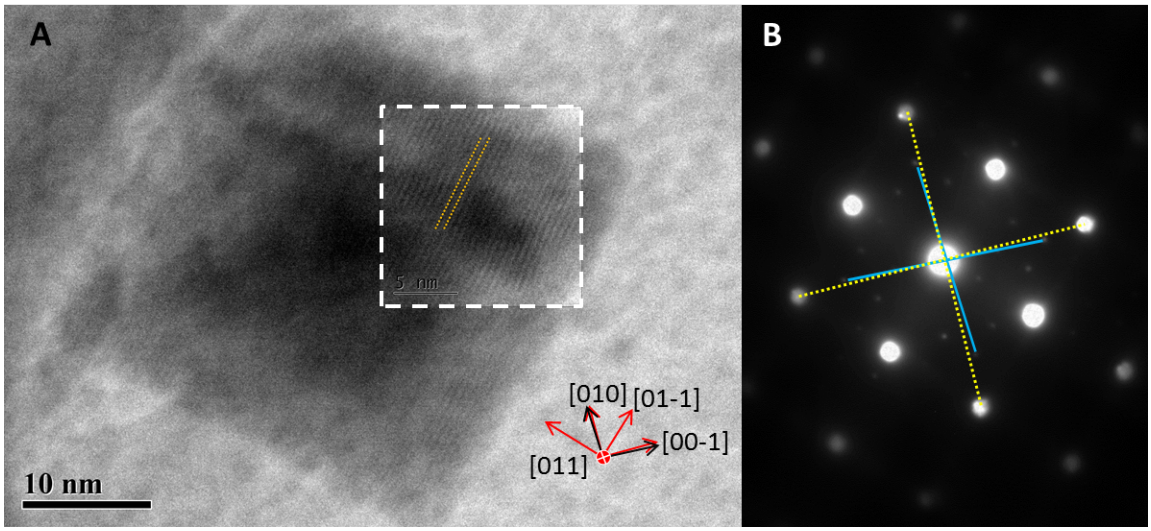

Figure 9.1: **A** Transmission electron micrograph and **B** electron diffraction pattern of nanoparticle in sample Ag9. Zone axis of the electron beam is [100].

8.1 of chapter 8. Nanoparticles have diameters up to 40 nm, and are found in a band more than 100 nm thick.

High-resolution transmission electron micrograph and diffraction pattern of a large nanoparticle found in Ag9 cross-sectional TEM specimen are shown in Figure 9.1. The arrows indicating low-index orientations in **A** are derived from diffraction pattern **B**, where red indicates Si and black indicates Ag atomic plane directions. According to the diffraction pattern, Si and Ag (110) planes analyzed are parallel to each other, but Si and Ag (100) planes are deviated by around 3°. This angular deviation indicates that the crystal structure of Ag in nanoparticle is no longer cubic, but the right angles measured between Ag (110) atomic planes from the same electron diffraction pattern counter such a conclusion. In a cubic crystal, the (001) and (010) atomic planes have a square projection when viewed along the (100) direction, and the (011) and (01-1) planes are diagonals within that square. The angular deviation in (010) and (001) planes in diffraction pattern do not show that the Ag crystal

is rotated with respect to the Si crystal, but that the projection of the (010) and (001) planes is changing from a square to a parallelogram. The Ag (001) plane spacing measured in Fig. 9.1**B** is within 0.3% of tabulated value, but Ag (010) and both Ag (011) planes deviate from tabulated values by 3.5%. It has been reported that the lattice structure of silver in nanowires at room temperature can compress in one direction to become face-centered tetragonal crystal [66]. However, such a transformation from cubic to tetragonal crystal structure would be accompanied by changes in the spacing of one of the (100) planes, which is observed in this case, but no change in the angle between planes, which is not observed in this case.

The projection of the nanoparticle in Fig. 9.1 viewed along the [100] zone axis is square, with shape bounded by (110) planes. A portion of the micrograph outlined by white square has been filtered to enhance the apparent fringe spacingby Fourier filtering method described in section 9.1 of this chapter. The fringe spacing measured from the filtered portion of the micrograph **A** is 5.6 Å, and the fringes are parallel to the [01-1] direction in Ag and Si.

The same nanoparticle is shown in electron micrograph and diffraction pattern in Figure 9.2 with the electron beam aligned with the [011] zone axis. The atomic planes causing diffraction spots in Fig. 9.2**B** are indicated by colored arrows: yellow (100), red (110) and light blue (111). In this diffraction pattern, all Si and Ag atomic planes are parallel to each other. The spacings of Ag atomic planes measured in Fig. 9.2**B** are within 0.5% of bulk values, normalized to bulk Si atomic plane spacings, and angles between planes indicate face-centered cubic structure. The Si (002) reflections shown in the diffraction pattern, indicated by yellow arrows, are forbidden reflections, but appear because of double diffraction from multiple planes. The spacing of interference pattern caused by penetration of an electron beam through multiple crystals with different atomic plane spacings that are parallel

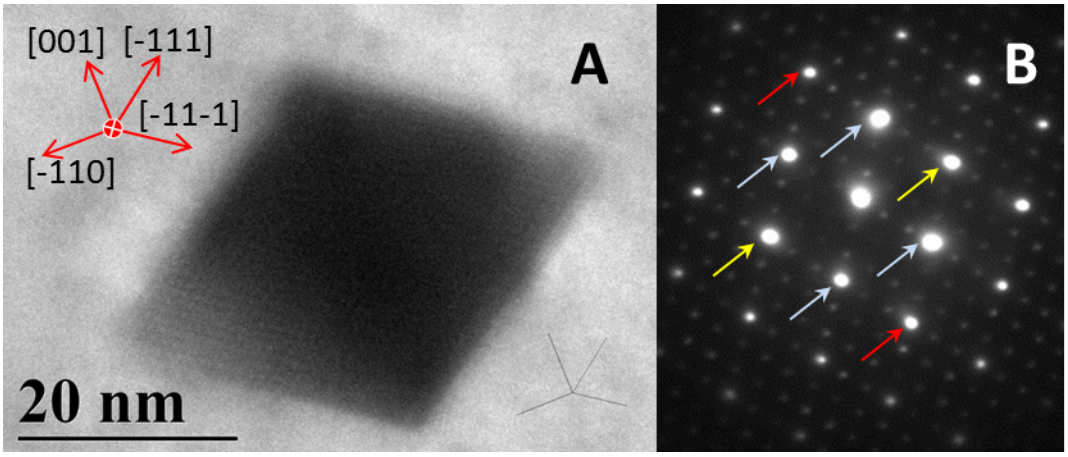

Figure 9.2: **A** Transmission electron micrograph and **B** electron diffraction pattern of same nanoparticle in sample Ag9 shown in Fig. 9.1. Zone axis of the electron beam is [011].

was described by Moire, for instance the Si (111) and Ag (111) planes, are determined by Equation 9.1

$$L_{111} = \frac{d_{Si(111)} \times d_{Ag(111)}}{d_{Si(111)} - d_{Ag(111)}} = \frac{3.135\mathring{A} \times 2.358\mathring{A}}{3.135\mathring{A} - 2.358\mathring{A}} = 9.51\mathring{A} \tag{9.1}$$

where $d_{A(xyz)}$ is the spacing of plane (xyz) of element A [30].

Close alignment of the Ag and Si atomic planes and the location inside the Si matrix renders the independent determination of planar spacing of Ag nanoparticles impossible without interference. This phenomenon also hinders exact observation of the size of nanoparticles using these micrographs. Moire interference pattern of Ag and Si (110) atomic planes contained in the portion of micrograph enclosed by white dashed lines in Fig. 9.1 is enhanced by Fourier filtering. The measured interference fringe spacing is 5.6 Å, and calculated value for interference fringe of Si (220) and Ag (220) planes with spacings 1.919 and 1.444 Å, respectively, using Eq. 1 is 5.8 Å.

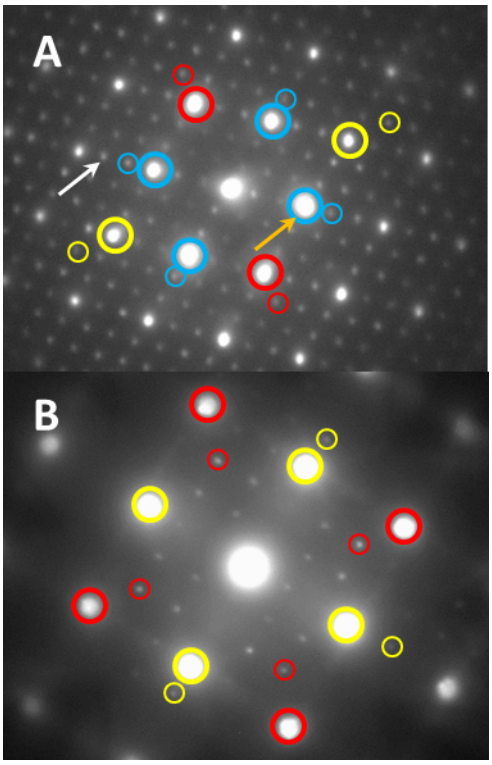

Figure 9.3: Electron diffraction patterns shown in Figures **A** 9.1 and **B** 9.2 modified to increase visibility of weak reflections from Ag atomic planes or caused by Moire interference. Reflections from atomic planes are outlined by Si (thick) and Ag (thin) circles. Zone axis of the electron beam is **A** [011] and **B** [100].

The difference between measured and calculated values for fringe spacing shown in Fig. 9.1**A** is 5%.

The diffraction patterns shown in Figs. 9.1**B** and 9.2**B** are presented in Figure 9.3 with values of brightness, contrast and gamma increased from 0.50 to 0.55. Low-intensity diffraction reflections caused by diffraction from Ag atomic planes or multiple diffractions due to Moire interference are more easily visible. The periodic nature of the high and low intensity diffraction reflections are a consequence of the relationship of crystal structures and lattice parameters of Si and Ag.

Silver fcc and Si diamondlike crystal structures are similar, with the diamond-

like crystal structure essentially being made up of two fcc sublattices offset in [111] direction fit into a larger unit cell. Diamondlike unit cell therefore contains twice as many atoms as fcc unit cell. Unit cells of Si and Ag have five (110) and (111) atomic planes, and [111] projections of each have atoms in same positions. The [110] projections of each crystal structure are different, shown in Fig. 6.5 on page 42. In the fcc unit cell, there are three (100) atomic planes, whereas in diamondlike unit cell there are five (100) atomic planes. The lattice parameters of Si and Ag are 5.431 and 4.087 Å, respectively, so Ag lattice parameter is 24.5% smaller than that of Si. In reciprocal space, such as in a diffraction pattern, diffraction from atomic planes with smaller spacing is larger and vice-versa. Therefore, diffractions from Ag (111) or (110) atomic planes are approximately 33% farther than from Si counterparts.

Electrons in the electron beam are undergoing multiple diffractions from atomic planes resulting in diffraction patterns shown in Fig. 9.3. In this case, the effective result is multiple points of origin of electrons before undergoing their final diffraction, which is then collected as data. Even though there is one electron beam incident on the specimen, and one true (000) transmitted beam, the effect of multiple diffractions results in multiple (000) transmitted beams. Therefore, there are multiple diffraction patterns overlaid on top of each other. The periodic, low-intensity spots are actually higher-order reflections of electrons that have been diffracted at least once previously. For example, the orange arrow in Fig. 9.3 is pointed at a (111) diffraction spot, assuming single diffraction from Si(111) planes of an electron initially directed toward the center spot, the (000) transmitted beam. An electron starting in the incident beam, diffracted by a (111) plane of Si, and then diffracted by a (311) Ag plane would be collected at the diffraction spot marked by the white arrow. The two additional low intensity diffraction spots between every high intensity diffraction spot in Fig. 9.3**A** are due to double (or higher) diffraction from Si and Ag atomic planes.

The contrast of different areas of the nanoparticle in Figs. 9.1**A** and 9.2**A** indicates the thickness of Ag in that area of the nanoparticle compared to others. Lighter contrast in square projection in Fig. 9.1 is near the edges, and darker contrast at center, indicating the edges are thinner than center. Lighter contrast in Fig. 9.2**A** is at two sharp corners, and darker contrast is in center and uniform along (001) direction. This indicates the two sharp, thin corners are apices, and the wide, thick part along (001) direction is the base of the octahedron.

The micrographs in Figures 9.1**A** and 9.2**A** show that the shape of the nanoparticle is octahedral and bound by (111) surfaces. The aspect ratio is near unity, calculated by comparing the length of nanoparticle measured along the (110) and (100) directions. The [110] projection, Fig. 9.2**A**, of the nanoparticle shows that the sides are (111) planes, the base is rotated 3° from (001) plane, and the apices are bisected by (110) plane. The nanoparticle's four sides in the [100] projection, Fig. 9.1**A**, are rotated 3° from (011) directions indicated on micrograph.

The size of the nanoparticle in Fig. 9.2**A** is 29.1 nm in the [111] direction and 27.7 nm in the [11-1] direction, and it is approximately square in Fig. 9.1**A** with side lengths 33 and 35 nm. It should be noted that filtering by Fourier transformation and masking, as in Fig. 9.1**A**, eliminates some noise associated with electron interference, so reported lengths should be considered upper bounds. The uncertainty caused by fuzzy boundaries could account for the apparent misalignment of the nanoparticle shape with atomic planes, or this could be a characteristic of an enclosed Ag nanoparticle grown heteroepitaxially in silicon with no free surfaces.

Additional Moire interference patterns are reported in Figures 9.4 and 9.5 observed in samples Ag9 and -3, respectively. A portion of the micrograph in Fig. 9.4 is Fourier filtered and shows Moire interference of Si and Ag (111) planes, with measured fringe spacing of 8.9 Å. A smaller nanoparticle created by different exper-

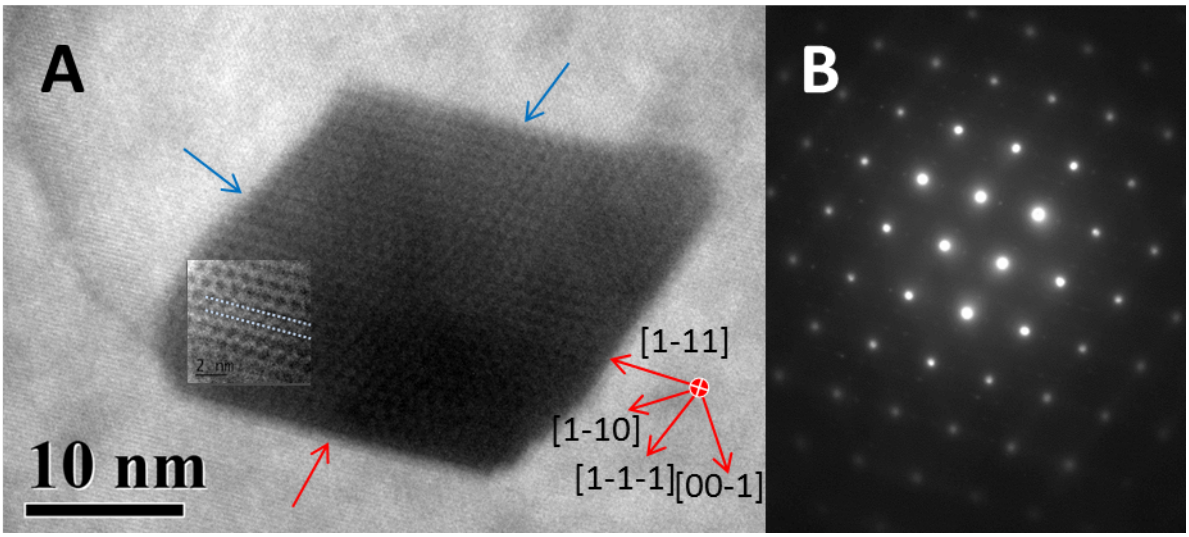

Figure 9.4: **A** Transmission electron micrograph and **B** electron diffraction pattern of partially-filled void nanoparticle in sample Ag9. The edge of the void is visible on the left. Portion of the micrograph is Fourier filtered to enhance interference fringe, and spacing of fringe is 8.9 $/AA$. Zone axis of the electron beam is [011].

imental conditions is shown in inset of Fig. 9.5, and the Moire interference of Si and Ag (111) planes with fringe spacing 9.9 Åis measured. The calculated fringe spacing using Eq. 9.1 with tabulated values for Si and Ag (111) planes is 9.51 Å.

Nanoparticles that occupy a portion of the total void volume are shown in Figs. 9.4 and 9.5. In Fig. 9.4**A**, the edge of the void can be seen on the left side of the micrograph, and diffraction pattern in **B** shows zone axis is [110]. Red arrows are pointing at Ag/Si interfaces, and blue arrows at Ag/vacuum interfaces, and all interfaces are predominantly bound by (111) planes. Two nanoparticles with free volume are shown in Fig. 9.5**A**, and **B** shows high resolution micrograph of left nanoparticle. The two nanoparticles in **A** are approximately the same size, though the free volume not filled by metal is different for each one. Figures 9.4 and 9.5 illustrate that free volume varies widely, but the amount of trapped Ag does not indicating that the Ag content of each nanoparticle is dependent on diffusion

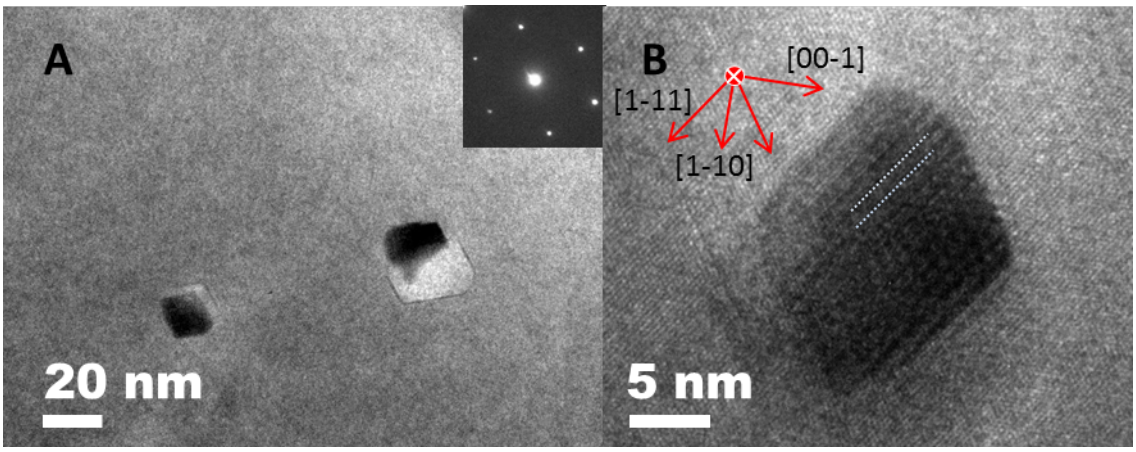

Figure 9.5: Transmission electron micrographs from sample Ag3 of **A** two nanoparticles with differing open volumes, and **B** high-resolution electron micrograph of left nanoparticle in **A**. Interference fringe is visible in **B** without Fourier filtering, and fringe spacing is 9.9 $/AA$. Zone axis of the electron beam is [011], and major crystallographic directions are indicated.

parameters and independent of void size. When voids are nucleated heterogeneously, following He ion fluence less than 1×10^{16} cm^{-2}, void sizes vary widely [68]. The nanoparticle in Fig. 9.4**A** is imaged along the same zone axis as that shown in Fig. 9.2**A**, and the size of the two compare favorably even though there is no free volume in the latter. Furthermore, the shapes of nanoparticles in Figs. 9.4 and 9.5, with free volume, are primarily bound with (111) planes and bisected by (110) and (100) planes, just as in the nanoparticle in Figs. 9.1 and 9.2. The shapes of fully-filled nanoparticles and partially filled void-nanoparticles differ by small area bounded by (100) planes, indicating that the surface energies are slightly different in their anisotropy. In the case of silicon, the lowest energy surface is (111) and $\gamma_{100} = 1.11\gamma_{111}$ is the next lowest surface energy [14]. This relationship is not observed for any Ag nanoparticles or Ag nanoparticle/void complexes in this study. The surface energy is weakly dependent on the nature of the interface, whether it is Ag-Si or

Ag-void.

9.3 Crystal imperfections and atomic plane alignment measured by channeling Rutherford backstattering spectra and angular scans

Rutherford backscattering energy spectra obtained when the ion beam is aligned with an atomic plane, such as [100] or [111], decreases the areal density of target atoms thus reducing the backscattering yield. If the ion beam is aligned with a major crystalline axis, where multiple atomic planes intersect, $\langle 100 \rangle$ or $\langle 111 \rangle$, the backscattering yield is further reduced. Using this method, the number of defects in a monocrystalline material can be measured in comparison to a control sample.

Figure 9.6 shows RBS channeling spectra from sample Ag1 and pure Si control sample. The ion beam is aligned with the surface normal crystalline axis, the $\langle 100 \rangle$ axis, and that is plotted with "random" energy spectra obtained when the ion beam is un-aligned and encounters areal density of material corresponding to bulk volumetric density. The raw data shown in this figure differ by a significant amount, but this is due to different fluences of analyzing ion beam used to collect the data (essentially, different data collection times). The random spectra are used to normalize the channeling spectra by obtaining the value for χ_d, from Equation 6.2, and these results are shown later.

Figure 9.7 shows random and channeling spectra from samples Ag3, -6, -7 and pure Si control obtained with ion beam aligned with $\langle 100 \rangle$ axis. Channeling spectra show that refining and optimizing the parameters for defect annealing and Ag diffusion has a measurable impact on the amount of defects measured in Si.

Every channeling spectrum has significant deviation from pure Si channeling spectrum between channels 50-200, so an additional step is taken in data analysis. A third-order polynomial is fitted to random spectrum in the channel interval 50-200,

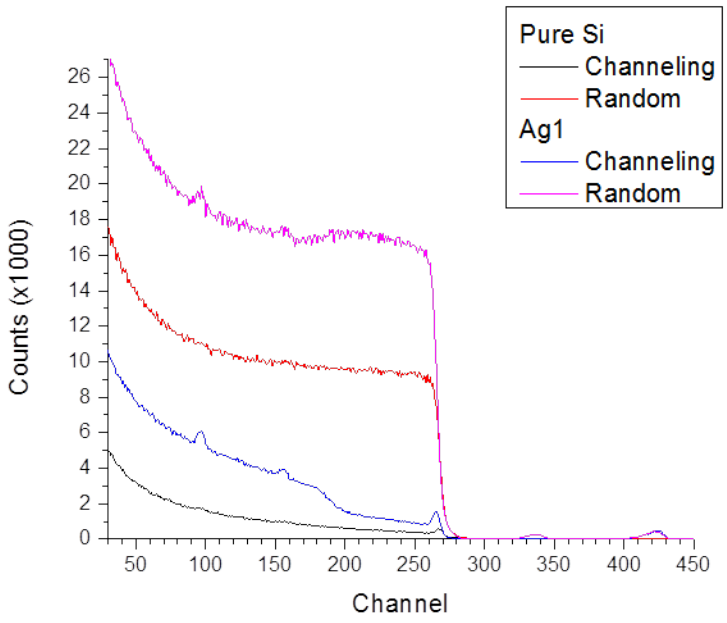

Figure 9.6: RBS channeling energy spectra from sample Ag1 and pure Si with ion beam aligned with ⟨100⟩ (surface-normal) channeling axis.

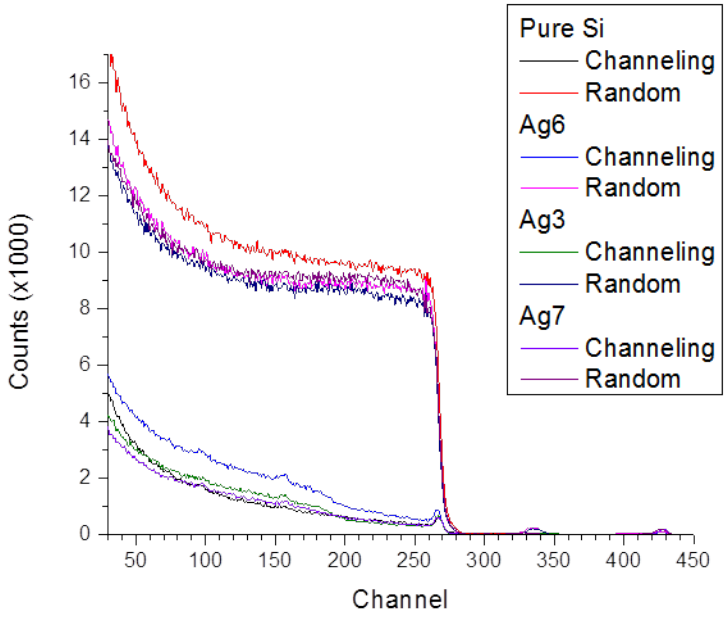

Figure 9.7: RBS channeling energy spectra from samples Ag3, -6, -7 and pure Si with ion beam aligned with ⟨100⟩ (surface-normal) channeling axis.

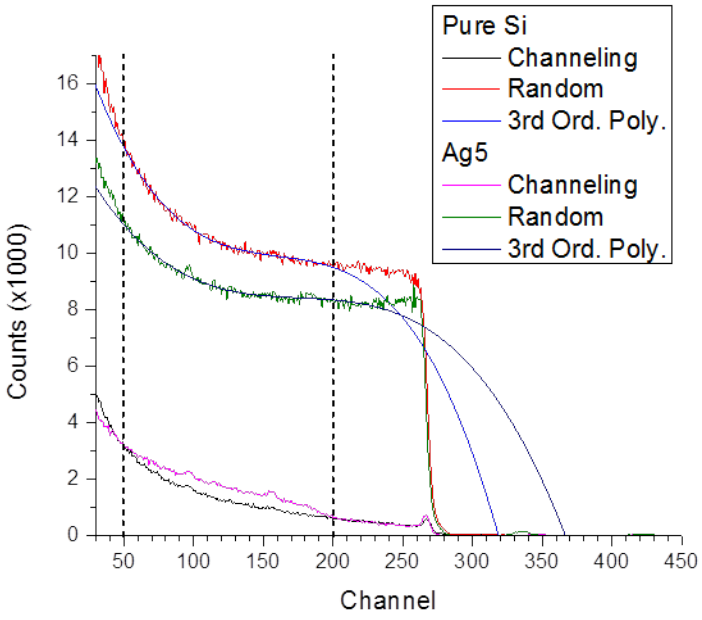

Figure 9.8: RBS channeling energy spectra from sample Ag5 and pure Si with ion beam aligned with ⟨100⟩ (surface-normal) channeling axis. The random spectra are fitted with third-order polynomials in the channel interval 50-200 to decrease noise in extracted disorder profiles.

and two of these fittings are shown in Figure 9.8 for sample Ag5 and pure Si control.

This effort is taken to decrease the effect of noise in the random spectra on the relative disorder profiles that are shown in Figure 9.9. The relative disorder is calculated by taking the ratio of the difference of sample and control channeling yields versus random and control channeling yields:

$$\frac{n_D}{n} = \frac{\chi_d - \chi_v}{1 - \chi_v} \tag{9.2}$$

where χ is calculated using Eq. 6.2 for d, samples that have crystalline damage, and for v, the control sample for each channel number. This calculation gives relative

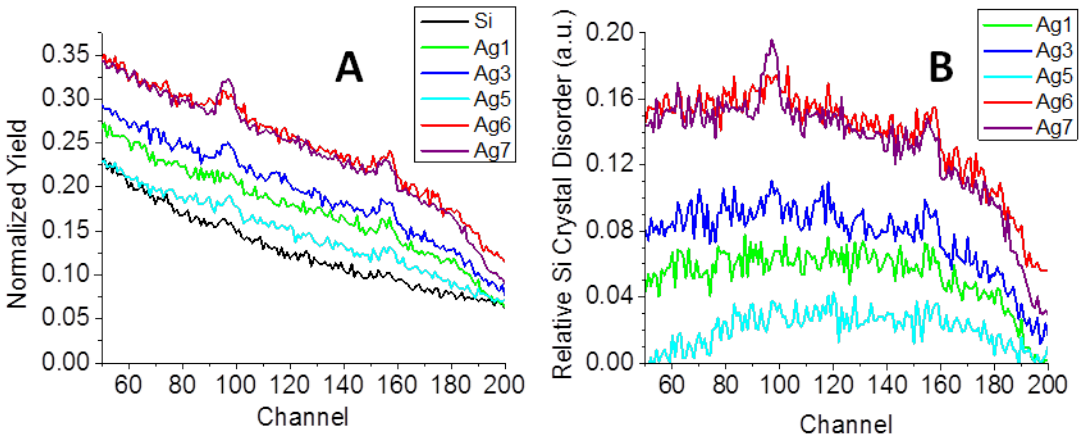

Figure 9.9: **A** Normalized channeling yields from samples Ag1, -3, -5, -6, -7 and pure Si calculated by ratio of channeling counts to random polynomial-fitted counts. **B** Relative Si disorder of samples Ag1, -3, -5, -6 and -7 calculated by equation

disorder in each sample compared to others, specifically the control sample. In the case where the sample does not contain a significant number of dislocations, which dechannel ions in a slightly different way than point defects, this value for relative disorder is the same as the defect concentration normalized by the atomic concentration of the sample. However, for samples Ag1, -3, -6, and -7, there are certainly a significant number of dislocations which accompany Si point defects. It is possible that sample Ag5 has sufficiently few dislocations that the relative disorder is the normalized defect concentration.

Sample Ag3 is analyzed more to understand the position of silver atomic planes in silver nanoparticles. RBS channeling spectra obtained with the beam aligned with **A** the surface-normal $\langle 100 \rangle$ axis and **B** the off-normal $\langle 110 \rangle$ axis are shown in Figure 9.10. The beam is aligned with the (100) plane channel as it is scanned across the $\langle 110 \rangle$ axis in **B**. Insets in Fig. 9.10 show backscattering counts from Ag atoms in sample Ag3. The backscattering yield from Ag atoms in the $\langle 110 \rangle$ axis channeling

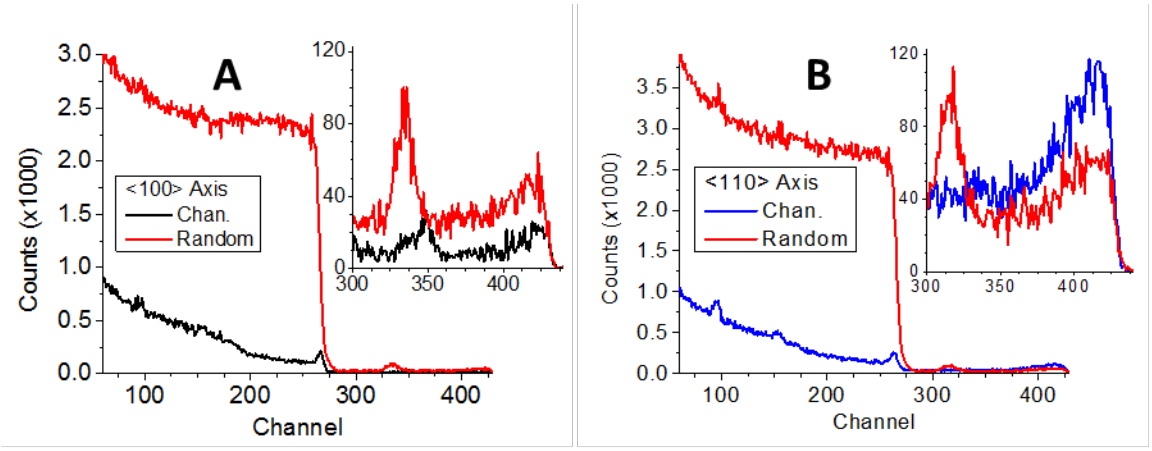

Figure 9.10: RBS channeling energy spectra from sample Ag3. Ion beam aligned with **A** ⟨100⟩ axis and **B** ⟨110⟩ axis and (100) plane. Insets show backscattering counts from Ag atoms in Si samples.

spectrum is greater than that of the random spectrum, indicating that some Ag atoms are in lattice positions that push into the ⟨110⟩ axis. This could mean that Ag atoms take tetrahedral interstitial positions, based on Fig. 6.5 on page 42.

Angular scans across the same channeling axes in Fig. 9.10 are obtained for the full energy spectrum and recorded. The scanning data shown in Figure 9.11 are from **A** ⟨100⟩ axis and **B** ⟨110⟩ axis with beam aligned with (100) plane channel, as before. Data are obtained for each channel at each scanning position, and then integrated over intervals twenty channels wide and plotted. The depth and depth interval that each angular scan represents increases as channel (backscattering energy) decreases. Near the surface, in channels 241-260 for both **A** and **B**, the minimum yields are 5.9% and 5.1%, respectively. Pure Si with no defects analyzed with same ion beam at same temperature would have minimum yields of 4-4.5%, so sample Ag3 is relatively free of significant crystallographic damage.

Figure 9.12 compares angular scans of Si near the surface and Ag in the nanoparticle region channeling **A** ⟨100⟩ axis and **B** ⟨110⟩ axis with beam aligned with (100)

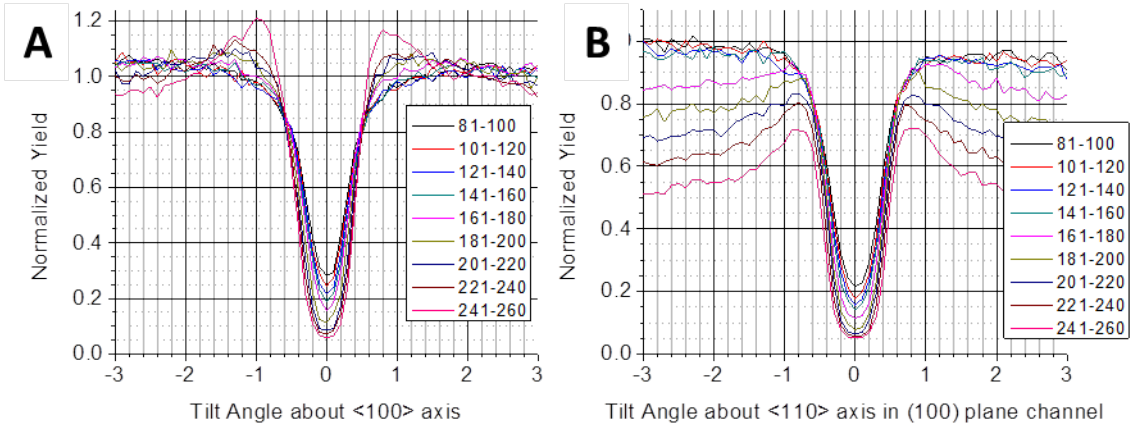

Figure 9.11: RBS angular scans from different depths of Si from sample Ag3. Sample is tilted across **A** ⟨100⟩ axis and **B** ⟨110⟩ axis in (100) plane.

plane channel. The minimum yields from Ag nanoparticles, 27% and 45%, respectively, are significantly higher, but the (100) and (110) atomic planes of Ag and Si are parallel. The minimum yields for Ag from both Fig. 9.12**A** and **B** are located 0.1° from center of Si axis, but this does not change the conclusion.

Angular scans data from Ag atoms in nanoparticles and interstitials closer to the surface are shown in Figure 9.13. The inset in Fig. 9.10**B** shows that backscattering yield from Ag atoms is higher when beam is channeled along ⟨110⟩ than when the beam is not aligned with a channeling axis or plane. The position of maximum yield in the ⟨110⟩ axis angular scan of interstitial Ag atoms in Fig. 9.13 is in the center of the channel, at tilt 0°, showing that the interstitials are in the center of the channel. The location of tetrahedral interstice is not the center of the ⟨110⟩ axial channel in the diamondlike unit cell of Si, according to Fig. 6.5 on page 42. However, literature has an example of angular scans of He interstitials with tetrahedral coordination occupying center of ⟨110⟩ axial channel [2]. It is possible that measurable portion of Ag atoms between surface and void layer occupy tetrahedral interstices in Si crystal.

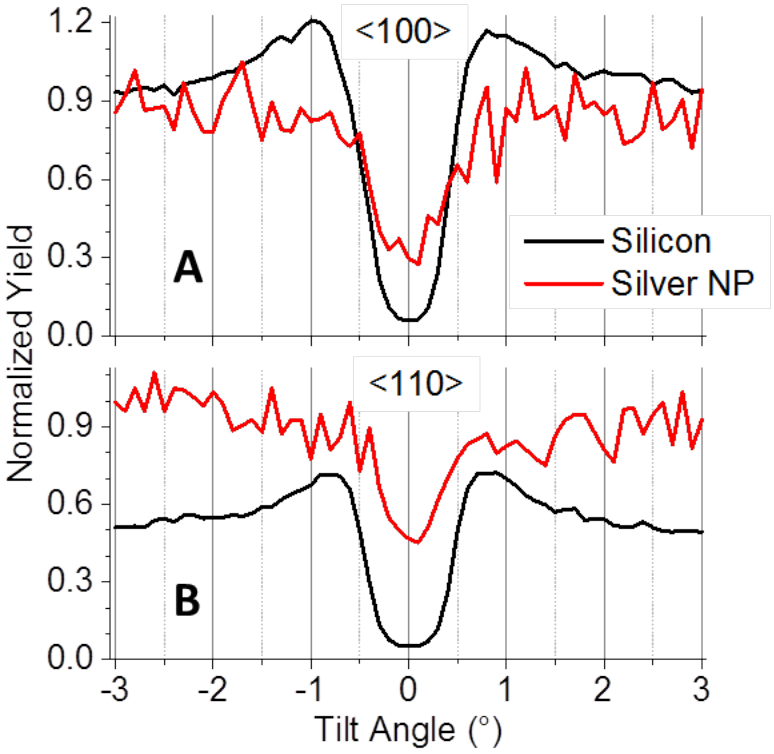

Figure 9.12: RBS angular scans of pure Si near the surface and from Ag nanoparticles in sample Ag3. Ion beam aligned with **A** ⟨100⟩ axis and **B** ⟨110⟩ axis and (100) plane.

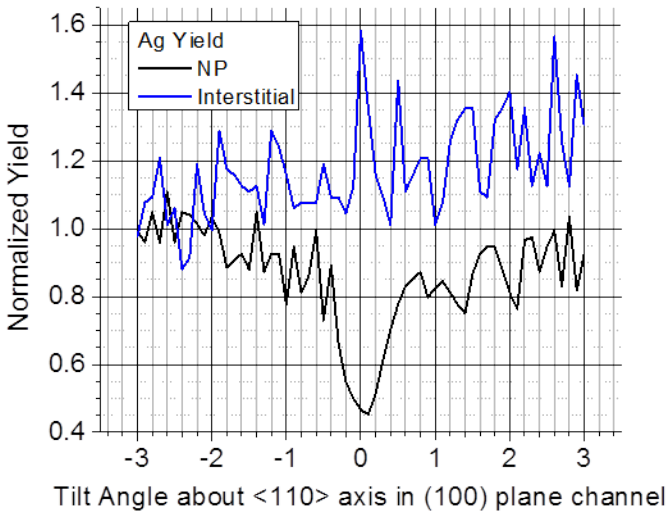

Figure 9.13: RBS angular scans of Ag backscattering signal from sample Ag3 scanned across ⟨110⟩ axis in (100) plane from two depth intervals. The interstitials are closer to the surface than nanoparticles.

9.4 Conclusions

The orientation of atomic planes in Ag nanoparticles grown on inner surfaces of voids in Si have been measured by high-resolution TEM, electron diffraction and RBS angular scanning, and have been shown to be parallel with their Si counterparts (e.g. Ag(111) is parallel to Si(111)) with small discrepancies. Electron diffraction shows that Ag(100) and Si(100) are mis-aligned by approximately 3°, and RBS angular scanning shows that tilt angle of minimum yield of Ag ⟨100⟩ and ⟨110⟩ axes are 0.1° from that of Si. However, these small discrepancies do not change the overall conclusion that Ag and Si atomic planes are parallel.

Silver nanoparticles grow on the inner surface of voids in Si heteroepitaxially, using 4:3 Ag:Si relationship on Si(111) surfaces or 2:3 Ag:Si relationship on Si(100) surfaces. Heteroepitaxial growth starts heterogeneously on inner corners of voids in Si,

and is maintained until the nanoparticle fully fills the void. Silver nanoparticles form (111) surfaces at the interfaces with vacuum in partially-filled void-nanoparticles. When the nanoparticle partially fills the void, the shape is primarily bound by (111) surfaces. Small areas bound by (100) Si surfaces have been observed, but whent the nanoparticle fully fills the void, the only boundaries are with Si(111) surfaces. The shape of a nanoparticle that fully fills a void is octahedral with aspect ratio near unity bound by (111) surfaces. The "base" of the octahedral nanoparticle is close to (100) plane, and apices are bisected by (110).

Silver atoms occupy tetrahedral interstices in Si unit cell between Si surface, where Ag is originally deposited, and Ag nanoparticles. It is assumed that silicon point defects facilitate Ag diffusion from the surface, but Ag atoms in tetrahedral interstitial positions do not require interaction with Si point defects. Analysis of the amount of relative disorder of Si atoms by RBS channeling shows that one condition, Ag5, has peak relative disorder around 3%. Comparison of the measured relative disorders with the amount of Ag trapped in nanoparticles, in Fig. 8.3 on page 85 in Chapter 8, reveals that relative disorder and amount of Ag trapped in nanoparticles are not related. Figure 9.9 shows that Ag5 and -1 have lowest relative disorder, around 3% and 6%, respectively, but Fig. 8.3 shows that Ag5 has almost 7 nm of equivalent thickness of bulk Ag film, the second highest, and Ag1 has one of the lowest amounts of Ag atoms trapped in nanoparticles, 2.5 nm. The two highest values of Si relative disorder in Fig. 9.9 are similarly separated in Fig. 8.3, where Ag6 and -7 have up to 17% relative Si disorder but Ag6 has almost 10 nm of equivalent thickness of bulk Ag film trapped in nanoparticles, the highest amount measured, to Ag7's 2.5 nm, one of the lowest measured. Clearly, Si interstitial point defects or dislocations are not solely responsible for mediating Ag diffusion. The Si point defect that cannot be measured by RBS channeling, the vacancy, could be the defect that mediates Ag

diffusion from surface to voids. Rollert et al suggested that Ag could diffuse by the dissociative mechanism, involving Ag interstitials occupying substitutional lattice sites [60]. The lack of a relationship between Si defects measured by RBS channeling and trapped Ag support diffusion of Ag mediated by the dissociative mechanism.

REFERENCES

[1] M Alatalo, MJ Puska, and RM Nieminen. First-principles study of He in Si. *Physical Review B*, 46:806–809, 1992.

[2] WR Allen. Lattice site of helium implanted in Si and diamond. *MRS Proceedings*, 279:433–438, 1992.

[3] Harry A Atwater and Albert Polman. Plasmonics for improved photovoltaic devices. *Nature Materials*, 9(3):205–213, March 2010.

[4] F. J. Beck, S. Mokkapati, and K. R. Catchpole. Plasmonic light-trapping for si solar cells using self-assembled, ag nanoparticles. *Progress in Photovoltaics: Research and Applications*, 18(7):500–504, 2010.

[5] Mark L. Brongersma and Vladimir M. Shalaev. The case for plasmonics. *Science*, 328(5977):440–441, 2010.

[6] E. Buehler. *50 Years Progress in Crystal Growth: A Reprint Collection*, chapter The first Czochralski silicon, pages 105–106. Elsevier, Amsterdam, The Netherlands, 2004.

[7] Quark Y. Chen and Clayton W. Bates. Geometrical factors in enhanced photoyield from small metal particles. *Phys. Rev. Lett.*, 57:2737–2740, Nov 1986.

[8] W K Chu, J W Mayer, and M.-A. Nicolet. *Backscattering Spectrometry*. Academic Press, New York, 1978.

[9] F. Corni, G. Calzolari, S. Frabboni, C. Nobili, G. Ottaviani, R. Tonini, G. F. Cerofolini, D. Leone, M. Servidori, R. S. Brusa, G. P. Karwasz, N. Tiengo, and a. Zecca. Helium-implanted silicon: A study of bubble precursors. *Journal of Applied Physics*, 85(3):1401, 1999.

[10] W Deweerd, T Barancira, S Bukshpan, S Demuynck, G Langouche, K Milants, R Moons, J Verheyden, and H Pattyn. Mössbauer study of the proximity gettering of cobalt atoms to He-induced nanosized voids in c-Si. *Physical review. B, Condensed matter*, 53(24):16637–16643, June 1996.

[11] W Deweerd, R Moons, K Milants, J Verheyden, G Langouche, and H Pattyn. Trapping of ion-implanted 57Co to cavities in c-Si : a qualitative study. *Nuclear Instruments and Methods in Physics Research Section B: Beam Interactions with Materials and Atoms*, 127/128:307–310, 1997.

[12] S E Donnelly, V M Vishnyakov, R C Birchter, and G Carter. The effects of radiation damage and impurities on void dynamics in silicon. *Nuclear Instruments and Methods in Physics Research Section B: Beam Interactions with Materials and Atoms*, 177:132–139, 2001.

[13] D J Eaglesham, V C Venezia, H-J Gossmann, and A Agarwal. Quantitative TEM of point defects in Si. *Journal of Electron Microscopy*, 49(2):293–8, January 2000.

[14] D J Eaglesham, A E White, L C Feldman, N Moriya, and D C Jacobson. Equilibrium shape of Si. *Phys. Rev. Lett.*, 70(11):1643–1647, 1993.

[15] S. K. Estreicher, J. Weber, A. Derecskei-Kovacs, and D. S. Marynick. Noble-gas-related defects in Si and the origin of the 1018 meV photoluminescence line. *Physical Review B*, 55(8):5037–5044, February 1997.

[16] J H Evans, I A V A N Veen, and C C Griffioen. The annealing of helium-induced cavities in silicon and the inhibiting role of oxygen. *Nuclear Instruments and Methods in Physics Research Section B: Beam Interactions with Materials and Atoms*, 28:360–363, 1987.

[17] ASTM Standard F-723. Standard practice for conversion between resistivity and dopant density for boron-doped, phosphorus-doped, and arsenic-doped silicon, ASTM International, West Conshohocken, PA, 1999.

[18] G. Faraci, A. R. Pennisi, and G. Margaritondo. Mechanism of photoelectron yield enhancement from ag clusters. *Phys. Rev. B*, 40:4209–4211, Aug 1989.

[19] G. Faraci, A. R. Pennisi, V. Privitera, H. Burtscher, and A. Schmidt-Ott. Photoemission from small particles of ag and au. *Phys. Rev. B*, 37:10542–10546, Jun 1988.

[20] L Fedina, O I Lebedev, G Van Tendeloo, J Van Landuyt, O A Mironov, and E H C Parker. In situ {HREM} irradiation study of point-defect clustering in {MBE-grown} strained {$Si1-xGex/(001)Si$} structures. *Phys. Rev. B*, 61(15):10336–10345, April 2000.

[21] L.C. Feldman, J.W. Mayer, and S.T. Picraux. *Materials Analysis by Ion Channeling*. Academic Press, New York, 1982.

[22] P F P Fichtner, J R Kaschny, R A Yankov, A Muecklich, U Kreissig, and W Skorupa. Overpressurized bubbles versus voids formed in helium implanted and annealed silicon. *Applied Physics Letters*, 70:732–734, 1997.

[23] D. M. Follstaedt. Relative free energies of si surfaces. *Applied Physics Letters*, 62(10):1116–1118, 1993.

[24] R. H. Fowler. The analysis of photoelectric sensitivity curves for clean metals at various temperatures. *Phys. Rev.*, 38:45–56, Jul 1931.

[25] B Fultz and J Howe. *Transmission electron microscopy and diffractometry of materials*. Springer, Heidelberg, 3rd edition, 2009.

[26] P I Gaiduk, J Lundsgaard Hansen, A Nylandsted Larsen, and E A Steinman. Nanovoids in {MBE-grown} {SiGe} alloys implanted in situ with {$Ge+$} ions. *Phys. Rev. B*, 67(23):235310, June 2003.

[27] J F Gibbons. Ion implantation in semiconductors part II: Damage production and annealing. *Proceedings of the IEEE*, 60(9):1062–1096, September 1972.

[28] C C Griffioen, J H Evans, P C de Jong, and A van Veen. Helium desorption/permeation from bubbles in silicon: a novel method for void production. *Nuclear Instruments and Methods in Physics Research Section B: Beam Interactions with Materials and Atoms*, 27:417–420, 1987.

[29] A. Haarahiltunen, H. Vainola, O. Anttila, M. Yli-Koski, and J. Sinkkonen. Experimental and theoretical study of heterogeneous iron precipitation in silicon. *Journal of Applied Physics*, 101(4):043507, 2007.

[30] P.B. Hirsch, A. Howie, R.B. Nickolson, D.W. Pashley, and M.J. Phelan. *Electron Microscopy of Thin Crystals*. Plenum Press, New York, NY, 1965.

[31] E. Holmström, A. Kuronen, and K. Nordlund. Threshold defect production in silicon determined by density functional theory molecular dynamics simulations. *Phys. Rev. B*, 78:045202, Jul 2008.

[32] S.M. Hu. Nonequilibrium point defects and diffusion in silicon. *Mat. Sci. Engr. Reports*, 13:105–192, 1994.

[33] J.H. Hubbell and S.M. Seltzer. Tables of x-ray mass attenuation coefficients and mass energy-absorption coefficients from 1 kev to 20 mev for elements z = 1 to 92 and 48 additional substances of dosimetric interest. Technical report, 100 Bureau Dr., M/S 8460 Gaithersburg, MD 20899, May 2004.

[34] Alexander V. Kildishev, Alexandra Boltasseva, and Vladimir M. Shalaev. Planar photonics with metasurfaces. *Science*, 339(6125), 2013.

[35] A Kinomura, J S Williams, N Tsubouchi, and Y Horino. Platinum atom location on the internal walls of nanocavities investigated by ion channeling analysis. *Nuclear Instruments and Methods in Physics Research Section B: Beam Interactions with Materials and Atoms*, 190(1-4):606–610, May 2002.

[36] A. Kinomura, J. S. Williams, J. Wong-Leung, and M. Petravic. Microstructural difference between platinum and silver trapped in hydrogen induced cavities in silicon. *Applied Physics Letters*, 72(21):2713, 1998.

[37] G F Knoll. *Radiation Detection and Measurement*. New York: John Wiley and Sons, Inc., 2000.

[38] R. Kogler, a. Peeva, a. Lebedev, M. Posselt, W. Skorupa, G. Ozelt, H. Hutter, and M. Behar. Cu gettering in ion implanted and annealed silicon in regions before and beyond the mean projected ion range. *Journal of Applied Physics*, 94(6):3834, 2003.

[39] E. Kotai. Computer methods for analysis and simulation of RBS and ERDA spectra. *Nuclear Instruments and Methods in Physics Research Section B: Beam Interactions with Materials and Atoms*, 85(1-4):588–596, 1994.

[40] O. Kurnosikov, H. J. M. Swagten, and B. Koopmans. Internal electron diffraction from atomically ordered subsurface nanostructures in metals. *Phys. Rev. Lett.*, 106:196803, May 2011.

[41] F K LeGoues, M Liehr, M Renier, and W Krakow. Microstructure of epitaxial Ag/Si(111) and Ag/Si(100) interfaces. *Philosophical Magazine B*, 57(2):179, 1988.

[42] B Q Li and J M Zuo. The development of epitaxy of nanoclusters on lattice-mismatched substrates: Ag on H-Si(111) surfaces. *Surface Science*, 520:7, 2002.

[43] Jens Lindhard, M. Scharff, and H. E. Schiott. Range concepts and heavy ion ranges (notes on atomic collisions, ii). *Mat. Fys. Medd. Dan. Vid. Selsk.*, 33(14), 1963.

[44] N.C. Lindquist, P. Nagpal, K.M. McPeak, D.J. Norris, and S.-H. Oh. Engineering metallic nanostructures for plasmonics and photonics. *Rep. Prog. Phys.*, 75:036501, 2012.

[45] J. P. McCaffrey and J. Hulse. Transmitted color and interference fringes for tem sample preparation of silicon. *Micron*, 29:139–144, 1998.

[46] S M Myers and D M Follstaedt. Forces between cavities and dislocations and their influence on semiconductor microstructures. *Journal of Applied Physics*, 86(6):3048–3063, 1999.

[47] S M Myers, Seibt M, and Schroeter W. Mechanisms of transition-metal gettering in silicon. *Journal of Applied Physics*, 88(7):3795, 2000.

[48] S M Myers and G A Petersen. Transport and reactions of gold in silicon containing cavities. *Phys. Rev. B*, 57(12):7015, 1998.

[49] Michael Nastasi, Tobias Höchbauer, Jung-Kun Lee, Amit Misra, John P. Hirth, Mark Ridgway, and Tamzin Lafford. Nucleation and growth of platelets in hydrogen-ion-implanted silicon. *Applied Physics Letters*, 86(15):154102, 2005.

[50] H. Okamoto and T.B. Massalski. Au-si (gold-silicon). In P. Villars, H. Okamoto, and K. Cenzual, editors, *ASM Alloy Phase Diagrams Center*. ASM International, Materials Park, OH, USA, 1990.

[51] R.W. Olesinski and G.J Abbaschian. Ag-si (silver-silicon). In P. Villars, H. Okamoto, and K. Cenzual, editors, *ASM Alloy Phase Diagrams Center*. ASM International, Materials Park, OH, USA, 2006-2012, 1990.

[52] M.H.F. Overwijk, J. Politiek, R.C.M. de Kruiff, and P.C. Zalm. Proximity gettering of transition metals in silicon by ion implantation. *Nuclear Instruments and Methods in Physics Research Section B: Beam Interactions with Materials and Atoms*, 96:257–260, 1995.

[53] K.-H. Park, G.A. Smith, K. Rajan, and G.-C. Wang. Interface characterization of epitaxial ag films on si(100) and si(111) grown by molecular beam epitaxy. *Metallurgical Transactions A*, 21:2323–2332, 1990.

[54] G A Petersen, S M Myers, and D M Follstaedt. Gettering of transition metals by cavities in silicon formed by helium ion implantation. *Nuclear Instruments and Methods in Physics Research Section B: Beam Interactions with Materials and Atoms*, 127-128:301–306, May 1997.

[55] W. G. Pfann. *50 Years Progress in Crystal Growth: A Reprint Collection*, chapter How zone melting was invented, pages 107–108. Elsevier, Amsterdam, The Netherlands, 2004.

[56] S. Pillai and M.A. Green. Plasmonics for photovoltaic applications. *Solar Energy Materials and Solar Cells*, 94(9):1481 – 1486, 2010.

[57] V Raineri, A Battaglia, and E Rimini. Gettering of metals by He induced voids in silicon. *Nuclear Instruments and Methods in Physics Research Section B: Beam Interactions with Materials and Atoms*, 96:249–252, 1995.

[58] V Raineri, S Coffa, E Szilágyi, J Gyulai, and E Rimini. He-vacancy interactions in Si and their influence on bubble formation and evolution. *Phys. Rev. B*,

61(2):937–945, January 2000.

[59] Vito Raineri. Gettering by voids in silicon: A comparison with other techniques. *Solid State Phenomena*, 57-58:43–52, 1997.

[60] F. Rollert, N.A. Stolwijk, and H. Mehrer. Solubility , diffusion and thermodynamic properties of silver in silicon. *J. Phys. D: Appl. Phys.*, 20:1148–1155, 1987.

[61] S Y Sayed, F Wang, M Malac, A Meldrum, R F Egerton, and J M Buriak. Heteroepitaxial growth of gold nanostructures on silicon by galvanic displacement. *ACS Nano*, 3(9):2809, 2009.

[62] Francois Schiettekatte, Carl Wintgens, and Sjoerd Roorda. Influence of curvature on impurity gettering by nanocavities in Si. *Applied Physics Letters*, 74(13):1857, 1999.

[63] A. Schmidt-Ott, P. Schurtenberger, and H. C. Siegmann. Enormous yield of photoelectrons from small particles. *Phys. Rev. Lett.*, 45:1284–1287, Oct 1980.

[64] Stephen M. Seltzer. Calculation of photon mass energy-transfer and mass energy-absorption coefficients. *Radiation Research*, 136(2):147–170, 1993.

[65] Lin Shao and Michael Martin. *Boron: Compound, Production and Application*, chapter Boron Doping in Semiconductor Device Fabrication, pages 473–492. Nova Science Publisher, Inc., Hauppauge, NY, 2010.

[66] Yugang Sun, Yang Ren, Yuzi Liu, Jianguo Wen, John S Okasinski, and Dean J Miller. Ambient-stable tetragonal phase in silver nanostructures. *Nat Commun*, 3:971, 2012.

[67] J R Tesmer and M Nastasi, editors. *Handbook of Modern Ion Beam Materials Analysis*. Materials Research Society, Pittsburgh, PA, 1995.

[68] R. Tonini, F. Corni, S. Frabboni, G. Ottaviani, and G. F. Cerofolini. High-dose helium-implanted single-crystal silicon: Annealing behavior. *Journal of Applied Physics*, 84(9):4802, 1998.

[69] V C Venezia, D J Eaglesham, T E Haynes, Aditya Agarwal, D C Jacobson, H-J Gossmann, and F H Baumann. Depth profiling of vacancy clusters in {MeV-implanted} Si using Au labeling. *Applied Physics Letters*, 73(20):2980–2982, 1998.

[70] J S Williams, M J Conway, J Wong-Leung, P N K Deenapanray, M Petravic, R A Brown, D J Eaglesham, and D C Jacobson. The role of oxygen on the stability of gettering of metals to cavities in silicon. *Applied Physics Letters*, 75(16):2424, 1999.

[71] J Wong-Leung, C E Ascheron, M Petravic, R G Elliman, and J S Williams. Gettering of copper to hydrogen-induced cavities in silicon. *Applied Physics Letters*, 66:1231–1233, 1995.

[72] J. Wong-Leung, J. S. Williams, A. Kinomura, Y. Nakano, Y. Hayashi, and D. J. Eaglesham. Diffusion and transient trapping of metals in silicon. *Phys. Rev. B*, 59:7990–7998, 1999.

[73] J Wong-Leung and JS Williams. Rutherford backscattering and channeling study of Au trapped at cavities in silicon. *Nuclear Instruments and Methods in Physics Research Section B: Beam Interactions with Materials and Atoms*, 118(95):34–38, 1996.

[74] J. Wong-Leung, J.S. Williams, and E. Nygren. Diffusion and trapping of Au to cavities induced by H-implantation in Si. *Nuclear Instruments and Methods in Physics Research Section B: Beam Interactions with Materials and Atoms*, 106(1-4):424–428, December 1995.

[75] L Zhu, J Chan, S Mccoy, J Gelpey, B Guo, K Shim, N Davidtheodore, M Martin, J Carter, and M Hollander. Defect characterization in boron implanted silicon after flash annealing. *Nuclear Instruments and Methods in Physics Research Section B: Beam Interactions with Materials and Atoms*, 266(10):2479–2482, May 2008.

[76] J F Ziegler. SRIM-2003. *Nuclear Instruments and Methods in Physics Research Section B: Beam Interactions with Materials and Atoms*, 219-220:1027–1036, 2004.

[77] A Zur and T C McGill. Lattice match: An application to heteroepitaxy. *Journal of Applied Physics*, 55:378, 1984.